SHIAVE, ALI IMRAN, Ph.D. Processing and Characterization of Cobalt Nanowires-Growth Characteristics and Thermal Characterization of Cobalt Nanowire Modified Nanofluid (2020)
Directed by Dennis R. LaJeunesse and Ram V. Mohan. 174 pp.

Cobalt (Co) 1-D nanostructures commonly known as nanowires, based on one of five ferromagnetic materials have attracted interest from researchers because of their potential applications in various fields. In particular, novel and suitable methods to grow nanowires that are simple, scalable, cheap and environmentally benign are also of great interest. Various approaches have been employed to grow metal nanowires; however, each process has their own set of advantages and disadvantages. Template Assisted electrodeposition (TAE) of nanowire growth in which solid templates act as a scaffold for the growth of the nanowire, is recognized as the best approach to grow pure metal nanowires for several reasons. The TAE process is simple to adopt, scalable, and cheap. TAE allows for the generation of a broad range of nanowire morphologies and sizes as the templates control the nanowire dimensions during synthesis; the growth of nanowires is governed by the dimensions of the template's nano-channels. However, there are many challenges in this process as even a minor change in any processing conditions i.e. bath temperature, solution pH, mechanical conditions/agitation, current density, etc. can and will change the properties of formed nanowires. This high sensitivity of the nanowire synthesis process is why it is necessary to determine and define the relationship between various processing conditions and their effect on nanowire properties and characteristics. Another major problem with TAE nanowire fabrication is the polycrystalline natures of yielded nanowires. Although some research groups have shown that it is possible to grow

single-crystalline nanowires using this approach, the conditions and factors that control crystallinity still remain unclear.

1-D nanostructures (that are composed of a metal, a metal oxide, or a non-metal) possess completely different properties compared to the same bulk materials and are useful in different applications. Metallic nanowires offer superior properties e.g. thermal, electrical, and mechanical when compared to nanowires composed of metal oxides or non-metals. Metallic materials have higher thermal conductivities than most materials (apart from some exceptions such as diamond) and have been used for decades for efficient thermal transport; metal nanowires are no different and have a similar set of properties that provide enormous potential in electronic and sensor applications which require thermal transport and management. This is especially true in our current world of miniaturization, where effective and efficient heat transport and transfer mechanisms are critical. From small electronic devices to giant industrial machinery, improved capacity for the dissipation of thermal energy results in better performance. Conventional coolants i.e. water, ethylene glycol, and oil are currently being used in heat transfer and temperature management applications although thermal conductivity of these fluids is poor. If incorporated successfully, metal nanowires can offer a potential solution to this problem. Metal based nanofluids will play an important role in efficient heat transfer. However, current work with nanofluids (both metal and non-metal), have only involved the use of 0-D nanostructures and there has been little work done with 1-D nanowire based fluid materials. The major challenge in using 1-D nanostructure based nanofluids has been the difficulty of stabilizing 1-D nanofluids. Heat transfer nanofluids that are not

well stabilized will lead to settlement of added nano level constitutes thus clogging the heat transfer channels. Metallic nanofluid, composed of ferromagnetic metals such as iron, cobalt, and nickel offers several advantages beyond a more efficient heat transfer media. Further, due to the ferromagnetic nature of cobalt, a cobalt nanofluid has several advantages including a more efficient cleaning process for the clogged channels which could overcome the problems posed by sedimentation easily.

My dissertation focuses on several areas critical to synthesis, characterization of cobalt nanowires, and application of metallic nanofluids, specifically cobalt nanowire based nanofluid. In my research (1) I have developed a protocol for the synthesis of cobalt nanowire and successfully synthesized Co nanowire using template-assisted electrodeposition technique; (2) I have defined and understood morphological and structural effects of various deposition parameters i.e. bath temperature, current density; (3) I have proposed and established growth models for these nanowires and the associated mechanisms of growth; (4) I have prepared stabilized Cobalt nanowire based nanofluids in an aqueous medium; (5) I have determined effective thermal conductivity of a cobalt-nanowire nanofluid that are composed of different levels of nanowire concentration and (6) I have demonstrated the application and showed the efficacy of a cobalt-nanowire nanofluid in simple heat exchanger set up.

PROCESSING AND CHARACTERIZATION OF COBALT NANOWIRES-GROWTH CHARACTERISTICS AND THERMAL CHARACTERIZATION OF COBALT NANOWIRE MODIFIED NANOFLUID

by

Ali Imran Shiave

A Dissertation Submitted to
the Faculty of The Graduate School at
The University of North Carolina at Greensboro
in Partial Fulfillment
of the Requirements for the Degree
Doctor of Philosophy

Greensboro
2020

Approved by

_____
Committee Chair

DEDICATION

To my family

APPROVAL PAGE

This dissertation written by Ali Imran Shiave has been approved by the following committee of the Faculty of The Graduate School at the University of North Carolina at Greensboro.

Committee Chair

Dennis R. LaJeunesse

Committee Members

Ram V. Mohan

Hemali P. Rathnayake

Eric A. Josephs

Jeffery R. Alston

03-13-2020

Date of Acceptance by Committee

03-13-2020

Date of Final Oral Examination

TABLE OF CONTENTS

Page

LIST OF TABLES

Page

LIST OF FIGURES

Page

CHAPTER I

INTRODUCTION

1D nanostructures, which include nanowires have attracted great interest from the scientific and engineering community for the past two decades due to their unique electrical, magnetic, thermal, and mechanical properties. They can be an influential agent for future optical, electronics, drug delivery, sensors, large scale data storage devices. Lots of experimental and simulation studies have been done on metal nanowires to exploit their potential and scope for further applications. Due to the tremendous potential, various synthesizing methods i.e. vapor phase synthesis, vapor-liquid-solid(VLS), template-assisted method, solution liquid-solid(SLS), self-assembled nanowire have been employed to grow nanorods and nanowires with better morphology, higher aspect ratio and more defined and controllable dimensions. Among various methods, template-assisted electrodeposition (TAE) of nanowire is the most popular method because of its simplicity, cost-effectiveness, high yield, controlled growth parameters, reduced contamination, and its ease of scalability to mass production. Various metals, non-metals, and hybrid nanowires can be synthesized efficiently using this technique. Since the development of template-assisted electrodeposition technique in 1996 by Martin et al.[1], different research groups have explored various aspects of this process and have grown nanowires of different materials including magnetic nanowires which are promising for

many different applications. The goal of much of these works is to develop materials with a high magnetic coercivity which is often a requirement for high energy products, and a figure of merit of a permanent magnet. Currently, rare-earth compounds are used as permanent magnets because of their extremely high magneto-crystalline anisotropy; however, when compared to 3d transition ferromagnetic metals like Fe, Ni, Co, and their alloys, rare earth magnets have some disadvantages including low magnetization level, limited thermal stability, and a limited and often politically restricted supply of rare earth ores. Although 3d transition metals are abundant, these elements are known as soft magnetic materials as they have high saturation magnetization, low coercivity, and high Curie temperature[2].

Being one of five ferromagnetic materials, Co nanowires provide an excellent solution for applications in data storage, biosensors, MEMs devices, catalyst for electro-oxidation of urea peroxide, etc. To date, extensive research has been done on pure metallic nanowires and most of these works focused primarily on processing parameters. It is important to have a better understanding of the behavior, structure of Co nanowires, and the influence of synthesis parameters on the final Co nanowire. By using well-defined characterization techniques, we will be able to determine how specific parameters impact the properties of the Co nanowires generated by this method. There have been some reports stating the effect of processing parameters on Cobalt nanowires yet a clear relationship among these processing conditions, structure, and properties are still to be well understood. In this dissertation, I specifically examined the effects of

electrodeposition process parameters bath temperature and current density to understand the associated process-property relationship.

Most TAE synthesized nanowires exhibit mainly polycrystalline structure, although some studies have shown that with precise control of process parameters it is possible to grow single-crystalline nanowires [3]. Reports have shown that highly crystalline nanowires can only be produced at very high temperatures (800-1200 ^{0}C)[4], or low deposition potential[5]. Despite these findings, there are no clear or precise conditions for the synthesis of single-crystalline magnetic nanowires until now. In this dissertation, I have shown that it is possible to get single crystal magnetic nanowire regions even when processing at a low temperature, which may impact applications such as hybrid solar cells, super capacitors, and fuel cells.

My research focuses on defining the conditions in TAE growth process of cobalt nanowire by determining the effect of temperature, current density on the morphology, and structure of grown nanowires. I have confirmed the crystallinity by X-ray Diffraction (XRD) and Selected Area Electron Diffraction (SAED). I have shown that altering the TAE conditions for the formation of Co nanowires affects the morphology of nanowires, though the structural properties of these nanowires do not change significantly. In addition to this, I have clearly defined the growth mechanism that can lead to the formation of single-crystalline regions in these nanowires.

The high thermal conductivity of metals is one of the most important features for cooling and heat exchanger applications. At present, industrial coolants are used in those places where heat dissipation is needed although their thermal properties are not good.

However, for the last few decades, with the development of nanoparticles, metal nanofluid (NF) has attracted interest as an efficient heat transfer medium because of its greater theoretical capacity for thermal conductivity. There is a great need for such new modified materials, especially with the rapid improvement of electronics technology from microchip to supercomputer, for which efficient heat dissipation is one of the main concerns. Industries spend billions of dollars to keep the instruments and machinery cool for higher performance and longevity[6]. Coolants like water, ethylene glycol (EG), and oil have been used for a long time. However, the thermal conductivity of these coolants is poor. For example, at room temperature, the thermal conductivity of water is 0.613 kW/mK and for EG it is less, at only 0.25 kW/mK. These numbers are several orders of magnitude lower when compared to the high thermal conductivity of metals. For instance, the highly conductive metal, Silver (Ag) has a thermal conductivity of 429 W/m.K. However, liquid coolants are convenient for several reasons including versatility and simplicity of application. One solution to the lower thermal conductivity of liquid coolant involves increasing the size of cooling channels thus increasing the size of the apparatus to improve thermal efficiency. However, this possibility is not feasible in all the cases, when most of the devices and instruments are getting smaller every day. Furthermore, these conventional liquid coolants cannot match the demand, and a new type of liquid coolant system with higher thermal conductivity is required to meet the current and increasing future demands. Nanofluid coolants can offer a solution to these problems because of their unique and improved thermal properties, namely, conductivity, diffusivity, and heat transfer coefficient compared to the base fluids, thus combining the

best qualities of both novel metals (i.e. high thermal conductivity) and current liquid coolants(i.e. high specific heat capacity).

Nanolfuids are stable dispersion of nanoparticles in base fluid i.e. water, EG, or oil, and a stable dispersion is required in order to improve their properties. NF offers many advantages over conventional solid-liquid suspensions including

- High surface area that can lead to more heat transfer surface between base fluids and added nanoparticles.
- Better dispersion stability because of particle Brownian motion
- Less pumping power, flow velocity, and driving force compared to pure coolants to attain same heat transfer performance
- Less possibility of clogging the heat transfer channels compared to traditional slurries
- Offers the possibility of system miniaturization
- Modifiable properties including surface wettability, thermal conductivity, etc. by adjusting the particle concentration.

Despite these promising characteristics, development in NF research is widely hindered by inadequate characterization techniques of NFs, lack of agreeable results from different researchers, lack of proper theoretical understanding of thermal conductivity improvement mechanisms, etc. The main challenge posed by the NF is the sedimentation of added nanoparticles over time. As nanoparticles have high surface energy, they tend to aggregate after some time and as a result settlement of nanoparticles occurs. An unstabilized nanofluid will have detrimental effects on the cooling system, especially in

small cooling channels. Sedimentation will lead to not only clogging of the channels but also a decrease in thermal efficiency. Apart from that, the stability of NFs is related to the improvement of thermal conductivity as better dispersion leads to higher thermal conductivity. This problem has been overcome in many ways including the addition of surfactants to prevent aggregation[7], dispersion of the nanoparticles in the solution via sonication[8], surface modification of nanoparticles for better stability[9], etc. Most of the work to date deals with 0-D nanoparticles because of their smaller size and ease of dispersion. The application of 1-D nanomaterials, i.e. nanowire, in nanofluids for increasing the effective thermal conductivity is new and little work has been done in this area. Metallic nanowire nanofluid, especially magnetic nanowires provide many additional advantages to cooling systems and other applications.

The present research after addressing the issues from the synthesis of Cobalt nanowires via template-assisted approach to the successful integration of them into water towards preparing an efficient heat transfer fluid and understanding its efficacy.

In summary, this research involved and focused on the following:

1) Synthesis of 1-D Cobalt nanowire using Template-assisted Electrodeposition technique which yields highly pure nanowires
2) Physical characterization of the yielded nanowire to understand the effect of processing parameters on nanowire morphology, structure, crystal size, and orientation
3) Determination of growth model for Co nanowire

4) Finding an effective method for making stabilized metal nanofluid using synthesized Co nanowires
5) Investigation of the effective thermal conductivity of modified nanofluid and reasons for the change in thermal conductivity
6) Demonstration of the prepared nanofluid and its effectiveness in heat transfer through a simple microfluidic heat exchanger setup.

1.1 Motivation

Since the discovery of remarkable properties of materials at lower length scales, different techniques have been explored and demonstrated for the successful synthesis of nanowires with fascinating behavior and enhanced properties. Freestanding, purity, ease of method adaptation, etc. have been the key drivers for developing suitable synthesis methods. Among various synthesizing methods, template-assisted electrodeposition (TAE) is one of the most suitable and effective methods for the growth of metal nanowires. In this approach, it is possible to synthesize nanowires with close control of dimensions, properties, and purity. Various processing parameters i.e. pH of electrolyte bath, template material, temperature, current density, and additive are found to influence the nanowire properties. Not only processing conditions but also nanowire diameter, length, crystal structure, orientation, surface condition, etc. affect their properties. However, the polycrystalline nature of nanowires is one of the main problems of the TAE process. Few reports have shown that it is possible to synthesize single-crystalline nanowires through precise control over processing conditions i.e. high temperature or

deposition voltage. However, reports on a suitable process for single-crystalline nanowires via TAE at room temperature is still scarce. Both experimental and simulation works have been done on characterization of nanowires to understand their electrical[10], physical[11], optical[12], magnetic[13], and mechanical properties[14]. The present research focuses on the effect of various processing conditions on nanowire morphology and structure as the change in these conditions can influence the nanowire properties by a great deal.

Among many potential applications of metal nanoparticles, highly efficient heat transfer nanofluid is one of the most promising ones. For more than a century, scientists and engineers have made great efforts to enhance the poor thermal conductivity of conventional fluids. Maxwell, in 1873 first proposed that effective thermal conductivity of slurries can be improved by dispersing millimeter or micrometer-sized particles (size from 0.1 to 100 micron). However, the proposition could not be successful because of some major problems such as erosion, sedimentation, and high-pressure drop though it is considered to be the first milestone in this field. Nanofluid, on the other hand, is a diluted suspension of nanoparticles dispersed in conventional fluids i.e. water, ethylene glycol, and oil. Nanoparticles stay in suspension much longer than microparticles under static conditions. However, due to strong Van Der Waals attractions, nanoparticles tend to aggregate and various techniques are needed to overcome this issue. Different additives to control pH, surface modification, and ultra-sonication, etc. can be used to maintain a stable dispersion. Well dispersed nanoparticles show great improvement of thermal conductivity compared to the base fluid. For example, Moldoneanu et al.[15] have

reported recently that the thermal conductivity of water-based alumina nanofluid increases by 21% at room temperature. Metal nanoparticle-based nanofluid has also shown promise[16][17]. Most of the work till today focuses on 0-D nanoparticle-based nanofluid while nanowire-based nanofluid research is still not explored especially because of their bigger sizes. Finding a well-established route for stabilized metal nanowire-based nanofluid can be a great contribution to the scientific society and can solve the age-long problem of efficient heat transfer.

1.2 Research Objectives

Specific research objectives, experimental goals and analysis studies for current work are presented here

i. Synthesis of Co nanowires.

- Develop and employ a template-assisted electrodeposition method for Co nanowire synthesis
- Design, develop and modify the processing condition to study the physical properties of nanowires at three electrical current densities and bath temperatures

ii. Physical property characterization nanowires

- Morphology, structural and crystallographic characterization of Co nanowires using
  - Scanning electron microscope (SEM)
  - Energy dispersive spectroscopy (EDS)

- X-ray diffraction (XRD)
- Transmission electron microscopy (TEM)/High-Resolution Transmission electron microscopy (HRTEM)

- Study and analyze the data obtained to understand the influence of current density and temperature on the physical properties of synthesized nanowires.

iii. Nanowire growth model

- Formulate a suitable growth model for Cobalt nanowires in nanoporous membrane

iv. Study of effective thermal conductivity of nanofluid

- Establish a suitable route to prepare stabilized Co nanowire-based nanofluid
- Study the effective thermal conductivity of nanofluid and the possible reasons for the improvement of thermal conductivity
- Establish an experimental set up to demonstrate the effectiveness of nano-modified fluid in a heat exchanger

1.3 Organization of Dissertation

The dissertation is planned and presented in six chapters to provide the flow of current research and key findings. Chapter 1 (Present chapter) involves the introduction of the dissertation to provide an overview of the research, the potential application of the outcome and objectives.

Chapter 2 presents various aspects of nanowire processing. In this chapter, theory of electrodeposition, various templates used to synthesize free-standing, impurity-free nanowires, and cited works on template-assisted metal nanowires are discussed briefly. The detailed synthesis process of cobalt nanowire is presented in the methodology section. Results and discussions on the effect of current density and temperature on nanowire morphology, length, and amount of nanowire produced are presented.

Chapter 3 focuses on the effect of processing conditions on the structural properties of nanowires. In this chapter, different physical characterization techniques are discussed in brief including XRD, EDS, and TEM/HRTEM. A unique process of nanowire sample preparation for TEM/HRTEM is discussed in the methodology section. Detailed results and relevant discussions are presented to study the effect of different operating conditions on cobalt nanowire structural properties. An appropriate growth model is also established from the acquired data.

In Chapter 4, a novel application for the synthesized cobalt nanowires in the form of metal based nanofluid is presented. In this chapter, various aspects of nanofluid preparation, different mechanisms for thermal conductivity improvement and adopted models, stability and characterization techniques, and different thermal conductivity measurement techniques are discussed. The process of successful preparation of a stable nanowire-based nanofluid using DI water as base fluid is shown. The stability of prepared nanofluid, the effect of nanowire inclusion and pH on thermal conductivity, and possible reasons for the change in effective thermal conductivity are discussed in the results and discussions section.

Chapter 5 demonstrates the application of nano modified heat transfer fluid in a simple microfluidic heat exchanger system.

In chapter 6, the overall conclusion of the current research and future scope is presented.

CHAPTER II
NANOWIRE PROCESSING

2.1 Introduction

1-D nanostructures commonly known as nanowires or nanorods have gained tremendous attention because of their versatile applications in numerous fields. The definition of nanorods varies from nanowires; the aspect ratio (ratio of length to diameter) of less than 10 is considered as nanorods whereas aspect ratio more than 10 defines nanowires. Nanotube, on the other hand, is a 1-D structure with a hollow interior. Different synthesis methods have been developed to synthesize 1-D nanomaterials of varying shape, size, and properties. All of these methods have their own advantages and disadvantages. It is important to adopt a synthesis method that is simple, easy to apply, cost-effective, and environmentally benign. Among these processes, template-assisted electrodeposition (TAE) is one of the most popular. In this chapter, we will discuss TAE and effect of various processing conditions on synthesized nanowires using this approach.

2.2 Synthesis of Metal Nanowires

The formation of nanowires is mainly governed by crystallization where nucleation can start from a liquid, vapor, or solid phase. Growth is controlled to get the desired dimensions in both axial and radial directions by the process itself or by external

methods. Researchers have developed different strategies to synthesize free-standing nanowires which include:

i. Nanowire growth can be aided by using anisotropic solid structures
ii. Introduction of the solid-liquid interface which can reduce the seed symmetry
iii. Dimension control using preformed templates
iv. Controlling the level of supersaturation by modifying the growth of the seed
v. Addition of capping agent can control the kinetics of seed facets
vi. Self-assembly of 0-D nanostructures

Various synthesis methods based on these strategies have been developed to grow nanowires as shown in figure 2.1.

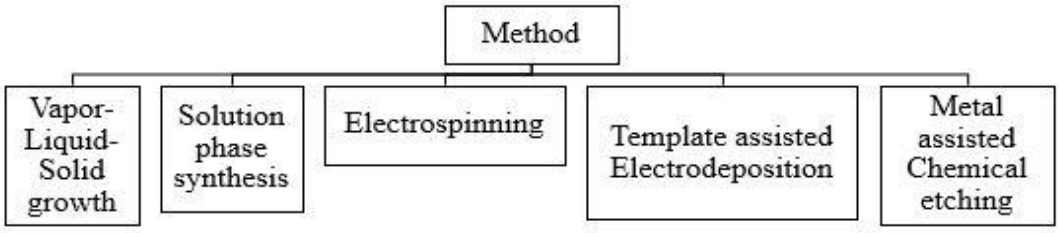

Figure 2.1. Various Synthesis Methods for Nanowire Growth

These synthesis methods are briefly discussed here.

2.2.1 Vapor-Liquid-Solid (VLS) Growth

VLS method is a well-established and popular method to grow semiconductor nanowires where metal nanoclusters are used as catalysts. In the presence of a semiconductor vapor phase source, the metal catalyst is heated just above the eutectic

point of the semiconductor metal system resulting in liquid droplet which consists of source alloy. As the reactants are fed continuously through the process, liquid droplets get supersaturated, and nucleation of solid nanowire starts. This growth is governed by the liquid-solid growth interface acting as a sink which leads to the continuous addition of desired material (a semiconductor in this case) into the growing lattice. Chemical vapor deposition[18], pulsed laser ablation[19] or molecular beam epitaxy[20] techniques are applied to get semiconductor reactants in the gaseous phase. Apart from VLS method, researchers have successfully grown different semiconductor nanowires using solid-liquid-solid[21], solution-liquid-solid[22], vapor-solid-solid[23] methods also.

2.2.2 Solution Phase Synthesis

In this process, nanowires are formed from a liquid precursor in the presence of a catalyst. After heating the solution to the desired temperature, a solid crystalline seed is injected which leads to the nucleation of the nanowires. Qian et al.[24] demonstrated the successful synthesis of iron phosphide nanowire using this process. They used a mixture of trioctylphosphine oxide (TOPO) and trioctylphosphine (TOP) as solvents. The mixture is heated to the desired temperature ($>300^0$C) and then metal precursor is injected to start the nucleation process to get high quality, uniform iron phosphide nanowires. The nanowires had a diameter of 5 nm while the lengths were 1 micrometer. Because of the less length and low aspect ratio these nanowires can be labeled as nanorods also. Gates and co-workers[25] synthesized single crystal Selenium nanowires with diameter of 10-30 nm while they got higher aspect ratios as the length of the nanowires were several

hundred microns. Gold nanowire[26], Cesium lead halide perovskite nanowires[27], etc. have also been synthesized using this technique.

2.2.3 Electrodeposition of Nanowires in Nanoporous Templates

Templates with nanoporous arrays are used to guide the growth of nanowires using electrodeposition techniques. This versatile method is one of the most popular methods for synthesis of 1-D nanostructures and was first introduced by martin[1] has been used since in conjunction with other techniques such as sol-gel, chemical vapor deposition, electrochemical deposition, and pressure injection. One side of the template is coated first with a conductive material mostly by thermal or sputter evaporation technique to make it an active electrode. The electrodeposition process is done using a suitable electrolyte containing the desired material to be deposited. Nanoporous templates are used as a cathode where the reduction of metal occurs while the anode is made with the same material which is to be deposited. Finally, after deposition, the templates are dissolved in a suitable solution (mostly NaOH and KOH) to get free-standing nanowires. Different templates have been used to synthesize various nanowires. Detailed discussions on templates and electrodeposition are discussed later. Au[28], Ni[2], Co[29], Cu[30], CdSe and CdTe[31] etc. have been synthesized using this technique.

2.2.4 Electrospinning

Electrospinning is a simple and the most efficient way to synthesize polymeric nanowires. In this process, a polymer solution is sprayed through a syringe. The surface

tension of the syringe tip can be overcome by applied high electric field yielding in the ejection of charged jet. Application of electric field helps to elongate the jet thousands or million times as the jet gets thinner to reach nanoscale level. Long nanofibers are then collected on a metal sheet that is electrically grounded followed by the solidification of the collected nanofiber. Electrospinning is a cheap, cost-effective, high-efficiency process that can produce long nanowire with well-controlled curvature. TiO_2 nanofibers[32], chitosan nanofibers[33], polymer/clay composite nanofiber[34], etc. have been synthesized using the electrospinning technique.

2.2.5 Metal Assisted Chemical Etching (MaCE)

MaCE is a wet etching technique that was first introduced as an electroless etching to make an unpatterned discontinuous metal layer of porous Si and III-V semiconductor in hydrofluoric acid (HF) and hydrogen peroxide (H_2O_2)solution[35]. In this process, noble metals i.e. Au, Pt, Ag are deposited on a semiconductor surface (i.e. Si) under open circuit inducing local oxidation-reduction reaction. Deposited metals act as local cathode where H_2O_2 is reduced releasing H^+ holes which are then injected into semiconductor valance band to be oxidized forming ionic solution. Thus the semiconductor material is removed without any consumption of metal. The overall reaction can be shown as equation (2.1)

$$Si + H_2O_2 + 6\,HF \xrightarrow{Au} 2\,H_2O + H_2SiF_6 + H_2 \uparrow \qquad (2.1)$$

With the help of a suitable catalyst and pattern, both porous and solid nanostructures can be synthesized using this process. The etching reaction occurs at the metal-semiconductor interface resulting in the etching of semiconductor which is right under the descending metal. The morphology of the final nanostructure can be controlled by etching temperature, immersion time, and solution concentration[36].

The schematics of these synthesis processes are illustrated in figure 2.2.

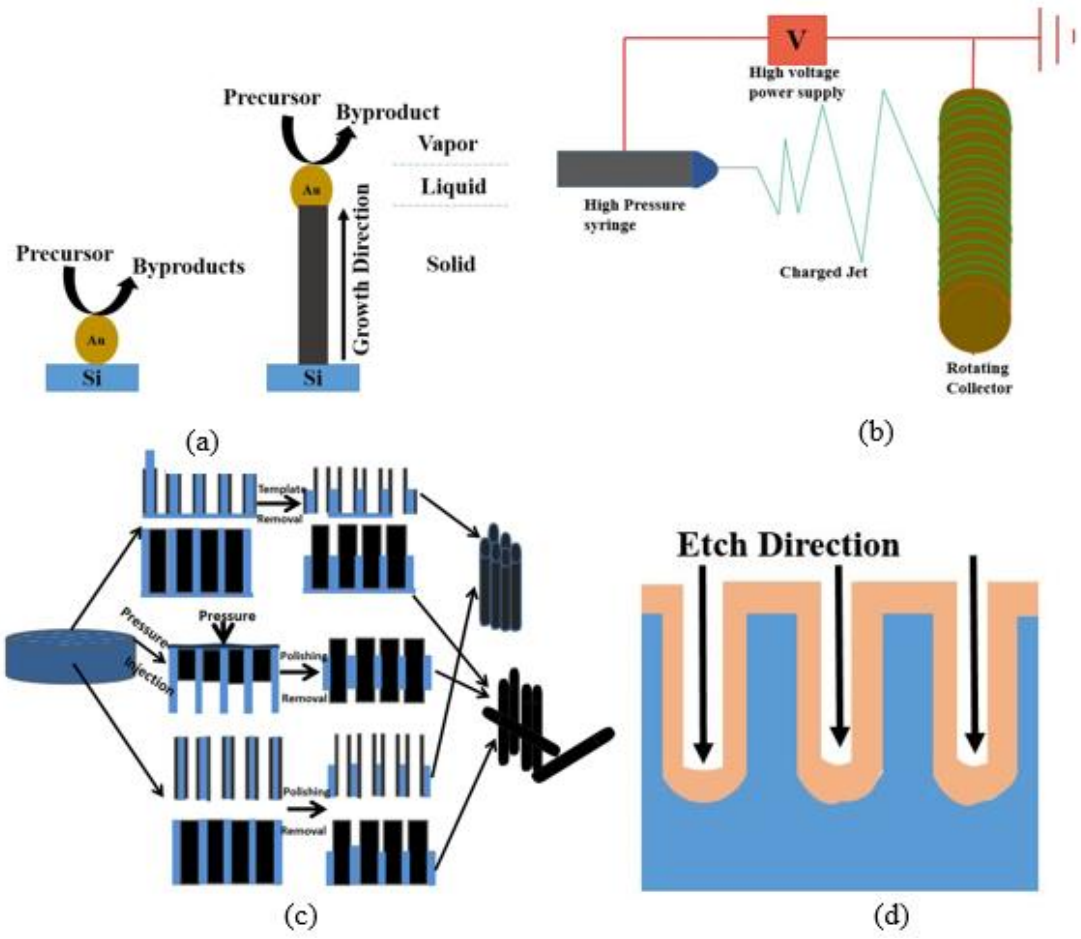

Figure 2.2. Nanowire Synthesis Methods; (a) VLS Method, (b) Electrospinning, (c) Template-assisted Electrodeposition and (d) MaCE

Among all these processes mentioned above, only VLS and template-based approach give orderly oriented, uniform diameter nanowires. Other processes result in randomly oriented nanowires and nanorods mostly in the form of powder[37]. VLS methods are advantageous as the nanowires are directly attached to the substrate making the characterization and application of yielded nanowire more suitable. However, at elevated temperature during the growth process, special catalysts are needed for forming a liquid capsule at the advancing surface. Besides, there is a possibility that these catalysts are incorporated also in the yielded nanowire and it is sometimes difficult to remove the capsules from nanowire tips.

On the other hand, advantages of TAE growths are often undermined by the polycrystallinity of the nanowire, difficulty to find appropriate template with desired pore diameter, and complete removal of the template after synthesis without sacrificing nanowire integrity.

2.3 Template-assisted Electrodeposition Process

Electrodeposition technique is advantageous because of high productivity and low cost, compared to conventional sputtering or molecular beam epitaxy techniques[38]. It involves diffusion of charged species with the help of an external electric field through a polar solution. Growth of desired material is occurred by the reduction of the charged species. The electrodes must be conductive for this process otherwise there will be no electron flow and apparently no electrodeposition will take place. As an external electric field is applied, nanowires start to grow immediately inside the nanopore of the template.

After complete growth, the template membrane is dissolved chemically to get free nanowires.

Generally, electrodeposition can be classified in 3 broad categories i.e. potentiostatic, galvanostatic, and electroless deposition. Potentiostatic electrodeposition is a 3-electrode deposition process (anode, cathode, and a reference electrode) in which deposition is carried out at a constant potential of the working electrode with respect to the reference electrode. Galvanostatic electrodeposition is a two-electrode deposition technique, where the deposition is carried out by passing a constant current between the working and counter electrodes. The electrode potential is not given much attention as the deposition is performed at standard, optimal current conditions. Electroless deposition, on the other hand, is a chemical deposition process that involves chemical agents to coat material on the template. The main difference between electroless and other two is that the deposited material should not be necessarily conductive for the former case while for both potentiostatic and galvanostatic processes the deposited material must be conductive.

Electrode potential E can be represented by the Nernst equation (2.2) when a solid material is immersed in a polar solvent or electrolyte.

$$E = E_0 + \frac{RT}{n_i F} \ln (a_i) \qquad (2.2)$$

Here E_0 is standard electrode potential or potential difference between electrode and solution, a_i is the reactivity, T is denoted as temperature, R is the universal gas constant, and F is Faraday's constant.

Figure 2.3 shows the representation of typical oxidation and reduction processes. If the electrode potential is more negative (higher) than the energy level of vacant molecular orbital of electrolyte, electron transfer will occur from electrode to solution and the electrolyte is reduced as shown in Figure 2.3(a). On the other hand, if the electrode potential is more positive (lower) than the energy level of the occupied MO, electrons will transfer from electrolyte to the electrode resulting in the oxidation of electrolyte as described in figure 2.3(b).

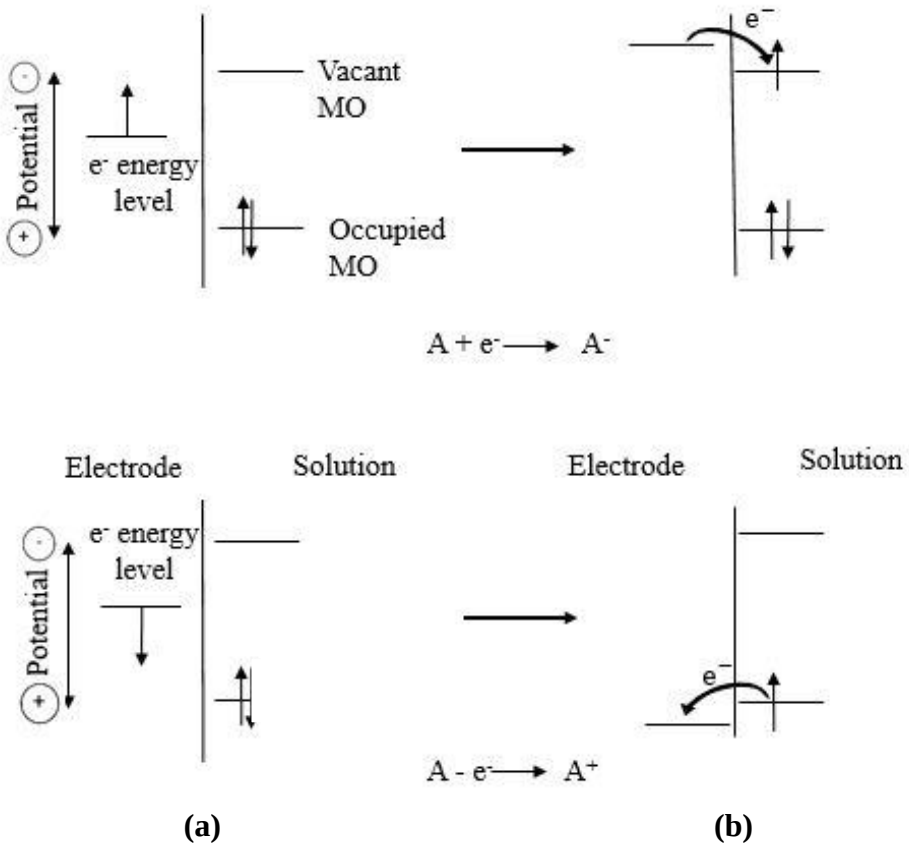

Figure 2.3. Process of (a) Reduction and (b) Oxidation of Material A in a Solution. Lowest Vacant and Highest Occupied Molecular Orbitals (MO) are shown[39]

When an external electric field is applied between two electrodes, charged species flow from one electrode to another resulting in electrochemical reactions at both electrodes. Nanowire growth with the presence of an electric field is a self-propagating process. Once a small rod is formed, current density lines and the electric field between nanowire tips and opposite electrode becomes greater than that of two electrodes as the distance is shorter now, resulting in continuous deposition of material on the tip of the rods and hence longer nanowires are formed.

Figure 2.4(a) represents a typical setup for the template-assisted nanowire electrodeposition process. A porous template is used as a cathode (negative terminal) while a metal sheet is used as anode (positive terminal). It must be made sure that anode and cathode stay parallel to each other. In the presence of a suitable electrolyte (usually consists of desired metal salts) and external electric field, cations diffuse through template channels and deposit on the cathode (in the available pore channels of template).

Figure 2.4(b) shows the current at different nanowire growth stages[40]. There is no significant change of current until the pores are filled (indicated as point (a) in the figure. Once the pores are filled, a sharp increase in current is seen because of improved contact with electrolytes (point (b) in figure). The current becomes saturated when the nanopores are completely filled thus in turn no or minimum change over time is found (point (c) in the figure) and template surface is covered with deposited metal.

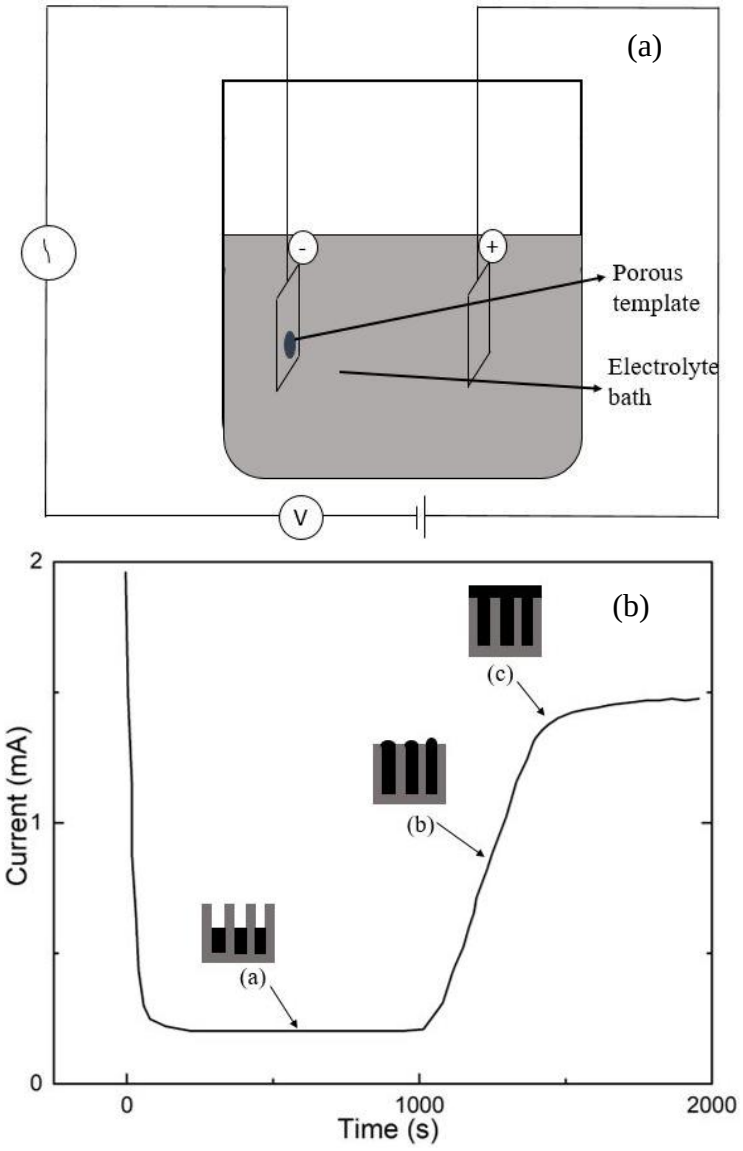

Figure 2.4. Typical Illustration of (a) Template-assisted Nanowire Growth Setup, (b) Current-time Curve during the Growth Process[37]

One of the main challenges in the TAE process is to find the most appropriate templates as they control the growth process. Templates with nanopores act as a scaffold for nanowire growth. Different types of templates have been used so far to synthesize

metal nanowires. Here, we will discuss a few of them which are commonly used by researchers.

2.4 Commonly Used Templates

Template growth can be classified into two main categories i.e. (i) endotemplating and (ii) exotemplating. In endotemplating process, an exoskeletal frame is created around nanoscale objects filling out the void left by them yielding in the exact negative replica of the template. Exotemplating on the other hand, the desired shape is formed inside the template holes. Template materials should meet certain criteria to be used for nanowire synthesis i.e. compatibility with processing conditions, thermal and chemical stability during synthesis and post-synthesis processes, the ability of desired materials to wet pore channels, and easiness of nanowire release after synthesis. The most commonly used templates are anodic alumina oxide (AAO) and radiation track-etched polycarbonate (PC) membranes.

2.4.1 Radiation Track-etched Polycarbonate

Polycarbonate membranes are synthesized by bombarding nano carbonate sheets with nanopores. Fission fragments create damage tracks which then are etched chemically to make them into pores. The pores with a diameter as small as 10 nm can be synthesized. PC membranes have some advantages as they are easy to handle during synthesis and post-synthesis steps, easy to remove after nanowire growth, even at high temperatures. However, the templates are susceptible to distortion during the heating

process and template removal might occur before complete densification of nanowires thus resulting in deformed particles. Ni, Co, Cu, and Au nanowires have been synthesized using this kind of membrane[41]. However, Schönenberger et al. showed that the channels do not have uniform diameter always[30].

2.4.2 Anodic Alumina Oxide (AAO) Membrane

AAO is the most used template as they are highly rigid and resistant to high temperature, nanowires of large surface area can be produced, freestanding and unidirectional nanowires can be synthesized, and have regular hexagonal nanoporous arrays. The pores densities can be up to 10^{11} pores/cm^2 and pore diameter can vary from 10 nm to 100 μm [42]. AAO templates are made by a two-step anodization process starting with an ultra-pure Al sheet. However, the removal of the template after nanowire growth is challenging. Ni[2], Au[43], Si[44], TiO_2[45], CdSe[46], Fe[38] nanowires were synthesized using AAO membrane. Recently, hard anodic alumina oxide (H-AAO) has been studied also because of its low processing time and large interpore distance[47]. Several other metals apart from aluminum such as Hf, Zr, Ta, Nb, and Ti can also form self-organized nanoporous film. Anodic titanium oxide (ATO) is particularly interesting because of its high potential to be used as self-cleaning, gas sensing, and dye-sensitized solar cells[48]. However, the main difference between ATO and AAO is that ATO nanoporous films contain separate nanotubes rather than a continuous porous film as shown in figure 2.5. The main advantage of AAO templates over radiation track- etched

templates are that the former one contains more densely packed nanopores. However, the removal of AAO templates after NWs synthesis requires harsh conditions.

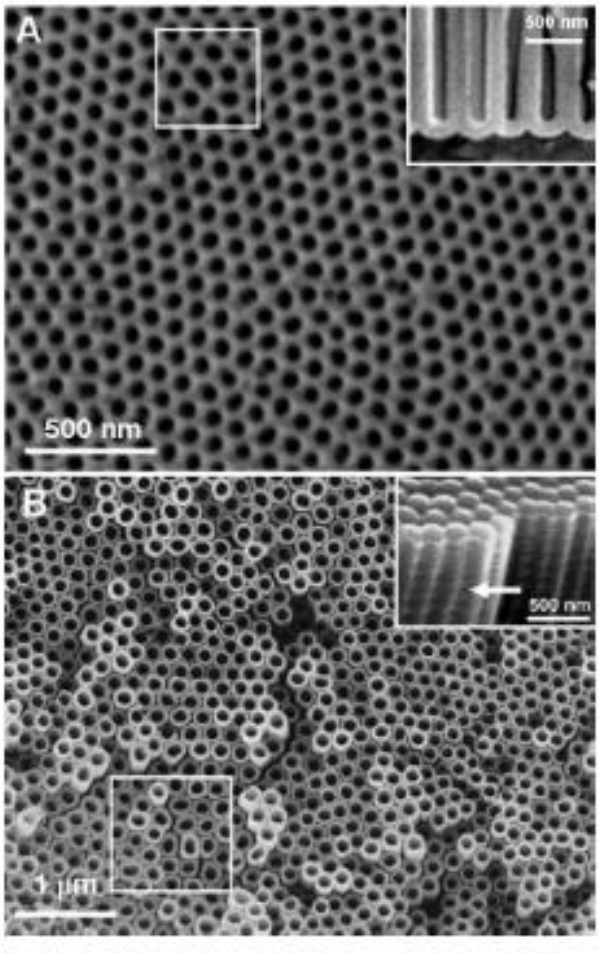

Figure 2.5. SEM Images of (A) AAO Template and (B) ATO Film [45]

Apart from these, researchers have also used radiation track-etched mica, nanochannel arrays on glass, mesoporous materials, zeolite, CNTs, etc. Further, bio templates such as DNA templates, central channel of tobacco mosaic virus have been studied.

2.5 Metal Nanowire Synthesis via Template-assisted Approach

Researchers have successfully synthesized nanowires and nanorods of different metallic materials via the template growth process. Various metal nanowires i.e. Ni, Co, Au, Ag, etc. have been synthesized using different templates with pore diameter from 10 nm to 200nm. Cheah[49] synthesized Al nanowires by a three-electrode deposition process using AAO templates. However, the nanowires were not evenly grown rather followed an "island-like" growth pattern. They argued that uneven growth can happen because of nucleation problems on the flat substrate as well as ununiformed pores. Schönenberger et al.[50] also reported that the channels in PC membranes can have a similar problem. They found that the pores are not cylindrical with consistent cross-section, rather have a cigar like structure. Leszek and co-workers[51] synthesized Ag and Sn nanowires that had varying aspect ratios using DC electrodeposition. They grew the nanowires inside AAO templates (with the thickness of 60nm) which were prepared from AA1050 alloy rather than expensive ultra-pure Al sheet.

Wang et al.[52] synthesized both Zn nanowires and Zn nanotubes using AAO templates. While Zn nanowires were synthesized via electrodeposition from Zn based solution, Zn nanotubes were prepared by heating induced volatilization method. For nanotube preparation, prepared Zn nanowires were heat treated in a tubular furnace under an inert atmosphere (in the presence of N_2). The temperature in the furnace was maintained above the melting point of Zn and was followed by slow cooling. During the cooling process melted Zn atoms start to nucleate on the high energy pore wall and form nanotubes gradually. However, they found, prior heating of as synthesized Zn nanowires,

and that there was no change of phase associated rather they have the same HCP structure all along. Only, the peak intensity decreases as the heating continues as shown in figure 2.6. They also found that this elevated temperature can increase the rate of nanotube formation from nanowires.

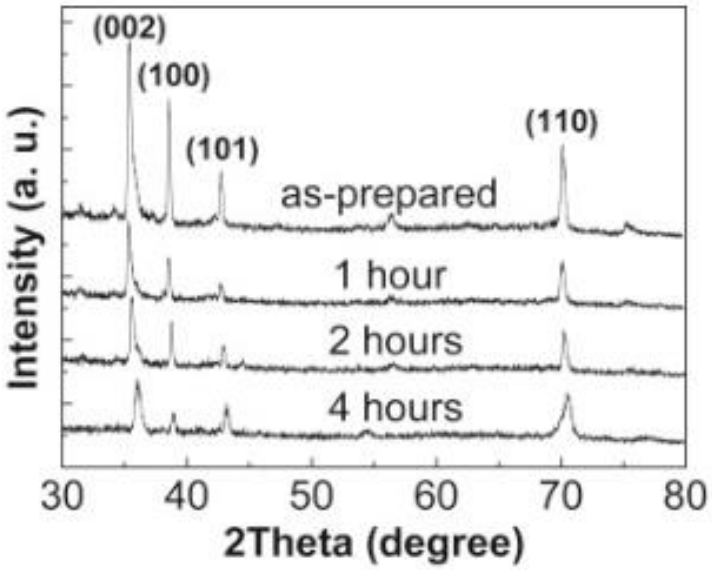

Figure 2.6. XRD of Synthesized Zn Nanowire after Heating at 500 ^{0}C at Different Time[52]

Shin et al.[53] prepared Cu nanowires at subzero temperature using alumina template with 20 nm pore diameter via potentiostatic electrodeposition with high pore filling (95%). However, due to the low temperature, the growth rate is much less as the growth inside the nanopores is governed by diffusion. Diffusion rate can be expressed by Fick's first law as $j = -D \Delta C$ where D is diffusion coefficient, j is diffusion rate and C is the local concentration. At low temperature, diffusion coefficient decreases according to Arrhenius plot[54] along with an elongated diffusion layer, which cumulatively decreases

concentration gradient and mass transport rate. They reported that, at higher temperature (60.5 ^{0}C) Cu nanowire growth rate is 745 nm/s, whereas at subzero temperature (-2.4 ^{0}C) it is only 45 nm/s[53].

Researchers have also synthesized nanowires using electroless deposition which needs chemical reagents to coat material on the surface of the template pore. In this process, the depositing material needs not to be conductive and deposition starts from the pore wall resulting in tubes and hollow fibrils. These are the main two differences compared to electrodeposition. Recently, Graves et al.[55] were able to synthesize Cu nanowires through electroless deposition process within 10 minutes inside PC membranes rather than AAO templates. They coated the back of the templates with a thin silver layer (≤15nm) which helps to catalyze electroless deposition. Cu nanowires with a length of 300-500nm were grown. However, the aspect ratio is not high as polycarbonate templates that had a pore size of 100nm and prolonged deposition caused a blistering effect on Cu nanowires. Zhang[56] et al. synthesized porous Au nanowire using AAO templates. They found that the morphology of nanowire is strongly affected by the current density and by adjusting the current density it is possible to transform solid nanowires into porous form. Fu et al. [57] produced Co and Pt nanowires using a three-electrode setup. They also synthesized CoPt alloy nanowires using the same process. Jin and co-workers[58] successfully synthesized single-crystal Bi nanowire with a high aspect ratio (>1000) via pulsed deposition techniques. Synthesis of Co_xNi_{1-x} alloy nanowires while varying the Co ratio was also reported by Vega et al.[59]. They grew nanowires in the nanopores of SiO_2 conformal coated hard-anodic aluminum oxide

membranes. They found that low Co ratio (≤0.51) leads to soft magnetic properties whereas nanowires with high cobalt content show increased magnetocrystalline anisotropy. Recently, ternary $Co_{12}Ni_{64}Fe_{24}$ compound nanowire growth through the three-electrode technique was reported by Atalay et al.[60]. They performed the electrodeposition for 180-300 minutes to get the nanowires and measured the magneto impedance. They found that the change in resistance is greater than the change in impedance and the maximum change in resistance (≈5.4%) occurs at 33MHz. Recently, Liakakos et al.[61] have reported the growth of single-crystal Co nanowire directly on Pt(111) film which was sputter deposited on Al_2O_3(0001) substrate through solution process reaction as shown in Figure 2.7(a). The cobalt nanowires with a diameter of 5-6 nm and length up to 960 nm were successfully synthesized. They found that the morphology of Co nanowire is not well defined at the Co-Pt interface and the broadening of diameter can happen as shown from HRTEM image in figure 2.7(b).

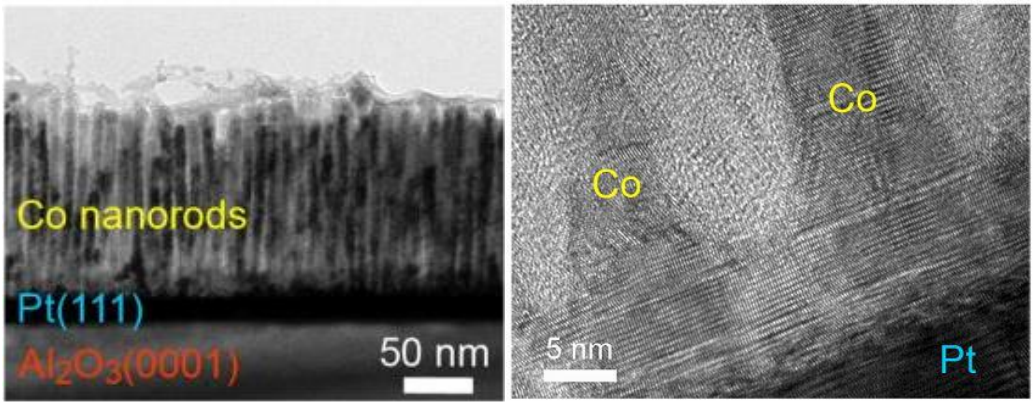

Figure 2.7. (a) TEM Image for the Cross-section of Co Nanowire Grown on Pt/Al_2O_3 Substrate; (b) HRTEM Image Showing the Base-broadening of Co Nanowire at Co-Pt Interface [61]

They also studied the magnetic hysteresis loop and found high density (up to 10 Tbits/in^2) and magnetic anisotropy (having KV value of 1300 k_BT; where T is 300 K and k_B is Boltzmann constant).

The majority of cited works on pure metal nanowires synthesized via TAE approach are compiled and summarized in Table 2.1.

Table 2.1. Template Assisted Pure Metal Nanowires

Mat[1]	**Type**	**Temp[2]**	**ECD Type**	**Dim. (D nm x L µm)**	**Deposition Bath**	**Ref**	**Remarks**
Ni Co	NW	AAO, Ion-track etched Polyamide, PC	Pot.[3]	10-100 x 1-60	$NiSO_4 \cdot 6H_2O + H_3BO_3$(Ni) $CoSO_4 \cdot 7H_2O + H_3BO_3$(Co)	[38]	
Ni, Co, Au, Cu	NR	PC	Pot.	10-200 x 6	$Ni(H_2NSO_3)_2.4H_2O$ + $NiCl_2.6H_2O + H_3BO_3$(For Ni); $CoSO_4.7H_2O + H_3BO_3$(for Co); gold(I) cyanide+ citric acid at pH 5-6 (For Au); $CuSO_4.5H_2O$ at pH 1 (for Cu)	[30]	Deposition voltage -1.2, -1.1, -1.0 and -0.2 V for Ni, Co, Au and Cu respectively
Al	NR	AAO	Pot.	200 x 2	[EMIm]Cl/ $AlCl_3$, molar ratio 1:2	[49]	CrO_3+ H_3PO_4 for template removal
Ag, Au, Sn	NW	AAO	Gal.[4]	80 x 1.5-17	Commercial Plating solution for Ag and Au; $SnCl_2$+ sodium Citrate for Sn	[51]	Template was prepared from AA1050 alloy (99.5% pure)
Zn	NW, NT	AAO	Gal.	Not provided	$ZnCl_2$+$ZnSO_4$ at pH 4-4.5	[52]	Graphite is used as anode

Cu	NW	AAO	Pot.	Not provided	$CuSO_4 \cdot 5H_2O + H_2SO_4$ + highly deionized water (18.2 MΩ cm)	[53]	Temperature range of -2.4 to 60.5^0C
Cu	NT	AAO	Elctless[5]	300 nm outer dia, length not provided	$CuSO_4 \cdot 5H_2O$+potassium sodium tartrate+ formaldehyde at pH value 7-8	[54]	Membrane modification by silane and sensitization-activation was done prior to deposition
Fe	NW	AAO	Pulsed	Not provided	$FeSO_4.7H_2O$+ H_3BO_3	[62]	Pre-plating of Cu NR, temperature 30 ^{0}C
Cu	Porous NW	AAO	Pot., Elctless	Not provided	$CuSO_4 \cdot 5H_2O + H_2SO_4$ +moderate stirring	[55]	Deposition voltage -75 mV vs SCE, deposition for 120 min
Bi	NW	AAO	Pot.	60 x 70	Bi $(NO_3)_3 \cdot 5H_2O$+ Glycerol + tartaric acid + KNO_3 at pH 2	[58]	Deposition voltage -0.05 V vs Ag/AgCl for 30 mins
Ni, Bi	NW	AAO	Gal.	50 x 50	Dimethyl sulfoxide solution containing $NiCl_2$ or $BiCl_3$ of 0.05M	[63]	N_2 gas purging during deposition and temperature 130 ± 5^0C
Pd	NW	Mesoporous silica	Pot.	$80A^0$ x 1	$PdCl_2$+HCl	[64]	2%HF used for template removal
Pd	NW	AAO	Pulsed	80 x 0.8	$Pd(NH_3)_4Cl_2$+ Palladure 150(commercial bath)+D.I. water	[65]	Current pulse -15mA and 1mA.Each pulse duration 0.1s
Cu	NW	PC	Pot.	Not provided	$CuSO_4$ at pH 2.0	[66]	Potential -400mV vs Cu applied
Zn	NW	AAO, PC	Pot.	40-100 x 6	$ZnCl_2$+KCl+gelatin	[67]	-0.7V and -1.5 V vs SCE
Cu	NW	AAO	Pot.	60 x 25	$CuSO_4 \cdot 5H_2O$+ H_3BO_3 at pH 4.5-5.0	[68]	-1.5 V, 10-20 mins at room temperature
Co	NR	AAO	Pot.	20,50,120 x 50 nm	$CoSO_4$.$7H_2O$+$CoCl_2$ $6H_2O$+ H_3BO_3	[69]	
Ni	NW	AAO	Gal.	200 x 20	Nickel sulfamate solution	[2]	Temperature at 35^0C
Ag	NW	AAO	Gal.	180-400 x 30	Commercial bath Silver 1025,	[70]	Room temperature, Current density $10mAcm^{-2}$

Co, Pt	NW	AAO	Pot.	200 x 60	$CoSO_4$ at pH 3.0 (For Co) platinum-p-salt ($Pt(NH_3)_2(NO_2)_2$) (Fo Pt) at pH 6.5	[57]	0.222 V vs Ag/AgCl electrode Pt as counter electrode
Fe	NW	AAO	AC ECD	55 x 1	$FeSO_4$ .7H2O+boric acid+ ascorbic acid	[71]	Room temperature, ac voltage 5-60V, frequency 300 Hz

[1]Mat= material, [2]Temp=template, [3]Pot. = potentiostatic, [4]Gal. = Galvanostatic, [5]Elctless= electroless,

*NW= Nanowire, NR=Nanorod, NT= Nanotube

Though several works have been done with TAE of metal nanowires, it is still not widely explored how different processing conditions, namely, temperature, current density, external force, etc. can affect the nanowire properties. In this work, the effect of current density and temperature on template-assisted Cobalt nanowire morphology and other physical properties have been discussed.

2.6 Methodology

Synthesis of nanowire via template-assisted electrodeposition method consists of three individual steps i.e. template preparation (by depositing a thin conductive metal film to make them as an active electrode), preparation of electrodeposition bath, removal of nanowires from the template. A typical synthesis process comprising these steps is illustrated in figure 2.8.

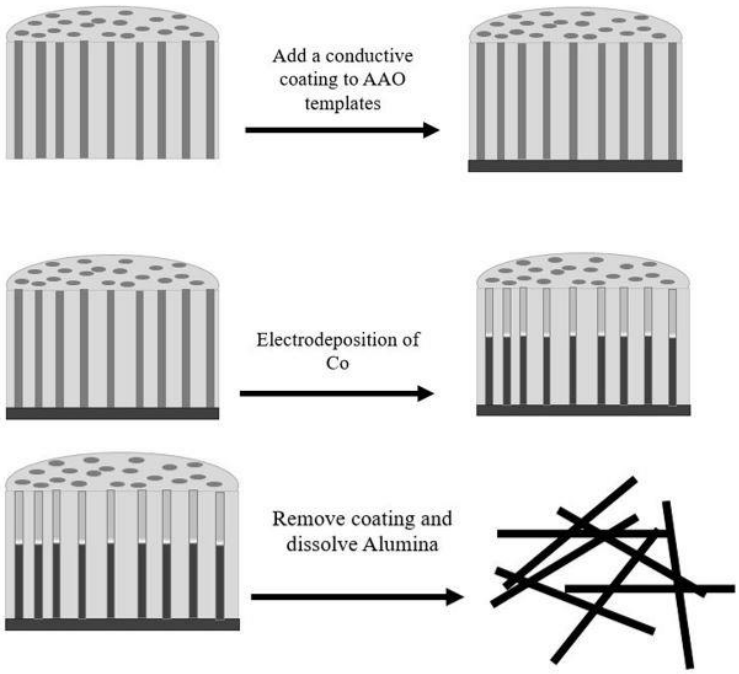

Figure 2.8. Schematic of Template-assisted Deposition of Nanowire

In the present work, 1-D Co nanowire arrays were prepared by galvanostatic electrodeposition of Co ions into commercially available alumina oxide template, Anopore® (Whatman, Germany) with a diameter of 200 nm. The templates were thoroughly cleaned with DI water and dried in the air prior to use. To make the templates conducting and an active cathode, a conductive layer of Al with an approximate thickness of about 800 nm was deposited on one side (using Kurt J. Lesker, PVD 75 system).

A special holder was fabricated via 3D printing technology with precise span distance (20 nm) and alignment of the arms as shown in figure 2.9. The template then was attached to a double-sided copper tape and used as a cathode in an electrodeposition bath.

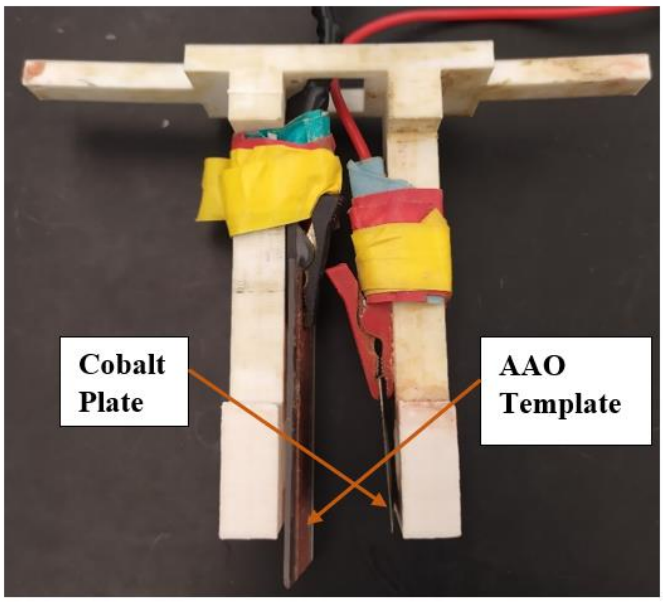

Figure 2.9. 3D Printed Sample Holder

An ultrapure cobalt plate (Sigma Aldrich) was used as an anode. The deposition bath consists of $CoSO_4.7H_2O$ (1 mol/L) and boric acid (45 g/L). Boric acid (H_3BO_3) works as a buffering agent for the electrodeposition solution. However, some recent reports suggest that it has catalytic effects on the electrodeposited metal ions also[72]. The holder is then placed in the deposition bath to start the synthesis process as shown in figure 2.10. A Kiethley 2602A type source meter was used to supply constant current density. A hot plate equipped with magnetic steering facility was used to control the bath temperature and a thermocouple type thermometer (Amprobe) was used to measure the temperatures. As mentioned earlier, properties of Co nanowires are significantly affected by solution pH, agitation, additives, external magnetic field, current density, and temperature and deposition time.

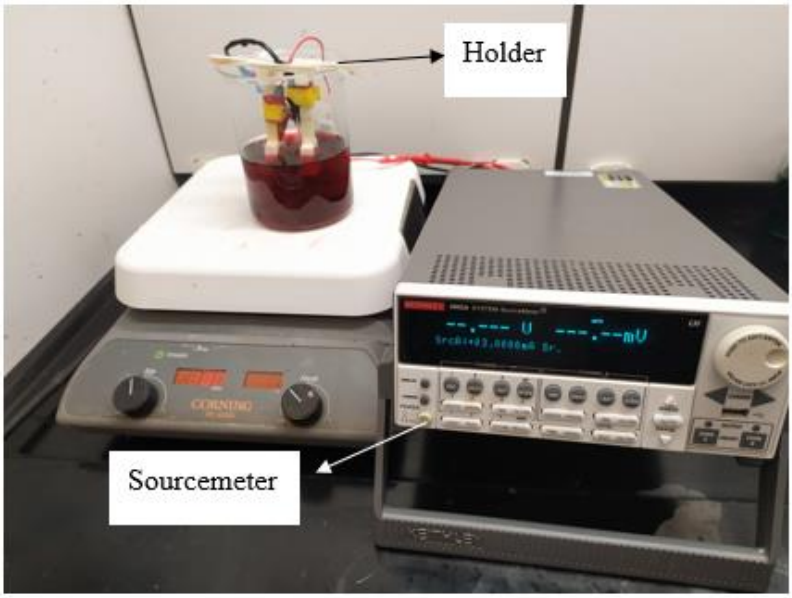

Figure 2.10. Experimental Electrodeposition Setup for Co Nanowire Synthesis

In this research, all the processing parameters i.e. bath composition, pH, deposition time, etc. were kept constant while bath temperature and depositing current density were varied accordingly. All these parameters are listed in Table.2.2.

Table 2.2. Electrodeposition Parameters

Parameter	**Value**	**Units**
Temperature	25 (RT), 35 and 50	°C
Current density	3, 5 and 7	$mA.cm^{-2}$
Solution pH	4.2-4.8	N/A
Agitation	100	rpm
Deposition time	60	Minutes

After depositing for 1 hr. the templates were rinsed with water and dried. The templates are dissolved completely into a 5M NaOH solution and kept overnight to ensure complete dissolution and yielding free nanowires. Alumina is an amphoteric oxide which reacts in both acidic and basic solution. The dissolution of the alumina membrane in a basic solution is occurred by the following reaction (equation 2.3).

$$Al_2O_3 + 3H_2O + 2NaOH \rightarrow 2\ NaAl(OH)_4 \qquad (2.3)$$

Yielded nanowires were then washed several times using magnetic decantation technique along with Ultrasonication to get well-dispersed nanowires. This step is important as it helps to remove NaOH which makes the nanowires to stick to one another as shown in figure 2.11.

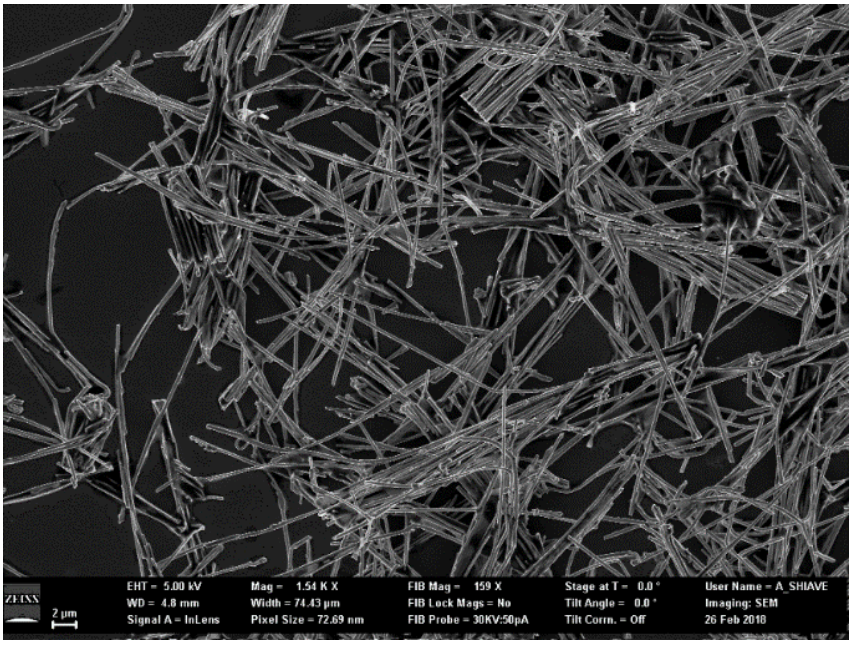

Figure 2.11. Co Nanowire after Synthesis

However, care should be taken during Ultrasonication as prolonged sonication can affect the mechanical integrity of the nanowires. Finally, the grown nanowires were stored in methanol to avoid any further oxidation.

2.7 Results and Discussions

Figure 2.12 shows regularly arranged nanopores of an AAO template where we can see the pore diameter is above 200 nm and are not always in a circular shape. The thickness of Anopore® template is 30 μm. Besides these, we also found branched structures at the bottom of the pore; these were also found in synthesized nanowires reported by other researchers. The diameter of our synthesized nanowires is 230±30 nm which is more than the average diameter of template pores.

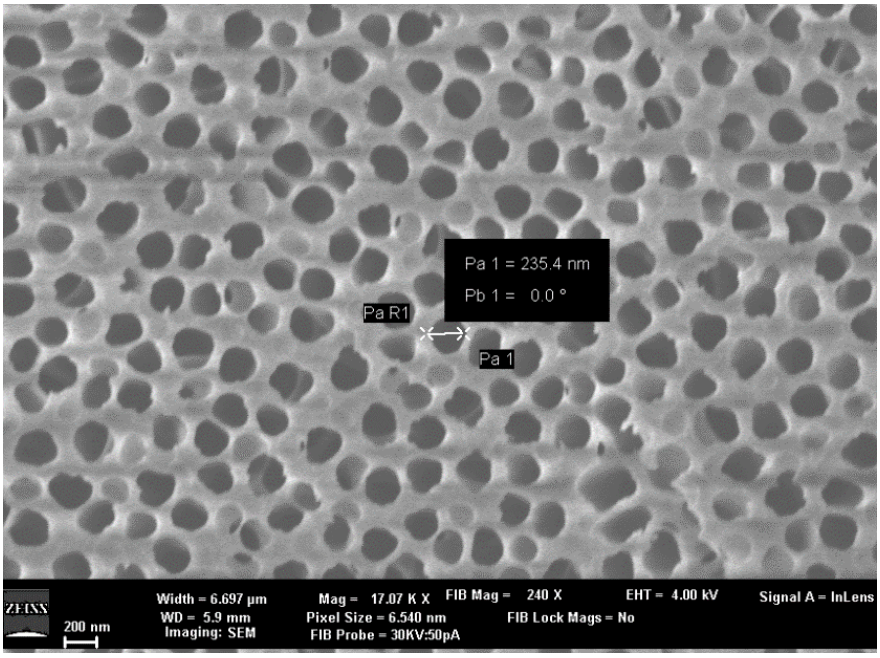

Figure 2.12. Nanopores of AAO Template

This increase in diameter can potentially be attributed to the post-synthesis oxidation. The length of nanowires was found to be 15-25 μm, which is mainly dependent on deposition time. The final length of nanowires is consistent with the template thickness, which means that the nanowires kept their mechanical integrity during the cleaning, separation, and sonication process. The morphology of Cobalt nanowires at varying current density and temperature are discussed next. It is to be mentioned that, in all the cases, nanowires were found to be branched which can be attributed to the branched nature of template pores.

2.7.1 Morphological Study of Co Nanowire

Morphological study of Co nanowire was done using Carl Zeiss Auriga FESEM. This study was done qualitatively by observing the nanowire surface using SEM images. Prior to imaging, the nanowires were dropped on SEM holder (on carbon tape) and were left for drying in the air for 15 minutes to remove methanol.

As the nanowires are metallic hence providing conductive target, no further sample preparation is required for SEM analysis. In all the cases, the imaging was done by 4 kV beam source, with 80 K magnification, tilt angle of 0.0^0, 2.9 mm working distance, and in-lens detector for useful comparison. Figure 2.13- figure 2.15 shows the morphological characteristics of deposited Co nanowire in various operating conditions i.e. bath temperature and current density.

Figure 2.13 (a)-(c) shows the surface morphology of as-grown Cobalt nanowire at room temperature ($25\ ^0$C) for varying current densities of 3 mA.cm^{-2}, 5 mA.cm^{-2} and

7 mA.cm^{-2} respectively. From these figures, we can see that the surface of nanowires at low current density (3 mA.cm^{-2}) is smooth which tends to roughen as the current density increases (figure 2.13(a)- figure 2.13 (c)) and at 7 mA.cm^{-2} the surface of the nanowires becomes the roughest. We can also see that at 7 mA.cm^{-2} current density, nanowire surface contains "island" like texture which gives the increased surface roughness and is not seen in lower current densities. Additionally, the nanowires show some distorted shape rather than perfect circular. These are the features associated to the template pore walls as the shape of the nanowire is a perfect replica of the templates.

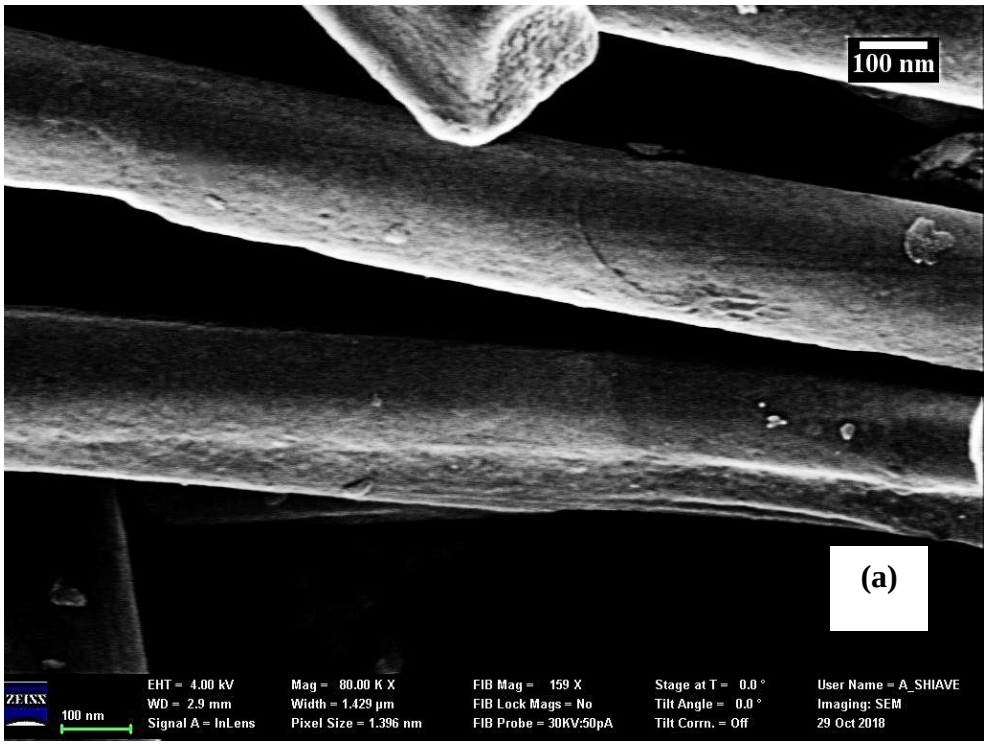

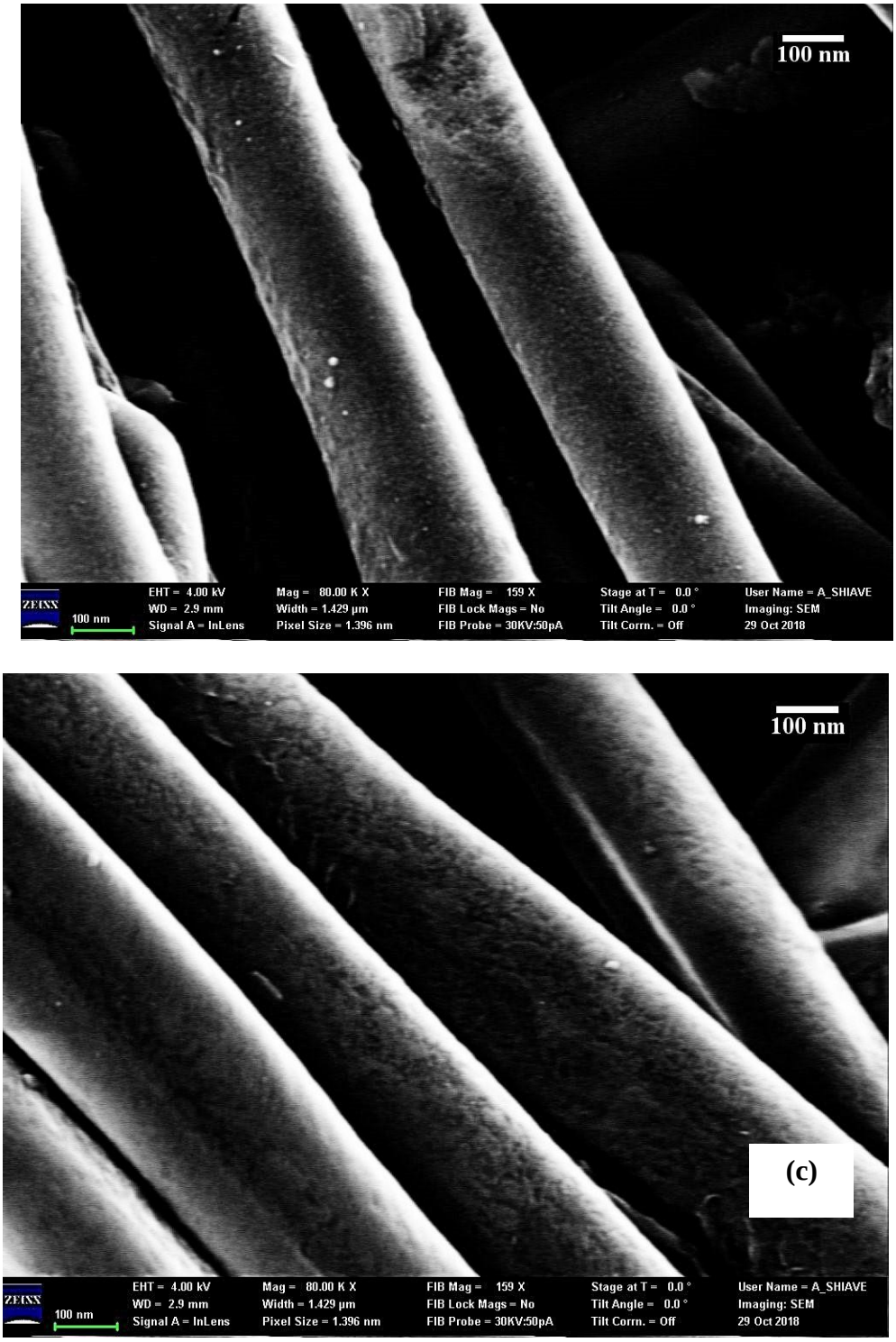

Figure 2.13. SEM Images of Cobalt Nanowires Grown at Room Temperature (25 ^{0}C) at Varying Current Density. (a) 3 mA.cm^{-2}, (b) 5 mA.cm^{-2} and (c) 7 mA.cm^{-2}

Figure 2.14 (a)-(c) and presents the surface morphology at 40 ^{0}C for current densities 3 mA.cm^{-2}, 5 mA.cm^{-2} and 7 mA.cm^{-2} respectively. The surface of the nanowires is not as smooth as RT for lower current densities. However, a similar trend of increasing roughness is seen in this case also. It is to be noted that, the area of individual "island" at 7 mA.cm^{-2} is smaller than that of RT nanowires. Figure 2.14(c) shows some wavy net-like structure on the edge of nanowires (as pointed out) which may come from unwashed NaOH solution.

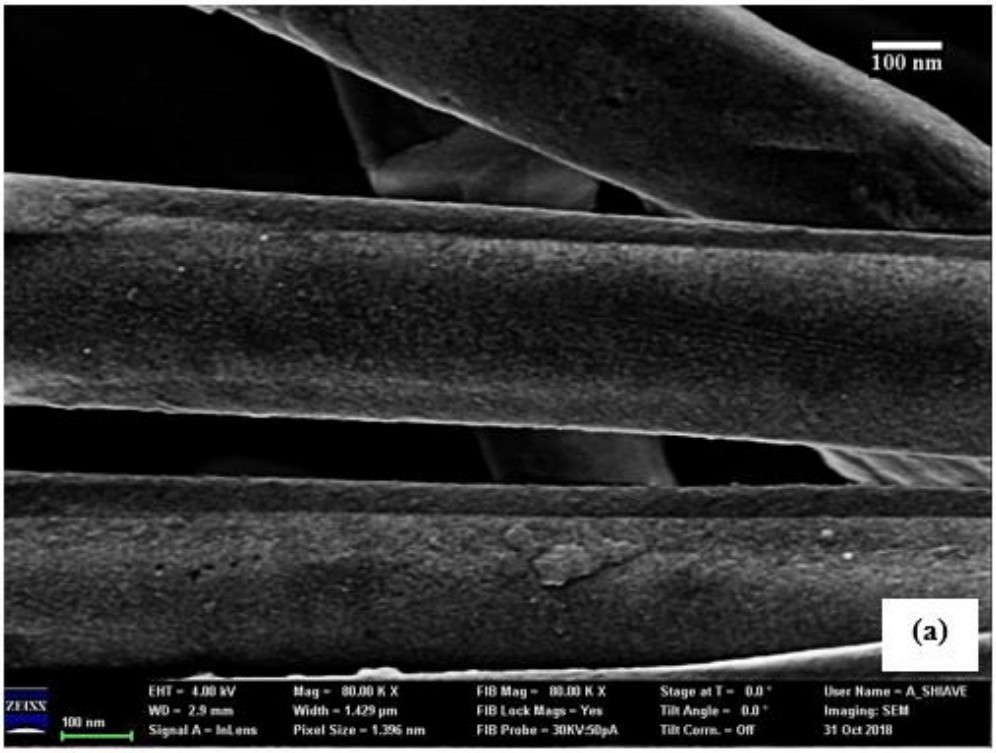

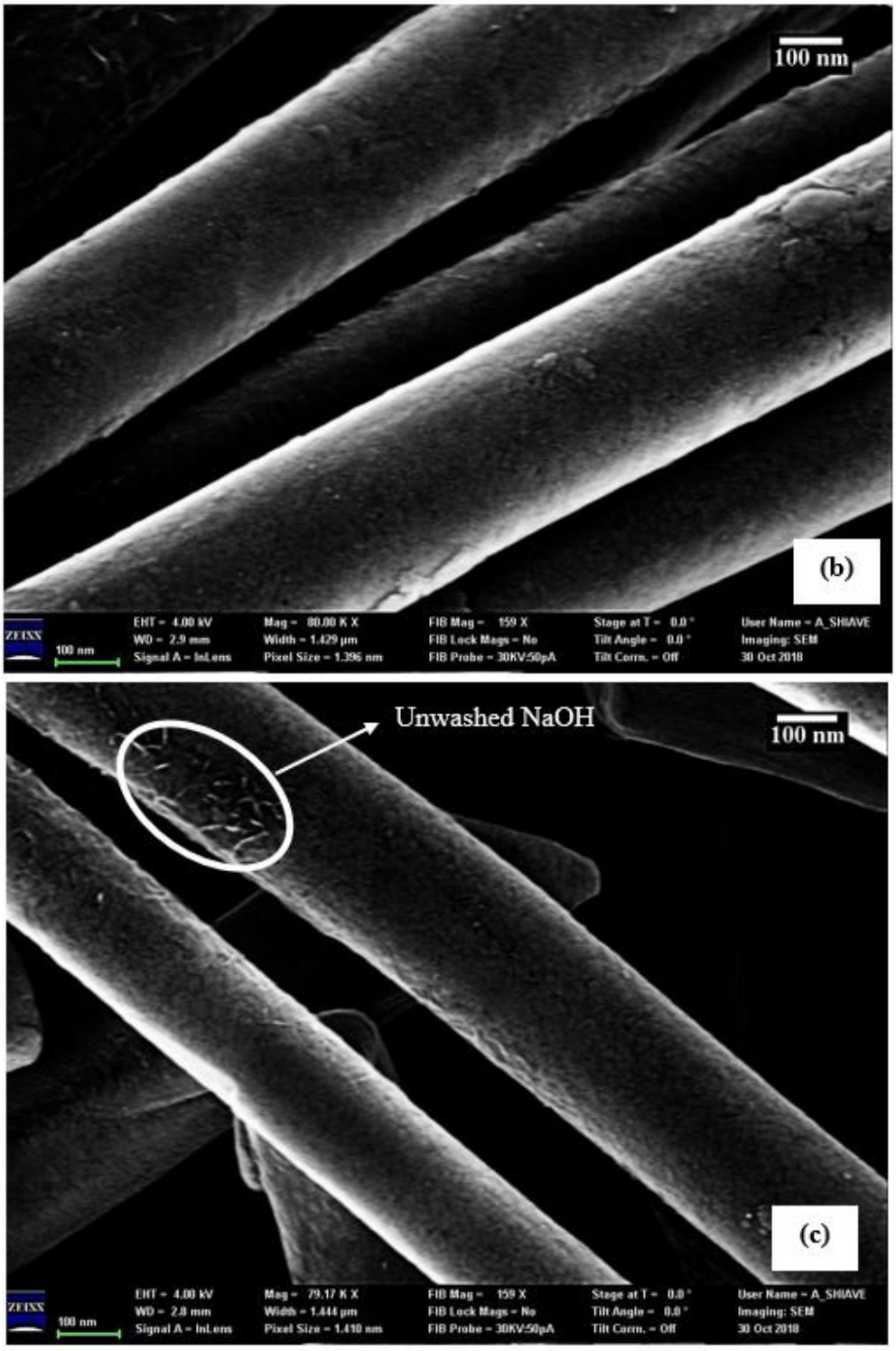

Figure 2.14. SEM Images of Cobalt Nanowires Grown at 40 ^{0}C Bath Temperature for Varying Current Density. (a) 3 mA.cm^{-2}, (b) 5 mA.cm^{-2} and (c) 7 mA.cm^{-2}

Figure 2.15 (a)-(c) shows the morphology at 50 ^{0}C for current densities 3 mA.cm^{-2}, 5 mA.cm^{-2} and 7 mA.cm^{-2} respectively. We can see that the surface roughness is the highest in this case, and the area of the "islands" is the smallest compared to previous cases. However, surface roughness increases as current density increases as we can see in Figure 2.15 (a) to Figure 2.15 (c). At a current density of 7 mA.cm^{-2} we found lots of small grainy structures. We can also see the nanowires are not completely circular tube rather some irregularities of shapes are also found. However, the diameter of these nanowires was fairly constant other than these regions.

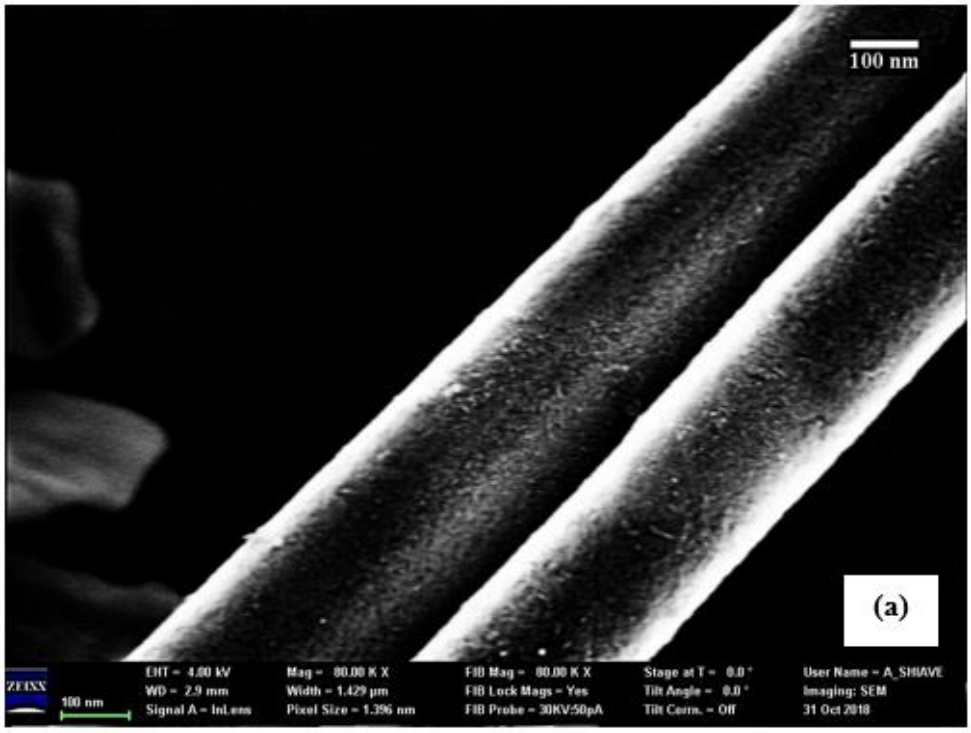

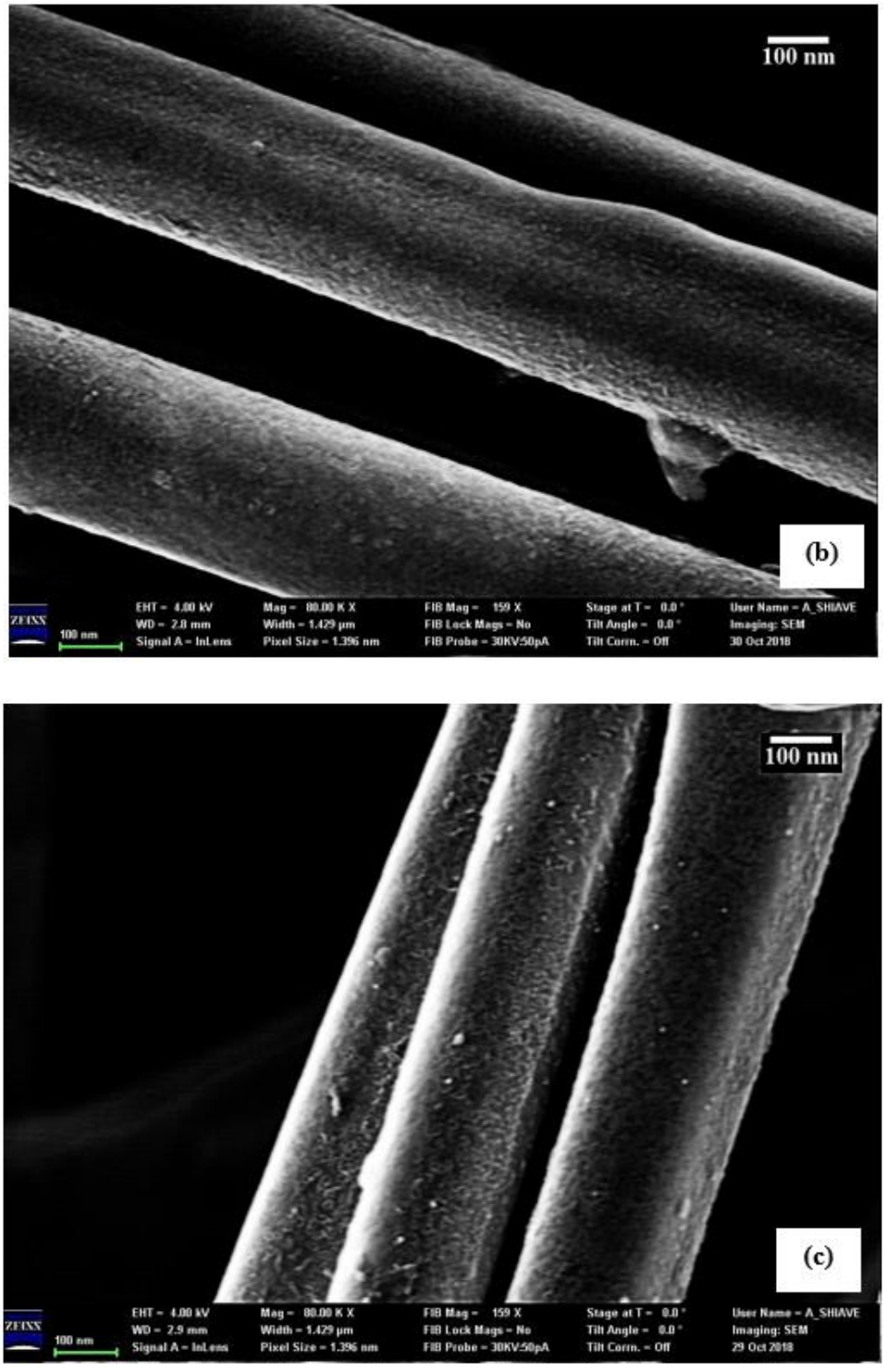

Figure 2.15. SEM Images of Cobalt Nanowires Grown at 50 ^{0}C Bath Temperature for Varying Current Density. (a) 3 mA.cm^{-2}, (b) 5 mA.cm^{-2} and (c) 7 mA.cm^{-2}

We also found some broken nanowires in all the cases, which may arise from ultra-sonication while releasing them from templates. To avoid inconsistency in the cleaning process, we used ultra-sonication for 10 minutes for all the samples. However, we also found that if ultra-sonication time is less, there is less possibility of dispersing the nanowires, as NaOH tends to agglomerate nanowires in bunches. Longer ultra-sonication can lead to well-dispersed free nanowires though the possibility of nanowire breakage is higher because of high shear exerted on the nanowires.

2.7.2 EDS Analysis

The study of nanowire purity was done using energy dispersive spectroscopy (EDS) analysis. The analysis is shown in figure 2.16 and the results are compiled in table 2.3.

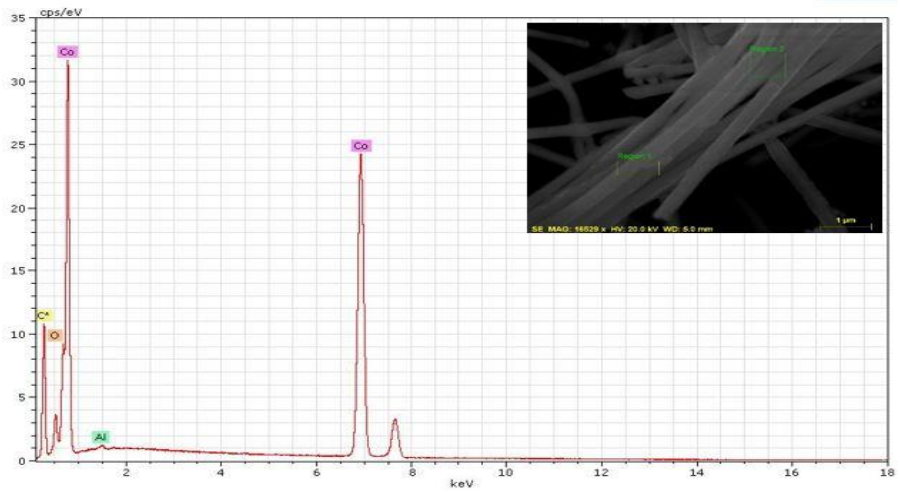

Figure 2.16. EDS Analysis of Cobalt Nanowire

Table 2.3 EDS Elemental Analysis

Elements	**Weight (%)**	**Atomic (%)**
Co	96.97	89.85
O	2.89	9.85
Al	0.15	0.30
Total	**100.00**	**100.00**

From the result, we can see that the purity of these nanowires is very high (~97 wt% cobalt). Small amounts of Al and O present could be from undissolved alumina membrane and oxidation, respectively.

2.7.3 Mass of Grown Nanowire

The weight of grown nanowire with different processing parameters was also studied as shown in Figure 2.17. As the mass is very small, it is not feasible to weigh the nanowires after complete removal from the template. That is why, each time before electrodeposition, the Al coated templates were weighed with the help of a microbalance. Following the deposition for 1 hour, the templates were washed carefully with acetone to remove any adhesive on the back of the template which might come while loading it on the double-sided copper tape. The templates were then dried and weighed again. The difference in weight gives the final mass of nanowires produced in each run. The same process was repeated 5 times.

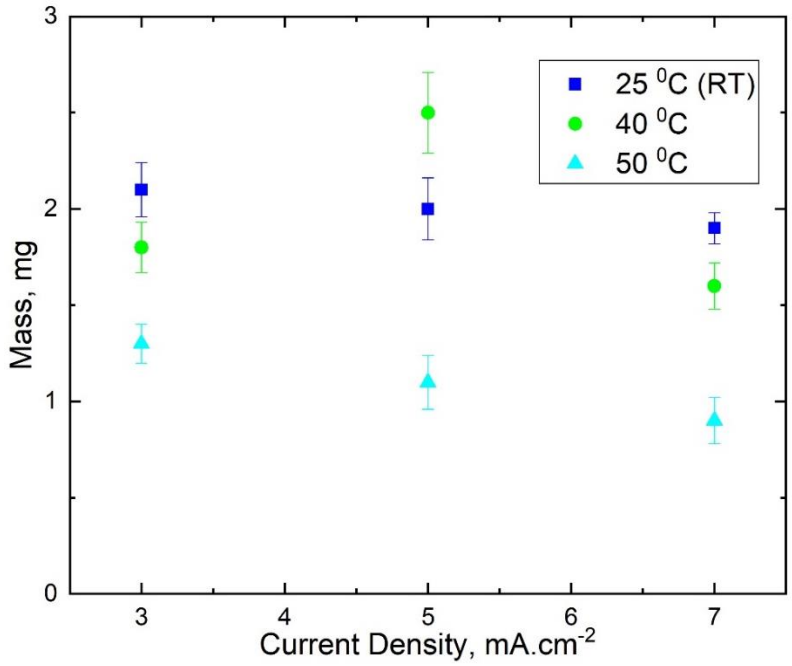

Figure 2.17. Nanowire Mass at Different Operating Conditions

From the figure, we can see that the maximum amount (2.6 ± 0.2 mg/each run) of nanowire is produced if the bath temperature is 40 ^{0}C at 5 mA.cm^{-2} current density. However, produced mass at each run is very low which is one of the drawbacks of TAE. Generally, with the increase in bath temperature at constant current density, fewer nanowires are produced. At RT the mass of produced nanowires is maximum for all current densities except for 40 ^{0}C and 5 mA.cm^{-2}. If the temperature rises, the mass of produced nanowires becomes lower in general. This may occur as high temperature creates extra energy which in turn increases ion mobility. Increased ion mobility incurs more collision between two adjacent Co^{2+} thus stopping more ions to go into template pores. Additionally, at high-temperature parallel hydrogen evolution reaction occurs which in turn decreases the electrodeposition efficiency up to 60%[73]. However, we do

not see any clear relation between current density and nanowire mass from figure 2.17 though we can see that there is a general decrease in nanowire mass if the current density is increased. We found that at 40 ^{0}C bath temperature, the maximum amount of nanowires is synthesized for all values of current density employed in the present work.

2.7.4 Length of Grown Nanowires

The length of as grown Co nanowire was studied to find out the effect of these processing conditions. Deposition of nanowires inside the nanopores is a purely diffusion-controlled process[74] where the diffusion rate (j) can be expressed according to the Fick's law (equation 2.4).

$$J = -D\Delta C \tag{2.4}$$

Here, D is diffusion coefficient and ΔC is change in local concentration. An increase in bath temperature increases the diffusion coefficient of Co cations which in turn increases the growth rate. From the equation, we can infer that nanowire length can be mostly affected by bath temperature rather than current density. That is why we only considered the condition when the current density is 5 mA.cm^{-2} as it gives maximum yield for most of the cases. We compared the lengths after 10 minutes, 30 minutes, and 60 minutes time intervals at different bath temperatures as shown in Figure 2.18(a). Nanowire growth rate trend (95% confidence) with different deposition time and temperature is also shown in Figure 2.18(b). We can see that the average NW growth rate for high temperature is the lowest, while for RT and 40 ^{0}C growth rate is higher. The maximum growth rate of 1.07

μm/ min can be attained at 50 ^{0}C after the first 10 minutes of nanowire deposition which we can see in figure 2.18(b). In fact at high temperature, the ion movement rate is higher which drives the ions to the suitable nucleation sites faster and get reduced. We also saw that the nucleation and growth of nanowires in each pore does not start at the same time and at high temperatures the possibility of hydrogen evolution reaction increases which minimizes energetically suitable nucleation sites. However, because of higher ion mobility, the growth rate becomes high and the length of nanowire is higher initially for 50^0 C bath temperature condition compared to low temperatures (at RT, 0.77 μm/ min and 0.96 μm/min for 40 ^{0}C) albeit less number of nanowires due to less mass of nanowires formed. That is why at the high temperature we get fairly long nanowires though the overall yield is low. On the other hand, because of low hydrogen evolution at lower temperatures, the number of suitable nucleation sites is high and nucleation starts for a greater number of nanowires filling more pores.

However, after the first 10 minutes of deposition, the growth rate drops for all bath temperatures. From both of these figures, we can see that the biggest drop in growth rate (79 nm/min) occurred for 50^{0}C whereas the growth rate does not drop much for room temperature (0.6496 μm/min for RT). For nanowires at 40 ^{0}C the growth rate also decreases to 0.3 μm/min. Because of continued high growth rate, nanowire length continues to increase at a faster rate (at low synthesis temperature for 30 minutes of deposition) as shown in Figure 2.18(a and b).

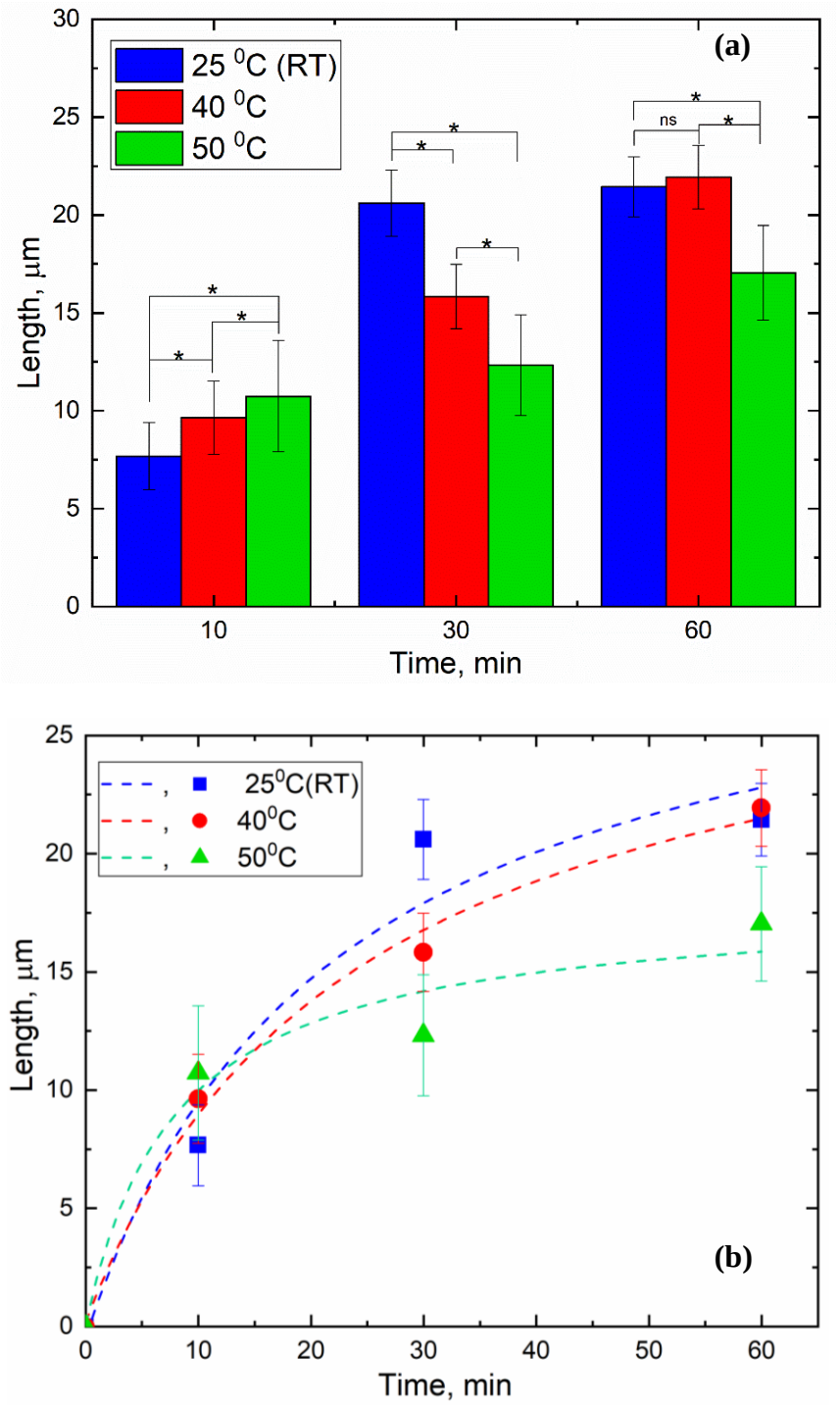

Figure 2.18. (a) Length of Nanowires, (b) Growth Trend at Different Bath Temperatures. Statistically Significance Level is Marked in (a) (* =significant (p<.05), ns = not significant)

Finally, the growth rate drops for all the cases, especially because of less potential difference between the anode and on-growing Co nanowire tip at the cathode. We found that, 40 ^{0}C bath temperature yields maximum length of nanowire after a full 60 minutes of deposition. We can also see that; the nanowire lengths vary from each other even for at a certain temperature (error bar calculated using standard deviation). The variation of length is higher for high bath temperature. Because at high bath temperature, ion transport rate is enhanced which in turn facilitates two main reasons for non-uniform nanowire growth i.e. cation transportation from the bulk electrolyte to the pore entrance and transportation along pore channels. At low temperature, constant diffusion of excess cations from the bulk solution makes sure that the cations are concentrated at the template edges as hemispherical diffusion layers are formed at those regions[75]. On the other hand, variation in pore diameter and the presence of defects inside the pore can also lead to non-uniform growth[75], [76]. Shin et al.[53] also reported that subzero bath temperature can yield 95% length uniformity which will reduce the SD value whereas at high temperature it is only 65%.

Comparing these results, we can conclude that, 40 ^{0}C bath temperature is the most favorable operating condition for maximum yield, as well as nanowire length.

2.8 Conclusion

We have successfully established a facile route to synthesize Cobalt nanowire via template-assisted electrodeposition method. As the quality and properties of electrodeposited products (nanowire in this case) can be affected by different processing

conditions, we studied the effect of temperature and current density on the physical properties of Co nanowire. We found that the surface morphology at low current density and temperature is smooth while an increase in both of these conditions increases the surface roughness. However, comparing the morphological images we can conclude that current density has a more dominant effect on surface roughness rather than temperature. EDS analysis reveals that the nanowires are of high purity (97% Co). We also found that bath temperature and current density can affect the nanowire yield as well as the length of nanowires. At 40 ^{0}C bath temperature, the maximum yield of nanowires was found irrespective of current density. Higher bath temperature can aid in faster initial growth. However, because of parallel hydrogen evolution, after some time the growth rate drops significantly compared to low bath temperature, and efficiency of the process decreases.

One of the main drawbacks of TAE is the crystallinity of nanowires as many researchers reported that the final nanowires are polycrystalline in nature, though some researchers reported that it is possible to get single crystalline nanowire via precise control of the processing conditions. So far we found that the nanowires are well structured and free-standing at varying processing conditions. We need a better understanding of the growth process of these nanowires which is mostly governed by the crystal structure. An in-depth study of Co nanowires structure is necessary as the processing conditions can affect the crystal structure also. The following chapter will focus mainly on the crystallographic orientation and growth mechanism of Co nanowire.

CHAPTER III

CRYSTALLOGRAPHIC STUDY OF COBALT NANOWIRE

3.1 Introduction

Template-assisted electrodeposition is one of the most versatile and popular methods to synthesize free-standing nanowires with precise control over dimensions. However, there are some challenges needed to be overcome i.e. selection of suitable templates and proper operating conditions, the crystallinity of formed nanowires, etc. Though it is possible to get single crystalline nanowire through this approach (e.g. very high temperature), most of the researchers reported nanowires are polycrystalline in nature. It is very important to find suitable conditions to synthesize single-crystalline nanowires because of their versatile application potentials. The crystallinity of nanowires is mainly governed by the growth mechanism and therefore a clear understanding of the growth mechanism is necessary. In this chapter, we will focus on the crystallographic study of template-assisted cobalt nanowires, and the effect of various processing conditions i.e. temperature and current density on the crystallographic orientation using various characterization tools i.e. X-Ray diffraction (XRD), Transmission electron microscope/ High resolution TEM (TEM/HRTEM) and selected area electron diffraction (SAED). In addition, detailed crystallographic study was performed to understand the growth mechanism for these nanowires.

3.2 Crystallographic Characterization Techniques

3.2.1 X-Ray Diffraction (XRD)

XRD is a simple and easy characterization technique to analyze crystalline solids which gives valuable information about lattice constants and geometry, defects in the samples, material identification, defects, size of powder samples, stresses, the orientation of single crystals and preferred orientation of polycrystals, etc. All crystalline solids (apparently 95% of all solid materials) have their own patterns and the same substance gives the same pattern all the time, even if they are in mixture with others which act like fingerprint[77]. A collimated X-ray beam with a specific wavelength is incident on a sample and is diffracted by crystalline phases present in the specimen following the Bragg's law(equation 3.1) [77]

$$n\lambda=2d\sin\theta \tag{3.1}$$

where λ is X-ray wavelength, d is spacing between planes in the crystalline sample, and θ is the angle between incident X-ray and diffraction plane. For constructive interference, the value of n must be an integer. The diffraction process is shown in figure 3.1. Interplanar spacing d can be calculated from Miller indices (hkl) as given by equation 3.2

$$d_{hkl} = \frac{a_0}{\sqrt{h^2+k^2+l^2}} \tag{3.2}$$

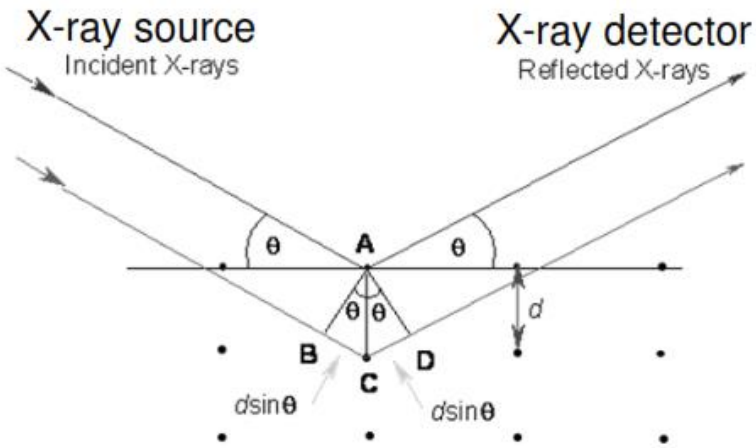

Figure 3.1. Bragg's Law of Diffraction

Where a_0 is the lattice parameter. And the (hkl) diffraction peak occurs at $2\theta_{hkl}$ as the following equation (3.3)

$$2\theta_{hkl} = 2\arcsin\left(\frac{\lambda\sqrt{h^2+k^2+l^2}}{2a_0}\right) \tag{3.3}$$

The positions of the diffracted peak can be measured accurately using XRD thus making it the best method for analyzing homogeneous and inhomogeneous strains[78]. Homogeneous elastic strain shifts the diffracted peak position and the change in d-spacing can be calculated resulting in the change of lattice constant under strain. In the absence of inhomogeneous strain, size of the crystallite, D, can be measured from peak width using Scherrer's formula[79] as followed (equation 3.4)

$$D = \frac{K\lambda}{B\cos\theta} \tag{3.4}$$

Here, λ is X-ray wavelength, B is the full width of height maximum (FWHM) of a diffraction peak (radians), θ is diffraction angle and K is the Scherrer's constant or shape factor (for spherical crystallite, K=0.9).

3.2.2 Transmission Electron Microscopy and Selected Area Electron Diffraction

Transmission electron microscopes comprise an electron source by which the electrons are accelerated down the TEM column followed by electromagnetic coils, lenses, and apertures which help to formulate images which then finally are projected on a fluorescent screen for observation. A typical TEM setup is illustrated in figure 3.2.

Electrons are accelerated through the column by high voltage difference produced by the electron gun. Three types of electron sources are possible i.e. Tungsten hairpin, lanthanum hexaboride, and field emission which have corresponding advantages and disadvantages compared to others. The setup of TEM is somewhat similar to SEM while the main difference is that the sample must be thin and electronically transparent for TEM. Transmitted electrons are then processed and projected on the screen to be configuration and finding defects in the samples. The main challenge for using TEM is to prepare a suitable sample, as it needs to be very thin (<100nm). Selected area electron diffraction commonly known as SAED or SAD is another technique that is used for crystallographic study in TEM environment. In this process, high energy electrons pass through thin TEM sample and are treated as waves.

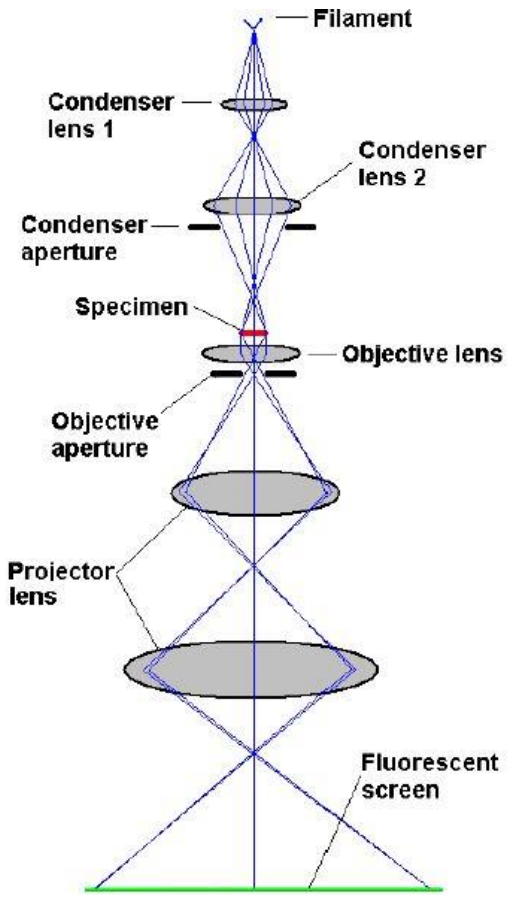

Figure 3.2. Typical TEM Setup

TEM study helps us to get better resolution, atomic. The wavelength of this high energy electron can be hundredth times lower than the lattice spacing of TEM sample. While passing the samples, electrons are diffracted as sample atoms act as a diffraction grating. Each plane with specific atom orientation gives individual diffraction pattern and can be observed in the screen of TEM as an ordered diffraction spot (for single crystalline material) or polycentric ring (for polycrystalline material). In this way, the crystallinity of the sample can be identified.

3.3 Focused Ion Beam (FIB) aided TEM Sample Preparation

For TEM analysis, the sample should be very thin (<100 nm) which is not always possible for nanowires. Nanowires having higher diameters or having segments of different materials should be prepared separately for TEM/HRTEM analysis. For TEM sample preparation, the most common techniques used are in-situ lift-out method, traditional H-bar technique, plan view lift out and H-bar lift-out technique, and direct lift-out technique[80]. These techniques are discussed in brief here.

3.3.1 H-bar Technique

This traditional approach has been practiced by researchers for a long time where a small sample is cut from the bulk sample with the help of a diamond cut-off saw. To minimize the mechanical damage of cutting as well as to make a flat sample, both sides of the sample is polished with a polisher followed by the mounting of sample on TEM grid with the help of epoxy and is allowed to cure. Finally, the sample is polished so that the thickness of the sample becomes less than 100 μm which will help to reduce FIB milling time. This technique is useful mostly for non-site-specific specimen and sometimes for site-specific specimen. However, care should be taken during the thinning and polishing process to keep the mechanical integrity of the sample intact.

3.3.2 Lift-out Technique

The most commonly used and popular technique for TEM sample preparation via FIB is “Lift-out technique” as samples can be prepared directly from the bulk sample,

and cutting and mechanical polishing is not needed. In this process, the zone of interest is first protected with metal deposition (tungsten, platinum, etc.) followed by the milling around the sample with thickness less than only 100 nm. A micromanipulator is then used to put the sample on the TEM grid via in-situ or ex-situ lift-out. The main advantages include (1) minimum mechanical damage, (2) reduced X-ray signals, (3) fragile and contamination prone samples can be prepared. This method is versatile and efficient where traditional H-bar technique is not suitable especially for ferromagnetic materials. However, once the sample is transferred to the TEM grid, re-thinning of the sample cannot be done.

3.3.3 Plan-view Lift-out and H-bar Lift-out Techniques

The main challenge during the lift-out process is the loss of samples as charge at the glass needle tip might repel the sample and cause “sample fly-off” from the tip. On the other hand, if the charge is too high then unloading the sample can be difficult. To solve this problem Patterson et al.[81] combined H-bar and lift-out technique. In this technique, a thicker slab (4 μm) with a sample feature is cut from the bulk sample and positioned and glued on a modified TEM grid using a micromanipulator tip. Finally, a sample of suitable thickness can be prepared in the FIB microscope. The advantages of these techniques are (1) lesser possibility of losing sample, (2) re-thinning of sample is possible, (3) suitable for Plan-view samples.

3.4 Growth Characteristics of Metal Nanowire

Determining the growth rate of 1-D nanostructures is important prior to other characterizations. The crystal growth rate in template pores is modulated by 2D growth mechanism which is kinetics dominated deposition process[82] and various growth modes are shown in figure 3.3(a, b and c). In all these figures, green atoms are nucleus center for 2D growth, blue and dark atoms, respectively.

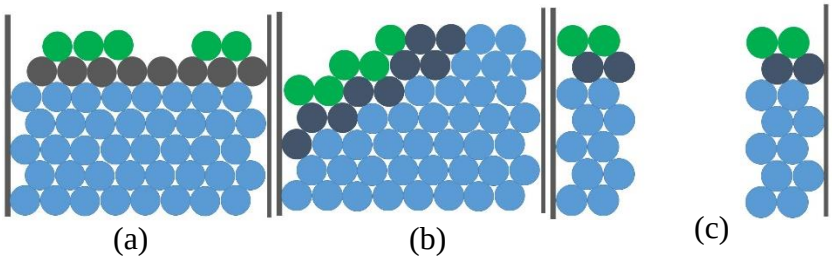

Figure 3.3. Various 2D Growth Modes. (a) Applied Potential Higher than Critical Potential; (b) and (c) Applied Potential lower than Critical Potential [82]

Variation of the applied potential can transform the electrodeposition process from kinetics to thermodynamics. Applied potential if higher than critical potential can lead to crystal growth as in 2D growth mode and is shown in Figure 3.3(a). Thermodynamics controlled plane ((002) plane for Co) can grow perpendicular to template pores at the initial stage of electrodeposition to form continuous nanowires.

If the potential is decreased effect of thermodynamics is decreased as well, while the kinetics is heightened. These two factors can contribute together at some potential range which leads to the growth of nanowires via both 2D plane mode and 2D tilted plane mode yielding solid nanowires as shown in figure 3.3(b). However, if the applied potential is lower than the critical potential, kinetics become the dominating factor for

electrodeposition, and 2D tilted growth plane mode persists only. As a result, initially formed kinetics governed plane ((110) plane for Co) cannot develop completely perpendicular to the pore walls and gives tubular nanostructure (figure 3.3c).

Thermodynamics and kinetics controlled growth process can be explained by Bravais law. In a thermodynamics controlled deposition condition, any foreign atom has superior rank among other crystallographic planes, as in this condition the lattice spacing as well as interplanar spacing of these crystal planes are smaller than that of kinetics modulated crystallographic planes. Besides, the attractive force between thermodynamic crystal planes and foreign atoms is stronger than the attraction between kinetics crystallographic planes and foreign atoms. As a result, thermodynamics controlled crystal plane (200) for example, is formed. On the other hand, in kinetics conditions, energy of foreign atoms is high enough to overcome the coulomb attraction, and kinetics controlled crystallographic plane (110) is grown. The process is shown in figure 3.4 where blue, green, and yellow particles represent ions, adatoms, and stable atoms, respectively, and black arrows represent ion diffusion from the electrolyte to pores which are a kinetics growth process, and blue arrows represent surface diffusion of adatoms to energetically favorable position which is a thermodynamic process. Only bath temperature can affect the rate of this growth process as all the aspects involved in electrodeposition i.e. migration, bulk diffusion or surface diffusion, etc. are controlled by diffusion coefficient as explained by the Arrhenius equation. Temperature can induce morphological changes in grown nanowires by controlling the rate of growth processes (thermodynamics and kinetics).

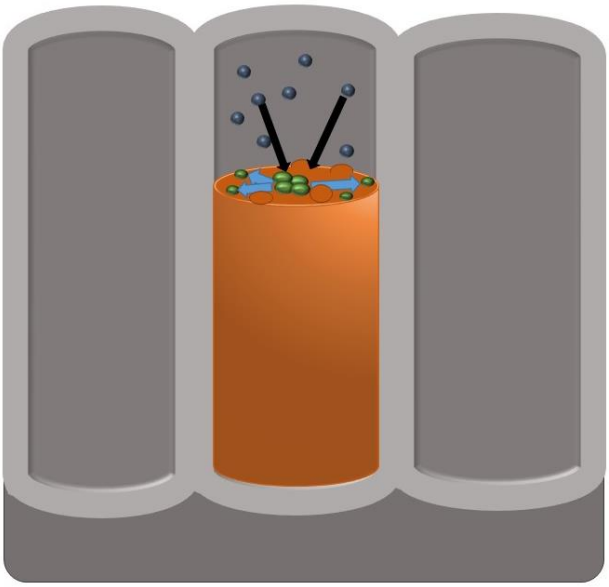

Figure 3.4. Growth of Nanowire Following Bravais Law [83]

Generally, high temperature favors the diffusion of adatoms which helps to continue the growth of preexisting nuclei and grains. As a result, coarse crystallites with rough surface morphology is found[83]. On the other hand, at low temperatures, the growth of preexisting grain is suppressed which allows new nuclei to form simultaneously, thus yielding in finer grains and comparatively smoother surface morphology.

Tian proposed 2D like nucleation mechanism for single-crystalline metallic nanowires with low melting point i.e. Cu, Ag, and Au[5]. Growth of nanowires will take place if the size of the initially grown nucleus exceeds the critical cluster size N_c, which can be represented as (equation 3.5)

$$N_c = \frac{bs\Psi^2}{(ze\varphi)^2} \tag{3.5}$$

However, for 3D growth, the relation becomes as equation 3.6

$$N_c = \frac{8\,BV_m^2\sigma^3}{27\,(ze|\varphi|)^3} \tag{3.6}$$

where, s/V_m is area/volume of one depositing metal atom on nucleus surface, Ψ/σ is edge/surface energy, φ is overpotential, z is effective electron number, b/B is constant[5].

Cao and coworkers [42] have also discussed the growth mechanism of metal nanowires and nanotubes inside template pores. In the electrodeposition process, metal ions surrounded by a hydration layer move toward the cathode and then are reduced mainly in three steps.

1. Metal ion hydration number decreases, and the metal ions are rearranged in solution near cathode surface

$$M^{2+} . m\ H_2O \rightarrow M^{2+} .(m\text{-}n)\ H_2O\ (m>n) + nH_2O \tag{3.7}$$

2. Metal ions surrounded with partly discarding water molecules are reduced in a step by step manner.

$$M^{2+} . (m\text{-}n)\ H_2O + e^- \leftrightarrow M^{+} . (m - n)\ H_2O$$

$$M^{2+} . (m\text{-}n)\ H_2O + e^- \leftrightarrow M^{+} . (m\text{-}n)\ H_2O\ (adsorption) \tag{3.8}$$

3. Adsorbed atoms discard surplus hydration layer entering the crystal lattice

$$M.\ (m\text{-}n)\ H_2O\ (adsorption) \leftrightarrow M\ (crystal\ Lattice) + (m - n)\ H_2O \tag{3.9}$$

When an electric field is applied, metal ions move toward cathode where it is deposited inside the pores of the template. The rate of movement of a metal ion in the presence of an external electric field E can be expressed by following equations.

$$\gamma_+ = U_+ . dE/dl \quad (3.10)$$

$$\gamma_- = U_- . dE/dl \quad (3.11)$$

Here γ_+ is ion movement rate (ms^{-1}), U_+ represents metal ion mobility ($m^2s^{-1}V^{-1}$), U_- and γ_- are negative ion mobility and movement rate, respectively and dE/dl is the potential gradient (Vm^{-1}). Two types of growth rates are possible for the deposition of either nanotubes or nanowires i.e. V_{II} (growth rate parallel to the current direction) and $V_\perp$ (growth rate perpendicular to the current direction) as shown in figure 3.5. The junction between the bottom of the template and the cathode surface acts as a suitable site for starting the deposition of metal ions. As a result, this area works as a nucleation site. Additionally, the high surface area of the template pore wall also acts as an energetically favorable site for growth yielding in tubular structure.

In the case of applied low current density, the influence on both V_{II} and $V_\perp$ is minimal resulting in similar values for both of them ($V_{II} \approx V_\perp$). As a result, with the increase of deposition time, metal atoms fill the template pores yielding in 1-D nanowire. When the higher current density is applied, dE/dl value gets bigger and a growth direction parallel to the current direction is preferential ($V_{II} >> V_\perp$).

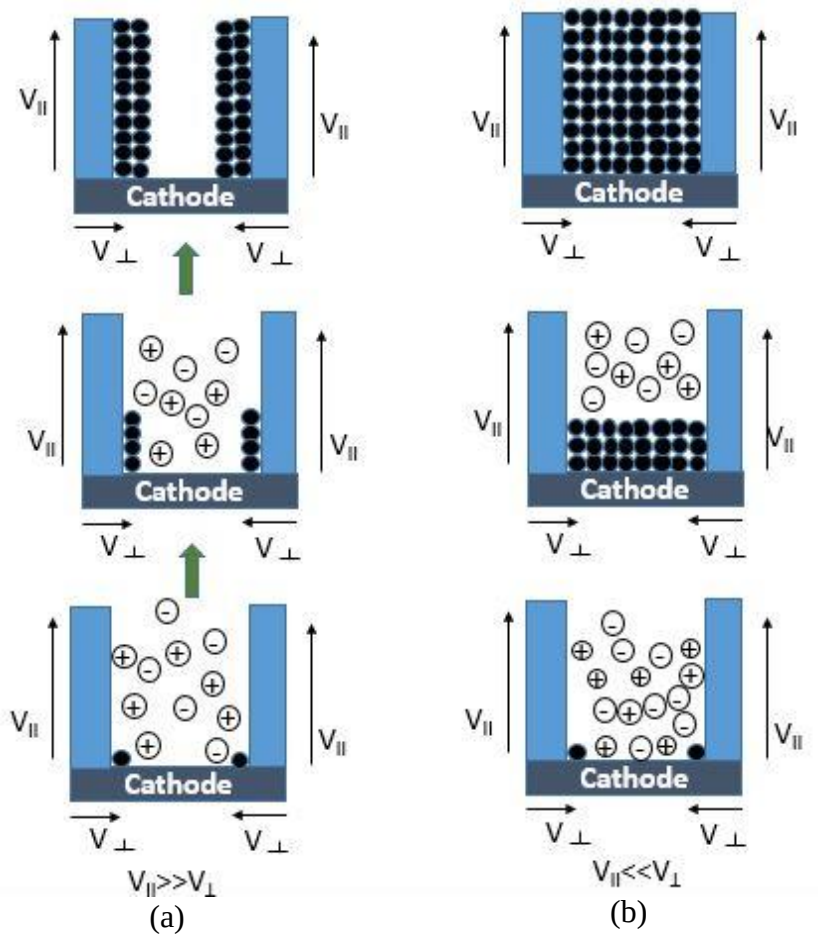

Figure 3.5. Schematic of the Growth Process of 1D Nanostructures; (a) Metal Nanotube Growth, (b) Metal Nanowire Growth Steps [42]

In this case, metal atoms start to deposit on the pore wall first, and with continuous electrodeposition gives a tubular nanostructure. However, researchers have also argued that not only applied potential but also other factors like application of anchoring agent, additional processing of template before deposition, etc. can also play a role in synthesizing tubular nanostructures. That is why it possible to synthesize both solid nanowires and hollow nanotubes using template assisted electrodeposition method.

3.5 Methodology

3.5.1 XRD Sample Preparation

XRD was performed by using Rigaku mini flex powder diffractometer to analyze the crystal structure and preferred planes of synthesized Cobalt nanowires. Nanowires were washed several times along with ultra-sonication and magnetic decantation using methanol to make sure that there is no alumina membrane or byproducts of alumina and NaOH reaction are present in the samples. Free cobalt nanowires were then dispersed on a microscopic glass slide and kept some time for drying. The sample then was transferred into an XRD capillary tube. The nanowires were loaded carefully in such a way so that there is maximum packing in the tube. To avoid excessive loss of X-ray because of the absorption of the glass tube, a low absorption glass tube (glass number 50) were used (purchased from Hampton Research) throughout the experiments.

3.5.2 HRTEM Sample Preparation

Focused Ion beam (FIB) was used to prepare HRTEM sample. The samples were prepared in FEI Quanta 3D FEG dual beam SEM/FIB instrument with acceleration voltage of 0.5-30 kV from Analytical Instrument Facility (NCSU). The samples were prepared via FIB lift-out technique. Talos F200X with acceleration voltage of maximum 200 kV was used for TEM/HRTEM analysis, and Gatan Digital Micrograph software was used to analyze acquired results.

3.6 Results and Discussions

3.6.1 XRD Analysis

Figure 3.6 presents the XRD spectra of as-grown Co nanowire deposited at 25 ^{0}C bath temperature for (a) 3 mA.cm^{-2}, (b) 5 mA.cm^{-2}, and (c) 7 mA.cm^{-2}. From the figure, we can see that, there are multiple diffraction peaks at 41.52±0.2^0, 44.3±0.3^0, 47.28±0.28^0, 75.62±0.18^0 and 92.27±0.23^0 which represent (100), (002), (101), (110) and (112) planes respectively according to PDF card 05-0727.

These results show polycrystalline nature of the nanowire samples with (002) plane as the most intense among others in all the cases which is the preferential direction and was also reported by Xu et al.[84]. Further, we can also see that at lower current densities (3 mA.cm^{-2} and 5 mA.cm^{-2}) there is little change in peak intensity as they are superimposed on each other.

However, in the case of high current density (7 mA.cm^{-2}) we can see a significant increase in peak intensity for all the planes. The maximum increase in peak intensity is found for (002) plane. It means that the nanowires show strong preferential orientation at high current density.

From the XRD data we can also calculate the d-spacing of the nanowire samples. For better comparison, our calculated values were compared with values reported in the literature. We can see that the accepted reported values and calculated values match perfectly for all the planes.

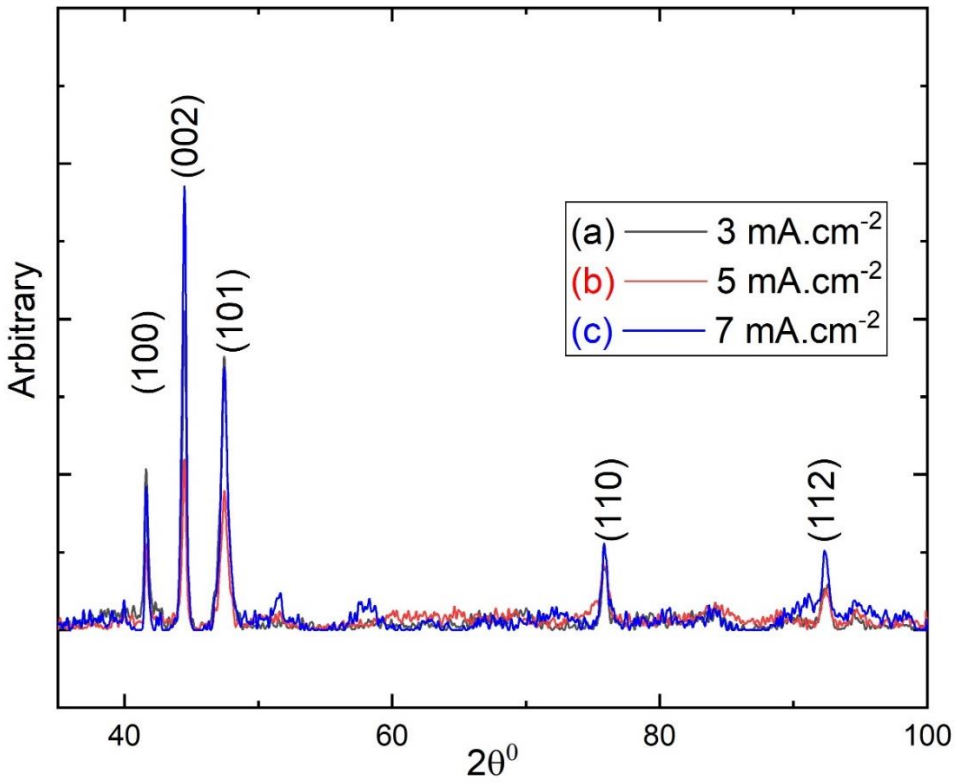

Figure 3.6. XRD Spectra of Co Nanowire Deposited at RT (25 ^{0}C); (a) 3 mA.cm^{-2}, (b) 5 mA.cm^{-2} and (c) 7 mA.cm^{-2}

Accepted value for d-spacing from the literature[85] for different planes are listed in table 3.1.

Table 3.1. d-spacing Value for Co from Literature

Planes	**(100)**	**(002)**	**(101)**	**(110)**	**(112)**
d-spacing(A^0)	2.1715	2.035	1.9158	1.2537	1.0655

From this figure using the value of 2-theta degree, d-spacing was calculated according to Bragg's Law as stated in equation 3.1 and the results are compiled in Table 3.2. Full width half maximum (FWHM) value was calculated using OriginLab software.

Table 3.2. d-spacing Calculation for Co Nanowire Deposited at RT and Different Current Density

Operating Conditions / Crystal Plane	25 ^{0}C, 3mA.cm^{-2}		25 ^{0}C, 5mA.cm^{-2}		25 ^{0}C, 7mA.cm^{-2}	
	2 θ (deg)	d (A^0)	2 θ (deg)	d (A^0)	2 θ (deg)	d (A^0)
(100)	41.64941	2.16563	41.64942	2.16563	41.58799	2.16869
(002)	44.45443	2.03528	44.49538	2.03350	44.47490	2.03439
(101)	47.42328	1.91455	47.44371	1.91377	47.44371	1.91377
(110)	75.78047	1.25363	75.80094	1.25334	75.86236	1.25248
(112)	92.65148	1.06449	92.46722	1.06613	92.50816	1.06577

Figure 3.7 shows the XRD spectrum of Co nanowire deposited at 40 ^{0}C bath temperature at current densities (a) 3 mA.cm^{-2}, (b) 5 mA.cm^{-2}, and (c) 7 mA.cm^{-2}. We can see the same crystal planes at the same diffraction angles as the previous case. However, (101) plane shows the highest peak intensity, indicating that preferential orientation has been changed from (002) plane (RT deposition).

At the same time, with the increase in current density, the peak intensity increases in all cases similar to the room temperature deposition. Maximum increase in peak intensity was found for 7 mA.cm^{-2} deposition current density for (101) plane.

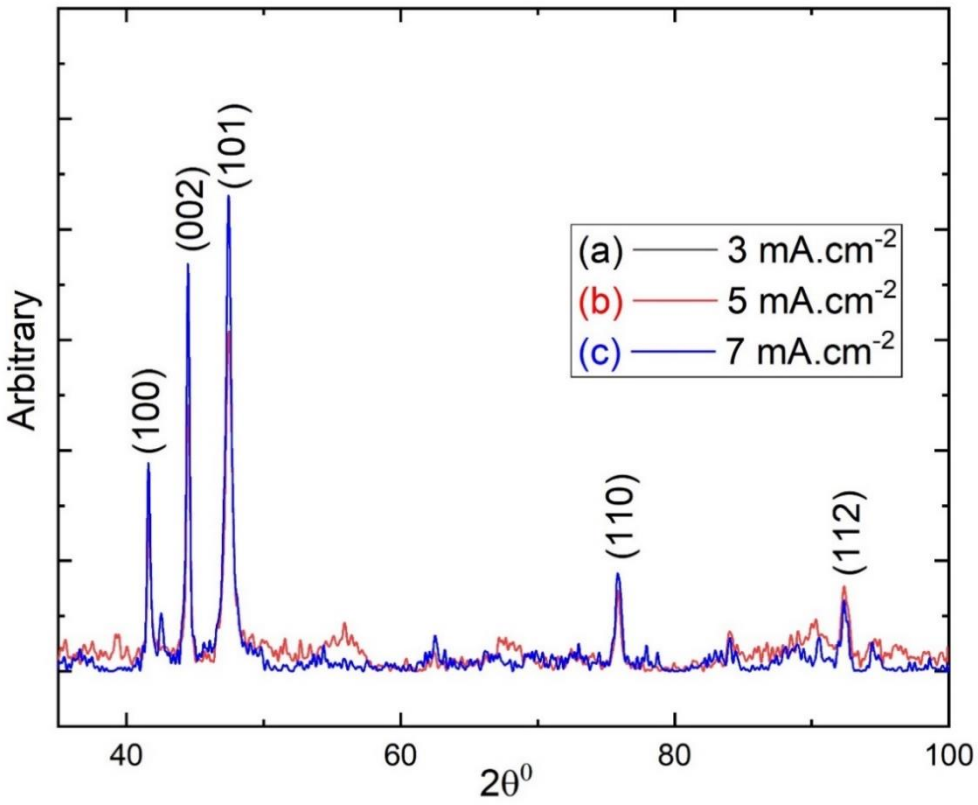

Figure 3.7. XRD Spectra of Co Nanowire Deposited at 40 ^{0}C; (a) 3 mA.cm^{-2}, (b) 5 mA.cm^{-2} and (c) 7 mA.cm^{-2}

The increase in peak intensity is more prominent for (100), (002) and (101) planes compared to (110) and (112) planes. From this figure using the value of 2-theta degree, d-spacing values were calculated for all current densities and the results are compiled in Table 3.3. We can see that the calculated d-spacing values are fairly comparable to the values reported in the literature.

Table 3.3. d-spacing Calculation for Co Nanowire Deposited at 40 ^{0}C and Different Current Density

Operating Conditions / Crystal Plane	40 ^{0}C, 3mA.cm^{-2}		40 ^{0}C, 5mA.cm^{-2}		40 ^{0}C, 7mA.cm^{-2}	
	2 θ (deg)	d (A^0)	2 θ (deg)	d (A^0)	2 θ (deg)	d (A^0)
(100)	41.54704	2.17073	41.58799	2.16869	41.59124	2.16853
(002)	44.47490	2.03439	44.47490	2.03439	44.47490	2.03439
(101)	47.50513	1.91144	47.42323	1.91455	47.42323	1.91455
(110)	75.84189	1.25276	75.96474	1.25104	75.82142	1.25305
(112)	92.46721	1.06613	92.42626	1.06649	92.34400	1.06723

Figure 3.8 presents the XRD spectra of Co Nanowire deposited at 50 ^{0}C and at current densities (a) 3 mA.cm^{-2}, (b) 5 mA.cm^{-2}, and (c) 7 mA.cm^{-2}. We can see at this temperature two new planes have been detected i.e. (102) and (103) which were not found in low-temperature conditions. This might happen as high bath temperatures can aid in the formation of new planes. We can also see that, (101) plane shows the highest peak intensity indicating the preferential orientation of nanowires similar to the nanowires deposited at 40 ^{0}C. However, the ratio of the peak intensity of (101) plane over (002) plane is lower in this case compared to the nanowires deposited at 40 ^{0}C.

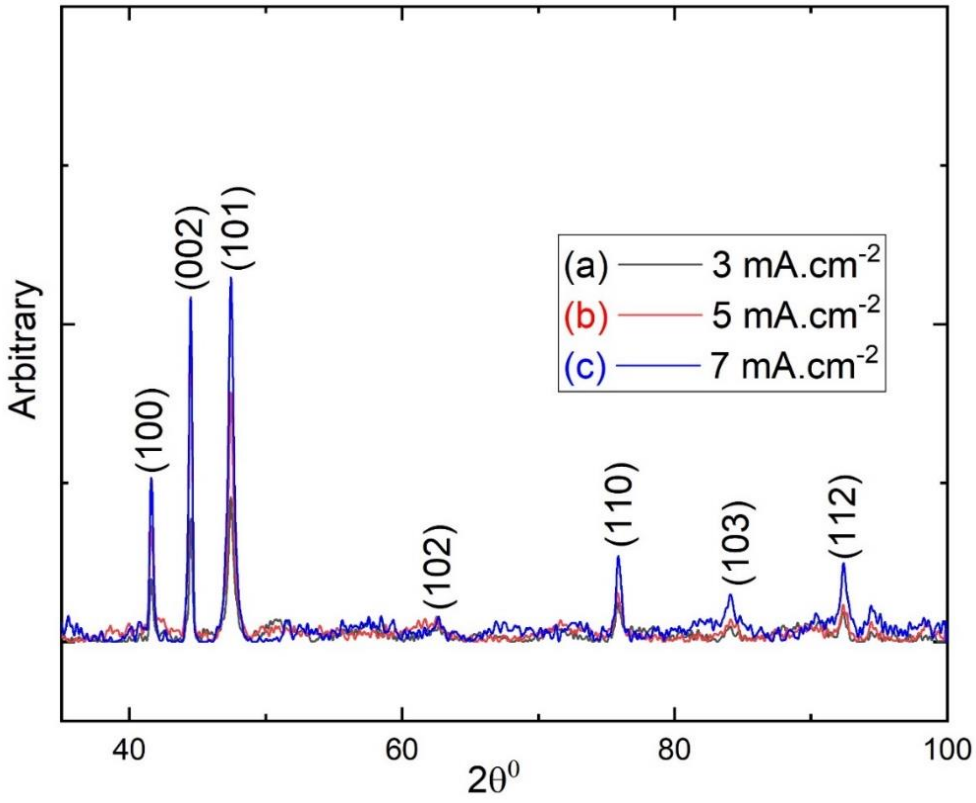

Figure 3.8. XRD Spectra of Co Nanowire Deposited at 50 ^{0}C; (a) 3 mA.cm^{-2}, (b) 5 mA.cm^{-2} and (c) 7 mA.cm^{-2}

At the same time peak intensity increases with an increase in current density. However, we can also see a significant increase in the peak intensity for (110) and (112) planes, which were not the case for low-temperature conditions. From this figure using the value of 2-theta degree, atom spacing was calculated and the results are compiled in Table 3.4. We can see that the calculated d-spacing values are fairly comparable to the values reported in the literature.

Table 3.4. d-spacing Calculation for Co Nanowire Deposited at 50 ^{0}C and Different Current Density

Operating Conditions / Crystal Plane	50 ^{0}C, 3mA.cm^{-2}		50 ^{0}C, 5mA.cm^{-2}		50 ^{0}C, 7mA.cm^{-2}	
	2 θ (deg)	d (A^0)	2 θ (deg)	d (A^0)	2 θ (deg)	d (A^0)
(100)	41.58799	2.16853	41.56752	2.16971	41.11708	2.16243
(002)	44.47490	2.03439	44.45443	2.03528	44.47490	2.03439
(101)	47.42323	1.91455	47.40276	1.91533	47.48466	1.91222
(110)	75.75999	1.25391	75.84189	1.25276	75.84189	1.25276
(112)	92.18382	1.06866	92.38531	1.06686	92.36484	1.06704

In summary, deposition bath temperature can affect the preferential crystallographic orientation. If we compare the peaks at a certain temperature for different current densities, we can see in all the cases that, with an increase in current density from 3 mA.cm^{-2} to 7 mA.cm^{-2} the peak intensity of different crystallographic orientations increases though the preferential orientation of crystal planes does not change. The increase in intensity is more prominent for (100), (002) and (101) planes compared to (110) and (112). However, with the increase in bath temperature, we found the preferential orientation has been changed. From these results, we can infer that the bath temperature has more effect on crystal orientation than depositing current density. In addition, a new peak at 83.79^0 was found which corresponds to (103) plane and only evident at high temperature.

3.6.2 Average Crystal Size Calculation

Obtained XRD spectra were used to analyze the average crystal size for these processing parameters by using Bragg's law and Scherrer equation. Origin Lab software was used to calculate the full-width half maximum (FWHM) value for each peak. The detailed calculation for (100) plane at different processing conditions is presented in Table 3.5. Similarly, we can calculate the average crystal size for all process parameters is represented in figure 3.9.

Table 3.5. Detailed Calculation of Crystal Size for (100) Plane at Different Process Parameters

Current Density ($mA.cm^{-2}$)	**Temperature (^0C)**	**2θ (deg)**	**θ (rad)**	**FWHM (rad)**	**λ (nm)**	**K**	**Crystal Size(nm)**
3	25	41.649	0.363	0.307	0.154	0.9	27.67
	40	41.547	0.3626	0.233	0.154	0.9	36.44
	50	41.588	0.3629	0.216	0.154	0.9	39.32
5	25	41.649	0.363	0.210	0.154	0.9	40.45
	40	41.588	0.3629	0.2173	0.154	0.9	39.08
	50	41.567	0.3627	0.2540	0.154	0.9	33.44
7	25	41.588	0.363	0.240	0.154	0.9	35.39
	40	41.591	0.363	0.2390	0.154	0.9	35.54
	50	41.517	0.3588	0.2600	0.154	0.9	32.65

Figure 3.9 shows the average crystal size with varying bath temperatures and current densities for different planes. From the figure, we can see that both current density and temperature affect the crystallite size. However, bath temperature affects the crystal size more than current density, as electrodeposition is a diffusion-controlled process that is mostly affected by temperature thus by ion mobility. For simplicity, we considered only (002) and (101) planes as those are the dominant planes for different conditions.

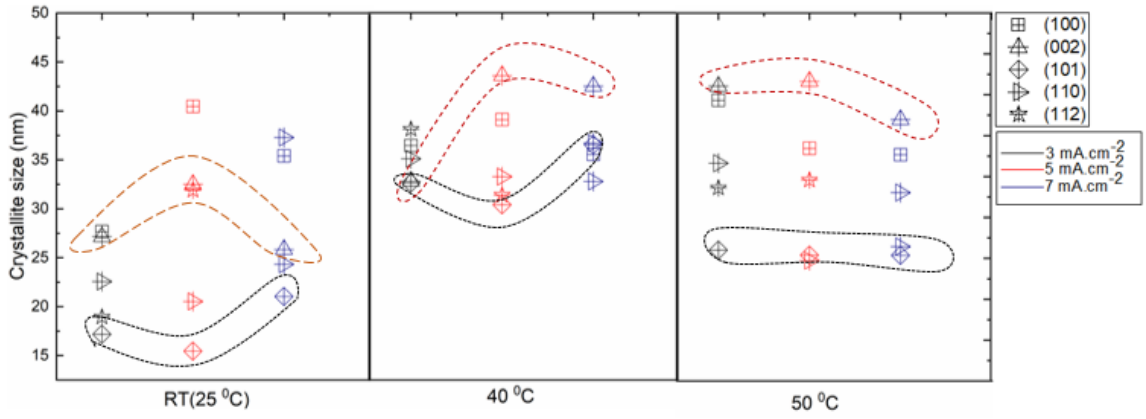

Figure 3.9. Effect of Processing Conditions on Crystal Size

We can see that (002) plane consists of higher size crystals in most of the cases whereas the crystalline size of (101) planes is smaller. This can be explained by the growth kinetics of these planes. For thermodynamic (002) planes the crystals grow continuously after nucleation which in turn increases the crystal sizes. On the other hand, for kinetic controlled (101) planes the crystal size cannot increase significantly as more cations come to suitable nucleation sites which in turn suppresses further growth of formed crystals. We also found that the crystallite size of different planes increases

initially if the bath temperature is increased to 40^0C. However, at higher temperatures, crystallite size decreases.

3.6.3 TEM Analysis

For further investigation of crystal orientation HRTEM analysis was done. Because of the size of the nanowires (200 nm diameter and 10-15 micron long), the as prepared nanowires are not suitable for TEM/HRTEM analysis. That is why, sample was specially prepared as mentioned in methodology. The length of the final nanowire sample was 4-5μm. From Figure 3.10 inset, we can see the polycrystalline nature of electrodeposited Co nanowire at the bottom of nanowire as SAED pattern shows polycentric concentric ring which is an indicator of polycrystallinity. We can see that, the strong bright ring corresponds to (100) plane while a weaker white ring of (110) plane was also identified.

This characteristic is logical as these are the suitable nucleation sites which are near to the amorphous Al layer (deposited initially prior to the electrodeposition process to provide a conductive layer to the templates) and makes the regions near to the bottom of the nanowires polycrystalline in nature. This phenomenon has been reported by other researchers also. As for example, Huang et al. [86] reported similar polycrystalline nature of electrodeposited Sb nanowire.

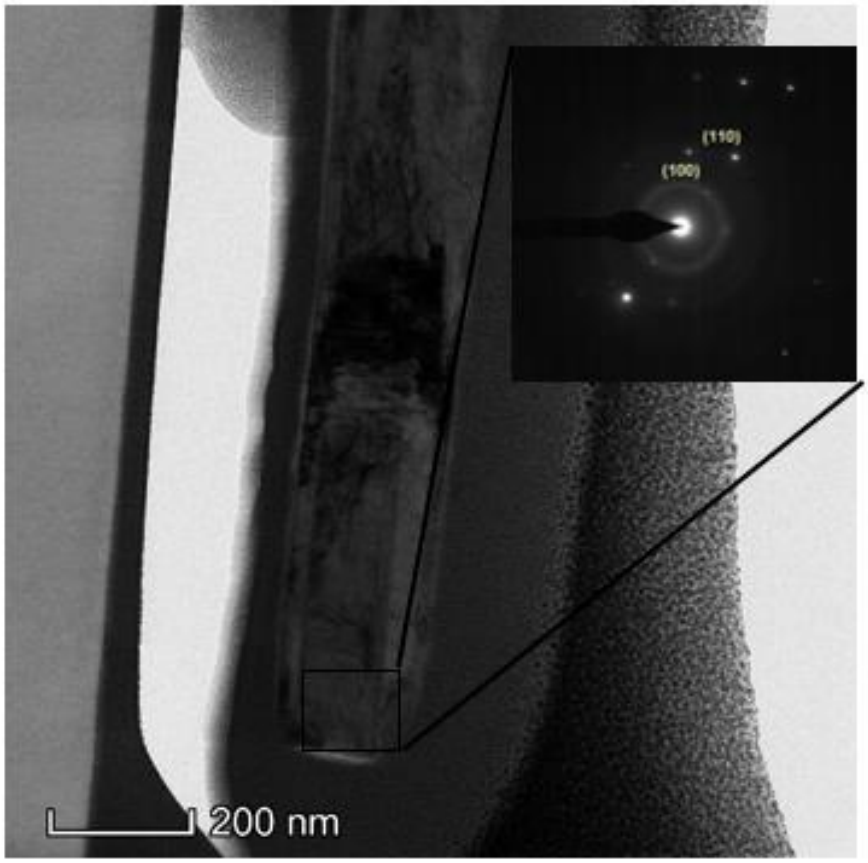

Figure 3.10. SAED Pattern of Nanowire Bottom Showing Polycrystalline Nature

Away from the bottom, nanowires start to show single-crystalline nature as shown in the SAED pattern from Figure 3.11. Crystal planes are also identified and shown in figure 3.11 inset. We can see the dominant crystal plane is (101) and is perpendicular to the wire axis [001] which is a resultant of nucleation competition among many planes. Besides, (002), (100) and (110) planes can also be identified. The presence of orderly arranged bright spots and clear lattice fringes indicate the presence of single-crystal zones in the synthesized nanowire.

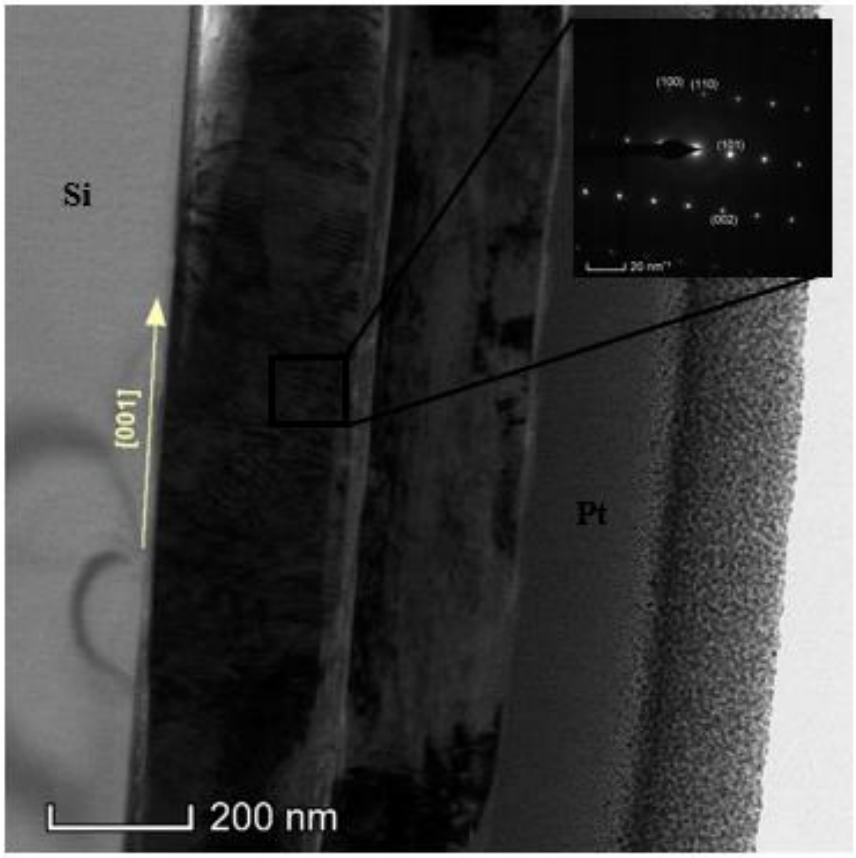

Figure 3.11. TEM Image of [001] Co Nanowire Deposited at 7mA.cm^{-2} and 40 ^{0}C. Inset is showing the SAED Pattern which Confirms the Single-crystalline Nature of Co Nanowire

We also found similar single crystalline regions over the whole length of the nanowire (4-5 μm) only with the change in preferential crystal orientation except the bottom region where only polycentric ring was identified.

We can conclude that the nanowires have zones of long single crystalline trunk with polycrystalline roots and using this FIB aided approach it is possible to identify the individual single crystalline regions. Additionally, the length of this polycrystalline base

can be found which can help to understand the interface of polycrystalline and single crystalline regions.

3.6.4 Proposed Growth Mechanism

The crystal orientation is governed by the growth mechanism which needs to be understood clearly to explain this phenomenon. Figure 3.12 (a) shows the far view SEM image of electrodeposited nanowire after 10 minutes. A special tilted sample holder was used for imaging to show the cross sectional view of alumina template.

The image shows that the nucleation starts at the bottom of the alumina template (juction between the bottom of the pores and deposited aluminum film) as a partially grown nanowire forest is seen (encircled bright region). However, all the nanochannels are not energetically suitable for nucleation to start. Some nanopore junctions act as nucleation sites and aid the nanowire growth while some other nanopores are not suitbale for nucleation initially and are found to be empty as seen in figure 3.12(b). We can also see the rooted nature of these nanowires which comes from the alumina templates. Even for pores filled with cobalt nanowire, we can see the length of these nanowires is not uniform which might indicate that the delayed start of nucleation in some of the nanopores.

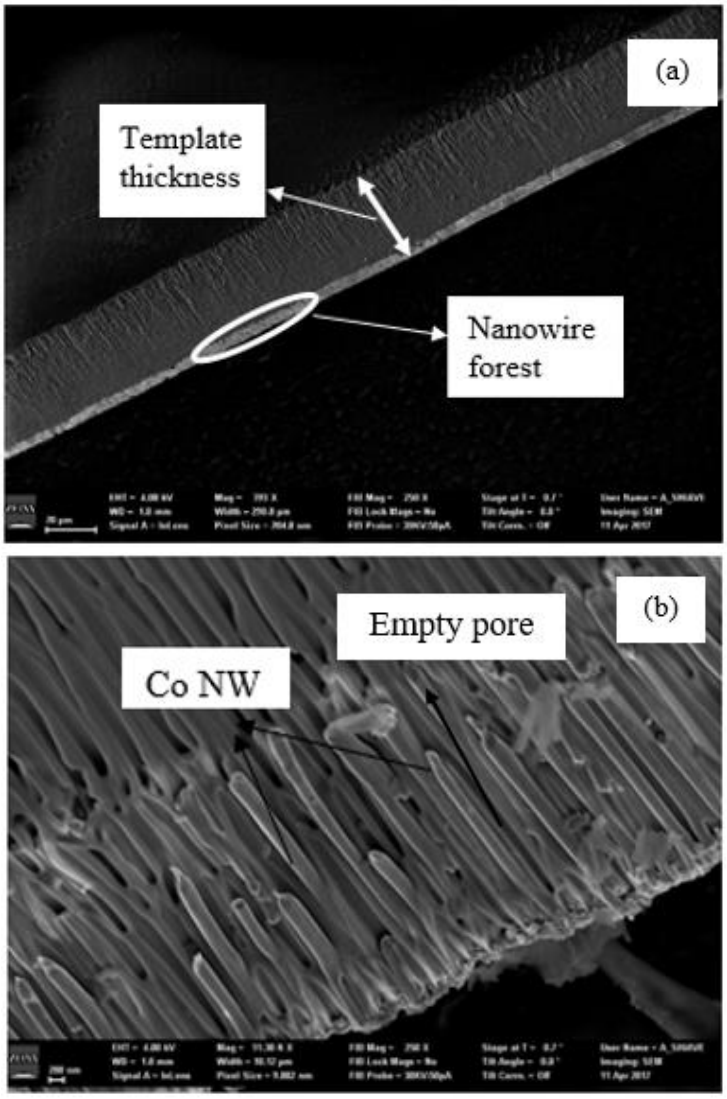

Figure 3.12. (a) Far View of Electrodeposited Co Nanowire after 10 minutes of Deposition; (b) Partially Grown Nanowires with Some Empty Channels

The growth mechanism can be explained using HRTEM images from thermodynamics and kinetics point of view. The crystal growth rate is determined by the 2D nucleation rate.

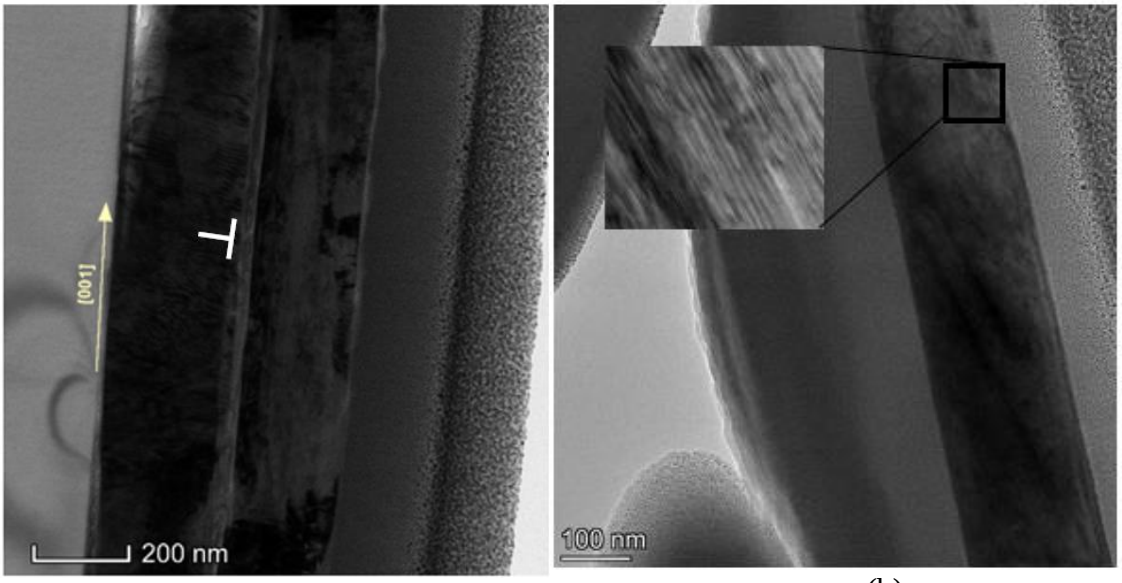

(a) (b)

Figure 3.13. Growth Mode of Co Nanowire Away from the Nanowire Bottom; (a) Perpendicular Growth Mode, (b) Tilted Growth Mode

The thermodynamics governed planes (002) are initially formed during electrodeposition and grow perpendicular to the wire axis as well as the pore wall as presented in figure 3.13(a). However, for nanowires deposited at 50 ^{0}C, we also found 2D tilted growth as shown in figure 3.13(b) which can be attributed to step growth mode[87]. The growth process is kinetic controlled rather than thermodynamics controlled as in layer-by-layer deposition process. In this process, the diffusing energy of reduced ions is small and can overcome Ehrlich-Schwoebel [88], [89] barrier. Based on our findings, we propose that electrodeposited cobalt nanowire mainly follow 2D nucleation mechanism with two types of possible growth modes i.e. perpendicular growth mode and tilted growth mode (step by step).

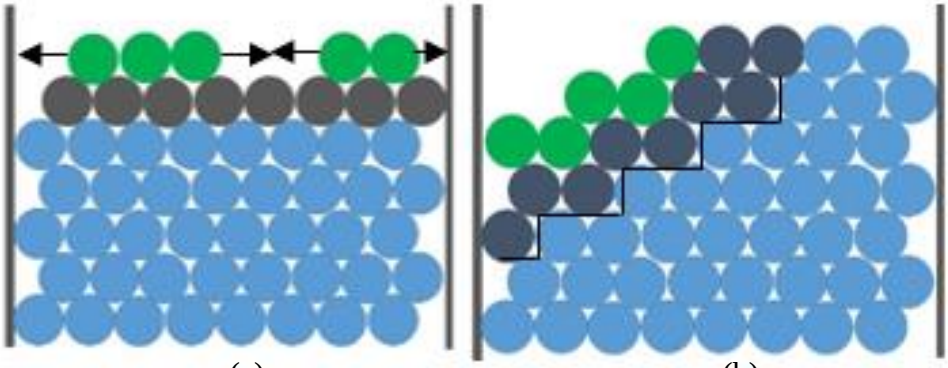

Figure 3.14. Proposed 2D Growth Modes for Co Nanowire; (a) Layer-by-layer Growth and (b) Tilted Plane Growth Mode

HRTEM images were also analyzed to calculate the d-spacing and match the findings of XRD results. Figure 3.15 shows the HRTEM image of Co nanowire synthesized at a current density of 7 $mA.cm^{-2}$ at 50 ^{0}C deposition bath temperature away from the nanowire bottom. From the lattice fringes and with the help of ImageJ software, we have calculated that the dominant crystal plane has a d-spacing of 0.190 nm which corresponds to (101) plane and is consistent with our XRD result as well as the theoretical reported values. However, (110) plane was also identified with a d-spacing of 0.125 nm. HRTEM images from other regions will reveal the identity of other planes also. Using this analysis approach, it is possible to calculate the d spacing for other dominant planes in all samples.

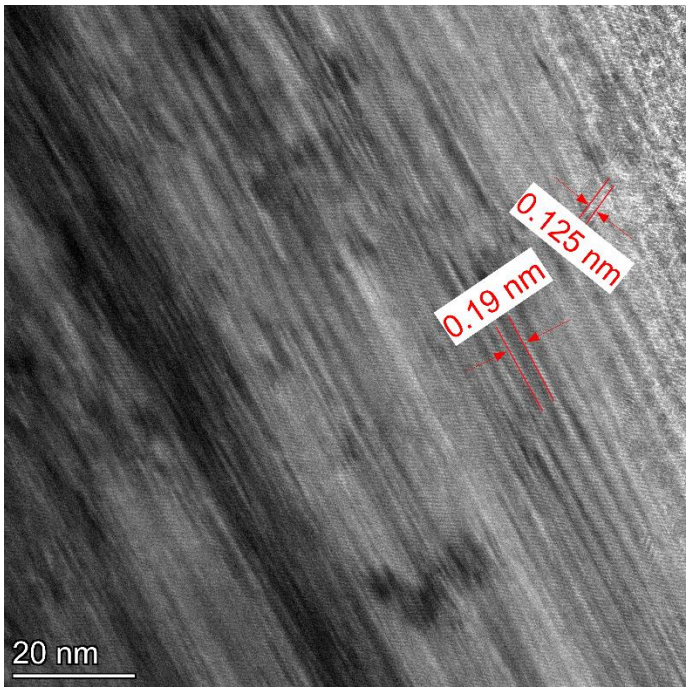

Figure 3.15. HRTEM Image is Showing d-spacing (0.191 nm) of Dominant (101) Plane. (110) Plane is also Identified with d-spacing of 0.125 nm

3.7 Conclusion

We have found that it is possible to identify single-crystalline Co nanowire via template-assisted electrodeposition approach at low bath temperature using FIB. XRD results show the nanowires consist of many crystal planes, and at high bath temperature, the introduction of a new plane is possible. We also found that crystal size is affected by both temperature and current density. However, the temperature has more effect on crystal size compared to current density as electrodeposition is a diffusion-controlled process. We found that at bath temperature of 40 ^{0}C the crystal size is the largest for most of the cases compared to other temperatures. For simplicity, only the (002) planes and

(101) planes were considered. However, we saw a similar trend for all other possible crystal planes.

HRTEM images and SAED patterns confirm that the nanowires have long single crystalline regions. It was also found that with FIB operation, it is possible to acquire and separate single-crystalline portion. From the results, we can see that nanowires have polycrystalline base followed by a long single-crystalline region. We have also elucidated that the nanowires follow a 2D type growth mechanism with either perpendicular, tilted, or combination of these growth modes. Finally, d spacing calculation using the lattice fringes from HRTEM image supports our findings from XRD analysis and confirms the dominant crystal plane.

FIB based technique can be adopted to acquire bulk amount of single-crystalline Co nanowire which can be used for further applications that need single crystalline nanowire regions. This presents a potential for a “Bottom-up” processing via TAE followed by a “Top-Down” formation from FIB. Nanowires possess the improved properties and uniqueness which make them a potential candidate for many applications i.e. electrical interconnect, data storage, MEMs devices, etc. In the following chapter, we will discuss a novel application of these nanowires in nanowire-based nanofluid which can improve the thermal properties of the base fluid and can increase the efficiency of heat transfer.

CHAPTER IV

APPLICATION OF 1-D METAL MODIFIED NANOFLUID FOR THERMAL PROPERTY ENHANCEMENT

4.1 Introduction

Metal nanowires, because of their electric, thermal, mechanical, and magnetic (for magnetic metals) superiority are potential candidates for numerous applications like electrical interconnect, MEMS Device, sensors, high-density data storage, biological applications, etc. Recently, researchers have used nanoparticles for the preparation of nanofluid which is a stable dispersion of nanoparticles in a base fluid, for efficient thermal transport, cutting fluid, enhanced oil recovery, etc. The most promising amongst these applications is the use of nanofluid as an efficient heat transfer media. Reports have shown that if nanoparticles can be incorporated in the base fluid, it can enhance the thermal property significantly.

With the advancement of technology and to meet the ever-growing demand, equipment must run efficiently with low power consumption. However, one of the main problems in this regard is the dissipation of heat as the operating temperature of any instruments from heavy machinery to computers must be kept low for high performance. Water, ethylene-based coolants, mineral oil, etc. are being used as heat transfer fluids in industries for years. A recent report has predicted that the heat transfer fluid market

would reach up to 4.56 billion USD by 2026[6]. Traditional coolants which are being used to keep machines cool cannot meet the desired requirement as thermal conductivity of them is very low. For example, at room temperature, the thermal conductivity of water is 0.613 kW/mK whereas for EG it is only 0.25 kW/mK. However, because of abundance and low cost, industries use these coolants in spite of their low efficiency which increases power consumption, and thus production cost.

Nanofluids can increase the efficiency of heat transfer and save energy also as low pumping power is needed for achieving the same level of outcome. For example, for a conventional cooling system, the pumping power should be increased by the factor of 12 if we want to increase the heat transfer by a factor of 2[90]. On the other hand, increasing the size of the cooling channel thus increasing the size of the apparatus is the only way to improve thermal efficiency which is not feasible in all the cases, especially when most of the devices and instruments are getting smaller every day. Nanofluids (NFs), for this reason, acquired great interest from the scientific community because of their unique and improved thermal properties i.e. conductivity, diffusivity, and heat transfer coefficient[91] compared to base fluids. Large surface to volume ratio of nanoparticles where a large number of surface atoms can take part in the heat transfer process is believed to be one of the main reasons. Besides, because of the much smaller size of nanoparticles, NFs show higher followability thus making them suitable for cooling electronic devices or automotive engines.

For efficient heat transfer applications, metals are primary candidates because of their high thermal conductivity. Researchers have tried to incorporate this improved

property in metal nanofluid and found promising results[92]–[95]. However, most of the works done so far are based on 0-D metallic nanoparticles. The study of metal nanowire-based nanofluid is still very limited and offers a potential area for future research. The main challenge for nanowire-based nanofluid comes from the stability as in most of the cases, nanowires are bigger in size than nanoparticles. That is why nanowires sediment faster than nanoparticle which could pose a big problem for nanofluid preparation. In this research, we have successfully prepared Co nanowire-based nanofluid with water as base fluid and studied the thermal property at different volume concentrations.

4.2 Background

James Clerk Maxwell in the 1870s first introduced the idea of solid suspension in a fluid to improve properties. Since then, it got attention from researchers all over the world. However, because of the big particle size and fast sedimentation, it was impossible to use these colloidal fluids in real-life applications. Sedimentation of solids can clog the fluid channels thus, in turn, increases the pumping power, decreases efficiency, and decreases the effectiveness of thermal transport. Nanoparticles, on the other hand, can overcome these issues because of their much smaller size though sedimentation is still a great scientific challenge.

Various research groups have found promising results using nanofluids. Masuda and coworkers first included various nanoparticles (TiO_2, Al_2O_3, and SiO_2) in base fluid and found improved heat transfer properties. After them, many research groups have found the enhanced thermal property of nanofluids compared to base fluids [96], [97].

Sundar et al.[98] found that the thermal conductivity of water increases by up to 6.52% and 24.6% if Al_2O_3 and CuO NPs of 0.8 vol% are added respectively. They argued the increase in surface area and Brownian motion of suspended solids are the main reasons for this increase. They also reported that the thermal conductivity increases 2-4 times with the increase of temperature from 30^0C to 60^0C. Sundararaj[99] and co-workers found an increase in the thermal conductivity of Kerosene up to 13.3% with less amount of alumina NP addition (0.05 vol%) at 55 ^{0}C. They have also investigated other thermophysical properties like viscosity, surface tension, etc. of Kerosene after adding NPs. Thermal conductivity of water-based alumina nanofluid increases to 21% at room temperature as reported by Moldoneanu et al.[15], which is higher than previous findings though they used higher volume fraction (1 vol%). All of them found thermal conductivity increases more if the concentration of added nanoparticles is higher.

Thermal conductivity of water-based CuO NFs increased from 10%-30% according to Zhu et al.[100] with increasing volume fraction. Karimi et al. studied the thermal conductivity of water-based magnetite (Fe_2O_3) and hematite (Fe_3O_4) nanofluid and found that the thermal conductivity ratio of these nanofluids with water increases from 15% to 38.5% for magnetite nanofluid and 13% to 175% for hematite nanofluid[101] at different particle volume fractions. However, Shima et al.[102] showed that though thermal conductivity of Fe_2O_3 NF (both aqueous and non-aqueous) increases with temperature, the thermal conductivity ratio compared to the base fluids at these temperatures remain constant. They also found similar results for viscosity value. They concluded that thermal conductivity and viscosity track the values of the base fluids with

increasing temperature irrespective of their nature. For example, Yoo et al.[103] found that the thermal conductivity of DI water increases by 14.4% for 1 vol% TiO_2 nanofluid whereas for Al_2O_3 and WO_3 nanofluid can increase the conductivity values by 4% and 13.8% respectively. Later on, Sundar et al.[104] found that with the inclusion of Fe_3O_4 (2 vol%) nanoparticle in distilled water can increase the thermal conductivity by 46%. Other oxide-based nanofluids were also studied by different researchers[105]–[108]. To be efficient for thermal conductivity applications, prepared nanofluid should have two main characteristics; no sedimentation and no-agglomeration. Because of the size factor, the effect of gravity on nanoparticles is low which slows down the sedimentation. Homogenized dispersion without any agglomeration is still a challenge for nanofluid.

Apart from oxide nanofluids, researchers investigated pure metallic nanofluids also and some studies have shown that the thermal conductivity of metallic nanofluid is higher than non-metallic nanofluid (containing non-metallic and ceramic nanoparticles)[109]. Sinha et al.[16] studied thermal conductivity enhancement of ethylene glycol-based iron and copper nanofluid. They compared their results with commercially available iron and copper nanoparticle and found that the thermal conductivity of their copper nanofluid increases 25%-70% whereas for iron nanofluid it is 11%-33%. They have also shown that the efficiency of heat transfer for copper nanofluid is higher than iron nanofluid by using them in small scale heater-cooler-pump setup. Esfe and co-workers[17] have studied the effect of iron nanoparticle on thermal conductivity for Fe-water nanofluid. They have also investigated dynamic viscosity of Fe-water nanofluid at different nanoparticle volume fractions and found that viscosity increases

linearly if the NP volume fraction is increased. They found that the thermal conductivity increases from 5%-8% for various size nanoparticle where the maximum increase is found for the smallest size NPs. Chen et al.[110] reported the effect of Cu nanowires on pool boiling of saturated water and found that both critical heat flux and thermal conductance on nanowires increase when compared to plain surface. Zhang and co-workers recently showed that thermal conductivity of ethylene glycol is improved by 13.42% after adding 0.46 vol% Ag nanowires (prepared by poly-vinyl-pyrrolidone technique). They also found that the property is superior compared to nanofluid containing a similar volume of spherical silver nanoparticles. More metal and metal oxide nanofluid based works for improved thermal properties are compiled in table 4.1 and can be found elsewhere[111].

Table 4.1. Cited Work on Metal and Metal Oxide Nanofluid

Added NP	**Size of NP**	**Base fluid**	**Loading**	**Property improvement**	**Ref**
TiO_2	21 nm	Polyalkylene glycol	0.07-0.8 %vol	TC* 37.8 % at 0.8% vol	[112]
Al_2O_3 TiO_2 SiO_2	45 nm 25 nm 10 nm	Water	0.25-3 %vol	TC 15%(Al_2O_3) 9%(TiO_2) 4.5%(SiO_2)	[113]
Cu	10 nm	DI Water	0.25-1 %wt	48% critical heat flux	[114]
Ag	15 nm	DI water	0.25-1 %wt	TC 11.5 % at 1%wt	[115]
Al_2O_3/Ag	13 nm(Al_2O_3) 25 nm (Ag)	DI water	0.005-0.1 %vol with different ratio	TC 12 %	[116]

Ag	<100nm	Commercial Heat transfer fluid	0.05 %wt	TC 12% at 55 ^{0}C	[117]
Fe_2O_3	50-60 nm	DI water EG	0.005-0.02 %vol	TC 16% (H_2O) 7%(EG) at 0.02%vol	[118]
Au	16 nm	Toluene	0.003 %vol	Effective TC 2%	[119]
ND**-Co_3O_4	2-4 nm diamond	Water	0.05- 0.15 %wt	TC 14% at 0.15%wt	[120]
Co_3O_4	<50 nm	EG	0.009-0.05 %vol	TC 5.4% at 0.05%vol	[121]
ND-Ni	4-5 nm	DI water EG	3.03 %wt	TC 21% (DI Water) TC 13%(EG)	[122]
$NiFe_2O_4$	8 nm	Water	0-2%vol	TC 17.2% at 2%wt	[123]

*TC= Thermal Conductivity, **ND= Nanodiamond

4.3 Nanofluid Preparation Methods

Nanofluids are prepared by even dispersion of nanoparticles in base fluids in such a way that there is minimum aggregation of added particles to ensure stability and no chemical change of base fluids. Two main techniques of nanofluid preparation have been developed focusing on these key criteria namely one-step/single-step and two-step/double-step methods.

In one step method, the synthesis of nanoparticles and preparation of stable nanofluid is done concurrently. Direct evaporation method is one of the common methods developed by Akoh et al.[124] where nanofluids are prepared by the solidification of nanoparticles directly from a gaseous phase inside the base fluid. They

synthesized ferromagnetic metal nanoparticles (Fe, Co, and Ni) by vacuum evaporation technique on running oil substrate (VEROS). However, the main problem of this process is that the nanoparticles cannot be separated from the base fluid. Eastman and his coworkers[125] developed a modified VEROS technique where Cu vapor was condensed directly into nanoparticles by the contact of flowing low-pressure ethylene glycol. Zhu et al. prepared Cu nanofluids using microwave irradiation technique and ethylene glycol as base fluid. The main advantages of this method are minimum, or no handling and storage are required for nanoparticles which can minimize the possibility of oxidation, good nanofluid stability can be attained. However, high cost, suitability only for low vapor pressure fluids, incapability of large-scale production etc. are the main disadvantages of this process.

The two-step nanofluid preparation method, on the other hand, is the most popular as it can overcome the challenges posed by the single-step method. In this method, nanoparticles are synthesized separately in the first step followed by controlled dispersion in a suitable base fluid. One of the main advantages of this method is that nanoparticles of different shapes (nanowire, nanotube, nanofiber, etc.) and materials can be used to prepare nanofluids. Besides, the cost is lower as various nanoparticle synthesis techniques have been scaled up for mass production into the industrial level. In the second step, synthesized nanoparticles are dispersed in a base fluid to attain a stable system. However, the main problem of this process is that the degree of aggregation is higher, and particles can aggregate in both of these steps. However, various techniques have been developed to get stable dispersion i.e. surfactant addition, pH control,

Ultrasonication, etc. Researchers have prepared nanofluid of various nanoparticles and base fluids using this technique[126],[127]–[134].

4.4 Stability of Nanofluids

Nanoparticles suspended in a liquid medium tend to form aggregate and thus sedimentation occur which poses a huge challenge while making a stable nanofluid. The velocity of particle sedimentation can be defined by Stokes law (equation 4.1)

$$V = \frac{2R^2}{9\mu} (\rho_p - \rho_L) \cdot g \tag{4.1}$$

where V is sedimentation velocity, R is radius of spherical particle, μ is liquid viscosity and ρ_P, ρ_L are the densities of particle and liquid medium respectively, and g is the gravitational acceleration. According to this law, the following measures can be taken to minimize the sedimentation process of the suspended particles

(1) Reducing the particle size

(2) Increasing the base fluid viscosity

(3) Minimizing the density difference between base fluid and added particles

Increasing fluid viscosity or minimizing density difference is not always possible from the application viewpoint, whereas reducing particle size seems to be the most feasible way. However, the surface energy of smaller particles is high which increases the possibility of agglomeration which leads to sedimentation and is undesired. To overcome these problems, researchers have tried different physical and chemical approaches. In a

physical stabilization approach powerful external force (ultrasonication, probe sonication, magnetic stirring, etc.) is used to break up the NP clusters and make a stable suspension. Chemical approach includes the addition of suitable surfactants (SDS, CATAB, Triton-x, long-stranded RNA, etc.) to modify the nanoparticles in such a way that strong repulsive force is present among them thus hindering the agglomeration process.

Stabilization mechanism is classified into two main categories i.e. electrostatic stabilization, and steric stabilization.

(i) Electrostatic stabilization: Electrostatic stabilization is described by the Derjaguin, Landau, Verwey, and Overbeek (DLVO) theory[135] and is a kinetic stabilization method. The electrostatic interaction energy is mainly depended on the number of surrounding ions around a NP in a solution. An increase in ion numbers leads to an increase in energy and becomes positive if the number of surrounding ions is more than 9. If the approaching charge carriers are few in numbers, attraction energy is high and can be compared to chemisorption energy. In that case, the repulsive force exists between NPs having the same negative or positive surface charges[136]. The surface charge can be induced by the following approaches; (1) ion adsorption, (2) ion substitution, (3) physical adsorption of charged particles, (4) dissociation of charged species on the surface, and (5) depletion or accumulation of electrons on the surface. If two adsorbates with the same charge approach the metal spheres from opposite sides, the net dipole moment is zero which increases if the charges are opposite to each other. Overall, cations and anions create many image charges on the surface as shown in Figure 4.1.

However, in a real situation, cations and anions are of different chemical nature having different interaction energy with metal spheres. As a result, the metal spheres are mainly surrounded by either cations or anions with a shell consisting of counter ions creating a double layer. This double layer consists of inside Stern layer and outside diffusive Gouy layer[136], [137]. Electrical double layers from two adjacent particles overlap each other causing repulsion and stabilize NFs. That is why if aggregates are formed or two different types of materials having different electric potential and surface charges are present in the fluid, it is not possible to redisperse them.

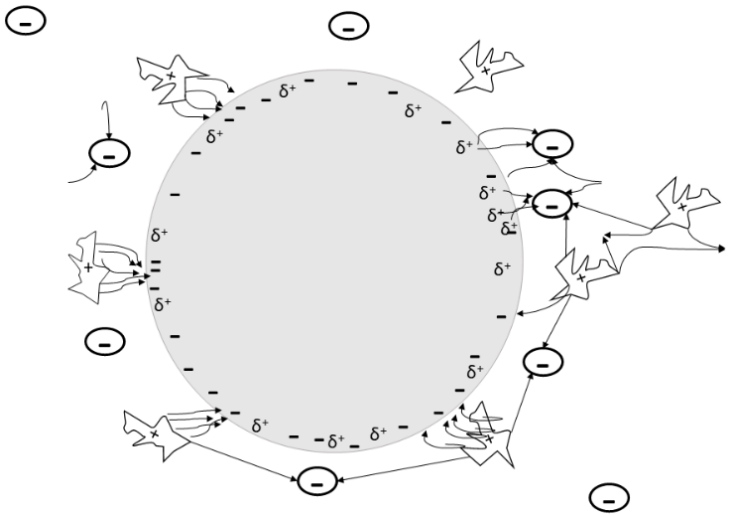

Figure 4.1. Representation of Metal Spheres Surrounded by Anions and Cations Creating a Distribution of Alternative Surface Charges[136]

(ii) Steric stabilization: Steric stabilization is another type of stabilization mechanism based on steric repulsion among molecules and adsorbed ions on adjacent particles which are governed by the nature and size of these molecules. Different forms of steric stabilization are illustrated in Figure 4.2. Large molecules having conical or elongated

geometry give effective stabilization because of geometric constraints around suspended NPs by keeping the approaching NPs apart from one another as shown in Figure 4.2(a).

Large molecules with strong adsorption ability are strong candidates for NP stabilization. If the length of the added stabilizer is longer (high molar weight polymers are generally used) than the characteristic size of suspended nanoparticles, solids can be encapsulated by a stabilizer molecule (Figure 4.2(b)). Chelating effect can improve the possibility of stabilizers being adsorbed on NPs if the stabilizer provides more than one adsorption center as shown in Figure 4.2(c).

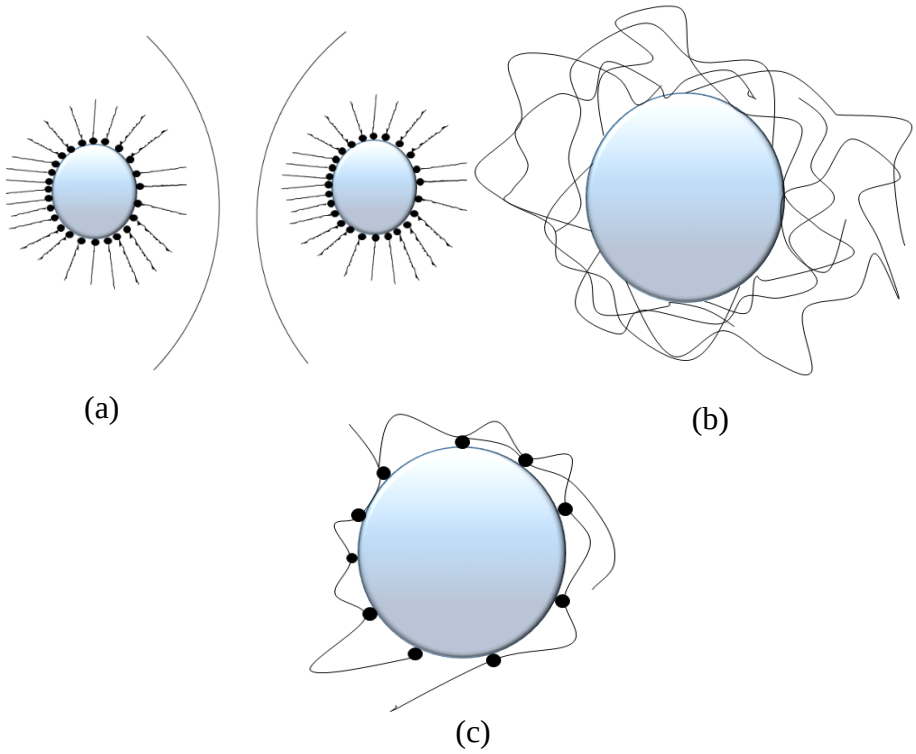

Figure 4.2. Steric Stabilization; (a) Elongated Molecules Adsorbed through Anchoring Centers Hindering other Molecules to Come Closer, (b) Long Polymer Chain to Encapsulate NP, (c) Chelate Effect, when a Stabilizer is Adsorbed through Multiple Anchoring Centers[136]

That is why it is important characteristics for the stabilizer to be adsorbed strongly on the NP surface providing longer residence time and thus preventing spontaneous desorption. Embedded NPs when coming closer to one another, the freedom of surface polymer chain and hence mixing entropy is reduced. At the same time, a long polymer chain between two embedded NPs results in an osmotic effect. Reduced entropy, as well as osmotic effect, are the two main key points of steric stabilization. Steric stabilization has some advantages over electrostatic stabilization i.e. (1) more applicability in different dispersion, (2) useful for high concentration NF, (3) possibility of dispersing different particles in the same fluid, (4) possibility of redispersion and (5) not electrolyte sensitive[136].

Though agglomeration free NF is the main criterion, some researchers have proposed that clustering and agglomeration is one of the main reasons for improved thermal conductivity of NFs. They argued that a certain degree of aggregation is necessary to improve the thermal properties[138], [139]. Evans et al.[138] reported that high aspect ratio fractal-like aggregates help to carry heat over a large distance. However, other researchers have contradicted this theory and found that aggregation of suspended NPs is the reason for reduced thermal property[140]. To make a stable NF, suspended NPs must meet the following principles:

1. Zeta potential principle (absolute value of zeta potential must be large to have strong repulsive force among particles)
2. Diffusion principle (particles are scattered by liquid medium and dispersed into the medium)

Based on these principles, researchers adopted three main stabilization techniques for nanofluid i.e. surfactant addition, pH control (Surface chemical effect), and Ultrasonication. These approaches are discussed next.

4.4.1 Surfactant/dispersant Addition

Adding surfactants or activators is one of the most popular methods for increasing nanofluid stability. Surfactants can modify the hydrophobic nature of nanoparticles surfaces into a hydrophilic one for aqueous nanofluid and vice versa for non-aqueous. Dispersants increase the wettability of suspended solids and may consist of a hydrophobic tail portion, usually a long-chain hydrocarbon, and a hydrophilic polar head group. Depending on the polar head group, dispersants can be categorized in 4 different groups i.e. (1) nonionic surfactants without a charged head group (polyethylene oxide, alcohol, and other polar groups), (2) anionic surfactants with negatively charged groups (long-chain fatty acid, sulfosuccinates, alkyl sulfate, phosphate, and sulfonate), (3) cationic surfactant with a positive head group (protonated long-chain amines) and (4) amphoteric surfactant with zwitterion head groups (charge depends on pH). The important issue is to select a suitable surfactant for a specific system. Generally, if the base fluid is a polar solvent, then the selected surfactants should be water-soluble. The solubility of nonionic surfactants can be found out by hydrophilic/lipophilic balance (HLB) value. If the HLB value is high, then surfactants are oil soluble and vice versa for water-soluble surfactants. There are some drawbacks also for surfactant addition as it

contaminates the liquid media, it may produce foams, and sometimes it can reduce the effective thermal conductivity of NF[111].

Because of the surface charge of suspended solids, zeta potential develops which in turn increases the repulsion force among them[141]. Figure 4.3 explains the zeta potential of a nanoparticle immersed in a fluid medium. Zeta potential is the difference of potential between the fluid medium and the stationary fluid layer attached to the particles which indicate the degree of repulsion between similarly charged adjacent particles.

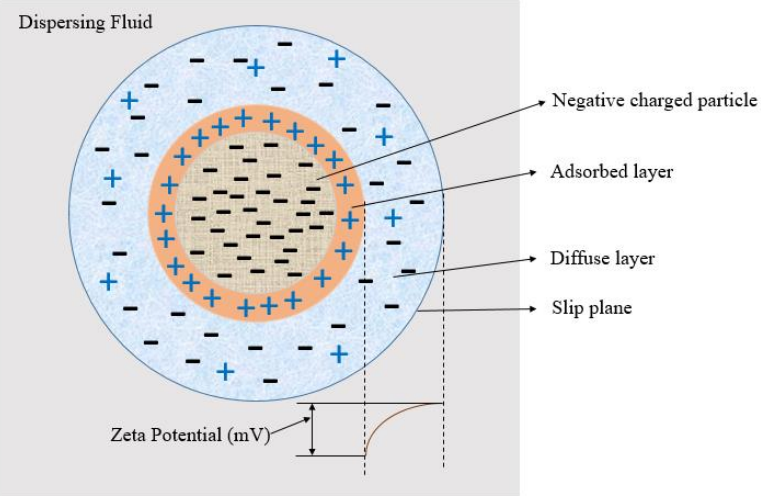

Figure 4.3. Zeta Potential of a Nanofluid

The liquid layer surrounding a nanoparticle consists of two parts i.e. adsorbed layer/ stern layer/ inner layer and diffuse layer/ outer region. In the stern layer, ions are tightly bound and in the diffuse layer, they are bound weakly creating an electrical double layer. The diffuse layer is important for stable fluid as with particle movement adjacent ions within its limit move along. The limit beyond which the ions do not move along with

particles is called a slip plane or surface of hydrodynamic shear. Researchers have argued that the higher the absolute value of zeta potential higher the electrical stability of nanofluid. Zeta potential with more than 30 mV (positive or negative) is considered to be stable nanofluid[142] while values more than 55 mV refer to excellent stabilization.

4.4.2 pH Control

NF stability is directly related to its electrokinetic properties as large surface charge of the NP creates strong repulsive force among them and make stable NF. Results have shown that CNTs attained good stability in water after simple acid treatment because of the hydrophobic to hydrophilic conversion due to OH group generated on the NP surface. Because of the size constraints of the NPs, large zeta potential far from isoelectric point (IEP) is needed for stability. IEP is defined as the concentration of surface charge where zeta potential is zero making the surface charge density equal to charge density which is the starting point of the diffuse layer. Changing pH will change the charge and move away from IEP making the NF stable[143].

Particles interact freely in a suspension either through attraction or repulsion which depends on the intraparticle distance and the sum of electrostatic repulsion, E_{el} and van der Waals attraction E_A namely total interface energy E_{tot}. E_{el} between two charged particles can be expressed by Derjaguin, Landau, Verweey, and Overbeek (DLVO) theory for low concentration NF as shown in equation (4.2)

$$E_{el} = \frac{\epsilon_0 \epsilon_1 r_1 r_2}{r_1 + r_2} \{2\Psi_{d1}\Psi_{d2} \ln \left[\frac{1+ \exp(-kx)}{1- \exp(-kx)}\right] + (\Psi_{d1}^2 + \Psi_{d2}^2) \ln[1-\exp(-2kx)]\} \quad (4.2)$$

Here, Ψ_{d1} and Ψ_{d2} are the surface potential of interacting particles, r is particle radius, x is the interparticle distance, ϵ is electric permittivity and k is the thermal conductivity of the system. Higher zeta potential leads to a bigger potential barrier for particle aggregation. At the point of zero charges (PZC), the second term of the equation becomes negligible which means the repulsion energy between the same size particles becomes proportional to the square of zeta potential. Attraction energy between the particles of the same material can be defined by Hamaker equation (equation 4.3)

$$E_A = -A_{132}\, r / (12x) \tag{4.3}$$

Here A_{132} is Hamaker constant and for metal oxide, it is in the order of 10^{-20} J. Using equations 4.2 and 4.3 Ψ_d and E_A can be calculated as a function of x for different pH. Away for the IEP, the repulsion barrier becomes bigger than attraction making stable NF. Suspension stability can be quantified in terms of collision efficiency α. α is the reciprocal value of stability coefficient W (related to aggregation rate constant, *k*) and is responsible for colloid particle growth can be represented as (equation 4.4)

$$K = \alpha\, k_{diff} = k_{diff}/W \tag{4.4}$$

Here k_{diff} is the rate constant of clustering among uncharged particles. And W is described as (equation 4.5)

$$W = 2r \int_0^{\infty} \left(\frac{E_{Tot}}{K_b T}\right) \frac{dx}{(2r+x)^2} \tag{4.5}$$

Additionally, changing pH changes the degree of particle aggregation. According to this theory, with the increase of intraparticle distance, valance state of counterions and concentration of added NP repulsive force decreases exponentially[136]. Optimum pH for a stabilized NF depends on the NF itself and different from one another.

Ultrasonic bath, homogenizer, or probe sonication are other useful tools to break the NP aggregation to get stabilized NF and different from other techniques as no change in surface properties is needed. However, finding optimum sonication conditions is still a challenge as excess sonication can lead to more aggregation because of increased surface energy. In most of the cases, researchers combined multiple of these techniques to get stabilized NF. It is to be noted that, only by using the Ultrasonication method it is difficult to get stable NF for more than 24 hours and more investigations are needed to define a well-established route.

Various techniques have been adopted by the researchers to investigate nanofluid stability i.e. zeta potential measurement, UV-Vis spectroscopy, visual inspection, TEM/SEM imaging, etc.

4.5 Mechanisms of Thermal Conductivity Improvement of NF

Reports have been found that NF increases the thermal conductivity though lack of agreement on these reported values fails to predict the appropriate reason for the increase[144]. On the other hand, there is no definitive formula to predict the thermal conductivity of nanofluid, some semi-empirical formulae for two-phase mixtures are adopted. Maxwell model, Bruggeman model, or even Hamilton crosser model are all

based on a classical model derived from continuum formulations and only include limited factors like particle shape and volume fraction and cannot give a rationale for the excellent increase of thermal conductivity of NFs. So far, four main mechanisms for thermal conductivity improvement have been discussed and accepted by the scientific community i.e.

1. Nanoparticle Brownian motion
2. Molecular-level layering of liquid particle interface
3. Nature of heat transport in nanoparticles and
4. Effect of nanoparticle clustering.

4.5.1 Particle Brownian Motion

Brownian motion of particles has been considered by many researchers for explaining the NF thermal conductivity. In the traditional approach, particles in a solid/fluid suspension are considered motionless in continuous material[145] which is not the actual case for NFs because of the constant Brownian motion of particles. Brownian motion can be expressed in terms of particle diffusion constant D, given by Stokes-Einstein formula (equation 4.6)

$$D = \frac{k_B T}{3 \pi \eta d} \tag{4.6}$$

Here, k_B is Boltzmann constant, η is fluid viscosity, and d is particle diameter. Because of the Brownian motion, particles or molecules are always in collision with one another. Researchers have discussed 4 modes of energy transport due to Brownian motion in

nanofluids i.e. collision between fluid molecules, thermal diffusion in NPs, the collision between NPs, and thermal interaction of dynamic nanoparticles with fluid molecules.

The effect of Brownian motion can be estimated from this equation by comparing the particle motion time with the heat diffusion in the liquid medium. The required time for a particle to move by the distance same as its own size τ_d can be calculated as follows (equation 4.7)

$$\tau_d = \frac{d^2}{6\,D} = \frac{\pi \eta\, d^3}{2\, k_B\, T} \tag{4.7}$$

required time for the heat to move in the liquid by equal distance τ_H can also be estimated (equation 4.8)

$$\tau_H = \frac{d^2}{6\,\chi} = \frac{d^2 c_p \rho}{6\, k_f} \tag{4.8}$$

For known values of these parameters of water at room temperature (η =0.01 g/cm.s, ρ =1 g/cm^3, c_p =4.2 J/g and k_f =0.4 W/m.K) with a particle diameter of 10 nm dispersed in liquid yield the value of τ_d and τ_H as 2 x 10^{-7}s and 4 x 10^{-10} s respectively. The ratio of τ_d/τ_H decreases to 25 if the particle size reaches atomic size. This means even for smaller particle, thermal diffusion is faster than Brownian diffusion. That is why Brownian motion alone cannot explain the increased value of thermal conductivity in a nanofluid (as it is too slow to transport heat).

4.5.2 Molecular Layering

It is well accepted that liquid molecules show good structural ordering at the solid-liquid interface and can be accounted for the increase in thermal conductivity. Some researchers argued that the presence of interfacial resistance (Kapitza resistance) can increase thermal conductivity though many researchers have opposed the idea. However, the consideration of Kapitza resistance can make an overestimation of k from the Hamilton crosser model which suggests thermal conductivity decreases with decreasing particle size and contrary to experimental findings[146].

For predicting the upper limit of the effect of liquid layering on thermal conductivity, we can assume that the thermal conductivity of this layer is the same as the solid particle. The larger the effective volume of the particle (sum of particle diameter and liquid layer thickness) higher the effective thermal conductivity as shown in Figure 4.4. In order to double the effective particle volume for a particle with 10 nm diameter, a 2.5 nm layer thickness is needed though experimental as well as simulation results from reports show that the width of this interfacial layer is only on the order of few atomic distances (1 nm)[147], [148] and can affect the thermal conductivity. However, Keblinski et al. [90] on the other hand argued that considering the liquid layer as the only reason for conductivity increase yields value which is one order of magnitude more than the value predicted by the HC model which undermines the possible explanation of the increase in thermal conductivity due to molecular layering.

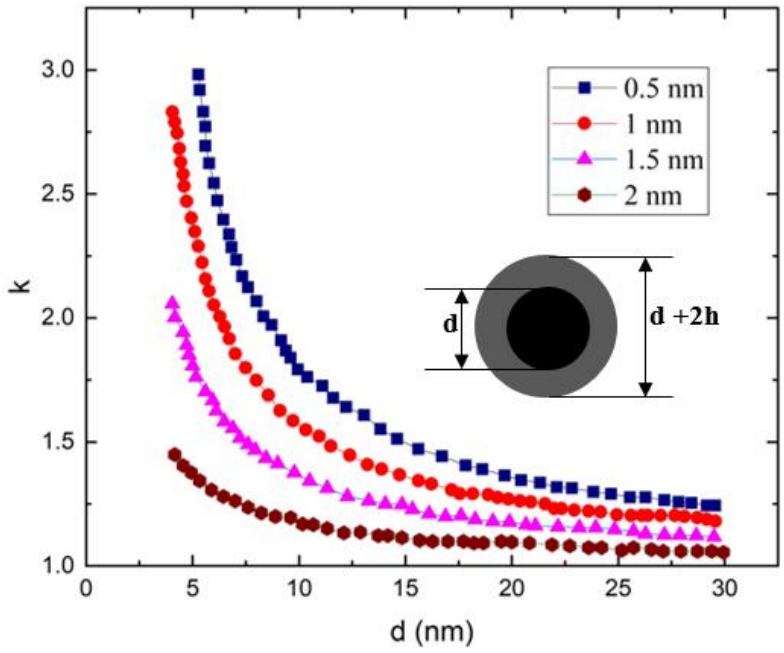

Figure 4.4. Thermal Conductivity Improvement due to the Formation of the Conductive Layer at the Particle-liquid Interface for Different Layer Thickness (h) [90]

4.5.3 Nature of Heat Transport (Phonon Theory)

Researchers reasoned the contribution of free electrons in a metal nanofluid as one of the main factors for thermal conductivity increase. To explain this unusual increase in conductivity, different models have been developed i.e. mean-field theory [149], aggregation model[150], and particle Brownian motion model[151], etc. by researchers. In these models, metallic nanofluids are considered the same as non-metallic NFs though the heat transfer pathways are different for these systems. In metallic nanofluids, free electrons are dominant to carry heat whereas phonons are the main means in non-metallic ones. However, researchers found that there is hardly any direct interaction between electrons of metals and non-metal phonons in the metal non-metal interface, rather heat is transferred between metal phonons and non-metal phonons[152].

In case of nanofluids where there is no long range order, direct coupling between fluid vibrational mode and electron wave function is very weak. As a result, temperatures of phonon and electron are different especially if there is any heat flux passing through the interface and conduction of heat between phonon and electron is necessary to gain thermodynamic equilibrium. Exchange of heat in this case can undergo via two main processes i.e. (i) metal electrons and non-metal phonon interaction at the interface and (ii) metal electrons and metal phonons coupling followed by heat exchange between phonons in both sides of the interface.

In the case of nanofluids, phonons can be taken as main heat carriers like nonmetal solids[153]. Figure 4.5 shows the temperature profile at the metal-nonmetal (liquid in case of nanofluids) interface considering that heat flux passes through the x-axis. An unbalance of temperature between electrons (T_e) and phonons (T_p) occurs at the metal-liquid interface as the heat transfer capacities are different for them. Results have shown that the heat is transferred through the interface via coupling between electrons and phonons of metals, followed by the exchange of heat among phonons from both sides of the interface. Apparent temperature of nonmetal, T_n is lower than that apparent temperature of metal, T_a. Metal phonon flows through the interface to nonmetal resulting in a decrease of metal phonon temperature, T_p. At the same time, metal electrons do not exchange heat with nonmetal phonons. As a result, electron temperature, T_e is higher than T_p. At the interface(x=0) because of the insulating boundary layer condition $\delta T_e/\delta x \sim 0$.

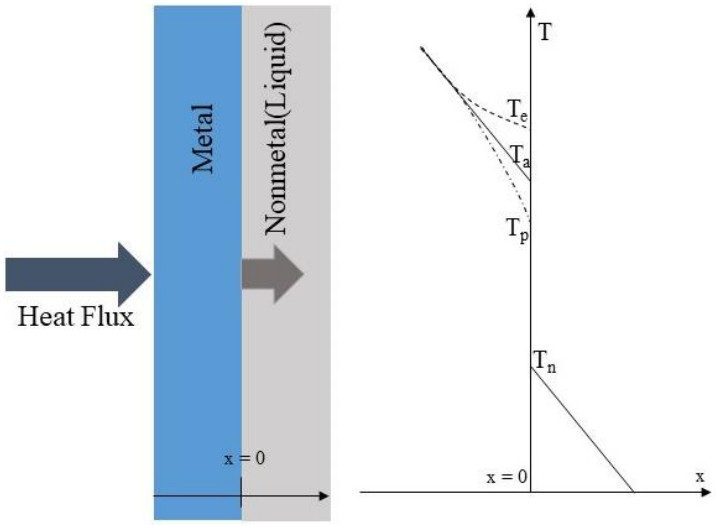

Figure 4.5. Interface Thermal Resistance and Temperature Distribution at the Metal-nonmetal Interface [154]

Energy balance equations of phonons and electrons can be expressed by the two-temperature model as shown [152], [155] (equation 4.9 and equation 4.10)

$$k_p \frac{d^2 T_p}{dy^2} + G (T_e - T_p) = 0 \quad (4.9)$$

$$k_e \frac{d^2 T_e}{dy^2} - G (T_e - T_p) = 0 \quad (4.10)$$

where k_p and k_e are thermal conductivity of phonons and electrons and G is the electron-phonon coupling factor that measures the energy transfer per unit volume from electron to phonon. If the value of Te is larger than Debye temperature T_D, G can be expressed as (equation 4.11)

$$G = \frac{\pi^2 v_a^2 m_e n_e}{6 \tau_e T_e} \quad (4.11)$$

Here, v_a is the average group velocity of phonons, m_e and n_e are electron mass and number density of electron and τ_e represents electron energy relaxation time.

According to the Debye theory, considering a lattice constant of 50 A^0, Gruneisen parameter of 1 and ratio of particle melting temperature and reference temperature 7 (for alumina NPs) phonon mean free path is calculated as 35 nm. If the particle size is less than 35 nm, phonon cannot diffuse through and diffusive nature of heat transport which is the basis of macroscopic theories is not valid[144]. Keblinski et al.[90] proposed that phonons must move ballistically in case of NF rather than diffusive heat transport.

4.5.4 Effect of Nanoparticle Clustering

Particle clustering can be a major phenomenon in explaining the increase in effective thermal conductivity of NF as it creates paths with low thermal resistance. Though clustering is favorable to some extent, agglomerates with large span distance are more prone to settling thus decreasing the efficiency. Though percolating structures are most unlikely in the case of NF, local clustering has been proved experimentally[156]. If the effective cluster volume (where another cluster volume is excluded from individual cluster volume) is higher than an individual particle, heat can move rapidly within the cluster. As a result, the volume fraction φ (as stated in the Hamilton-Crosser model) of this highly conductive phase is larger than solid volume and can increase the thermal conductivity rapidly.

Figure 4.6 shows the increase in thermal conductivity with cluster packing fraction φ (ratio of solid particle volume in a cluster to total cluster volume). If the

packing fraction is decreased i.e. when the total volume of a cluster is increased due to particle separation, the thermal conductivity increases significantly. Even closely packed particles have at least 25% liquid in them, though the effective cluster volume is 30% higher than that of dispersed particles [90].

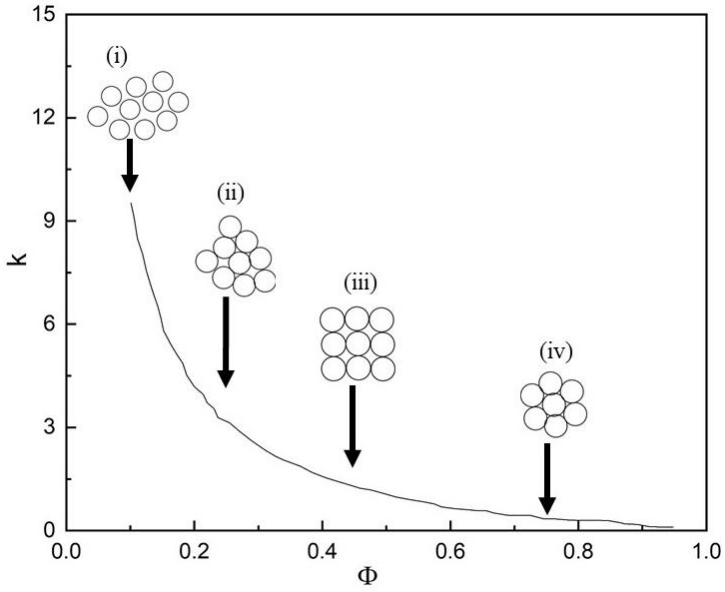

Figure 4.6. Effect of Cluster Packing Fraction on Thermal Conductivity. (i) Particles Separated by Thin Liquid Layer among them Allowing Rapid Heat Flow, (ii) Randomly Packed Particles where they are in Contact to one another, (iii) Cubic Structure of Particles and (iv) Closely Packed fcc Structure [90]

If the particles are more dispersed, then the increase in effective volume is even more which in turn decreases the cluster packing fraction. A drastic increase of k value has been found if the clusters are not in physical contact rather within a specific distance which allows rapid heat flow because of ballistic phonon effect. However, a further increase in cluster size leads to a less efficient NF system, especially at low particle

volume fraction. More experimental works are still needed to conclude on the role of aggregation on thermal property.

4.6 Thermal Conductivity Measuring Techniques

The most popular and common techniques for thermal conductivity measurement of fluids are Hot-wire method, steady-state method, and optical method. These methods are discussed in brief here.

4.6.1 Transient Hot Wire (THW) Method

This method is considered one of the most popular methods and widely used for measuring the thermal conductivity of fluids. This method is a dynamic technique that records the temperature rise at a specific distance from a hotwire embedded (works as a heat source) test material. The hot wire is considered to have uniform output along test sample length and the thermal conductivity is then measured over known time. The THW measurement technique is illustrated in Figure 4.7. Temperature rise $\Delta T(r,t)$ for any distance r from the heat source (in this case hot wire) can be described as a function of time (t) and is expressed as follows (equation 4.12)

$$\Delta T(r,t) = \frac{q_1}{4\lambda\pi} \ln \frac{4at}{r^2 C} \tag{4.12}$$

Here, q_1 is constant heat flux, λ represents thermal conductivity, a is thermal diffusivity, and $C = \exp(\gamma)$ where γ Euler's constant. Several researchers have used this technique to study the thermal conductivity of nanofluid[104], [110], [157], [158].

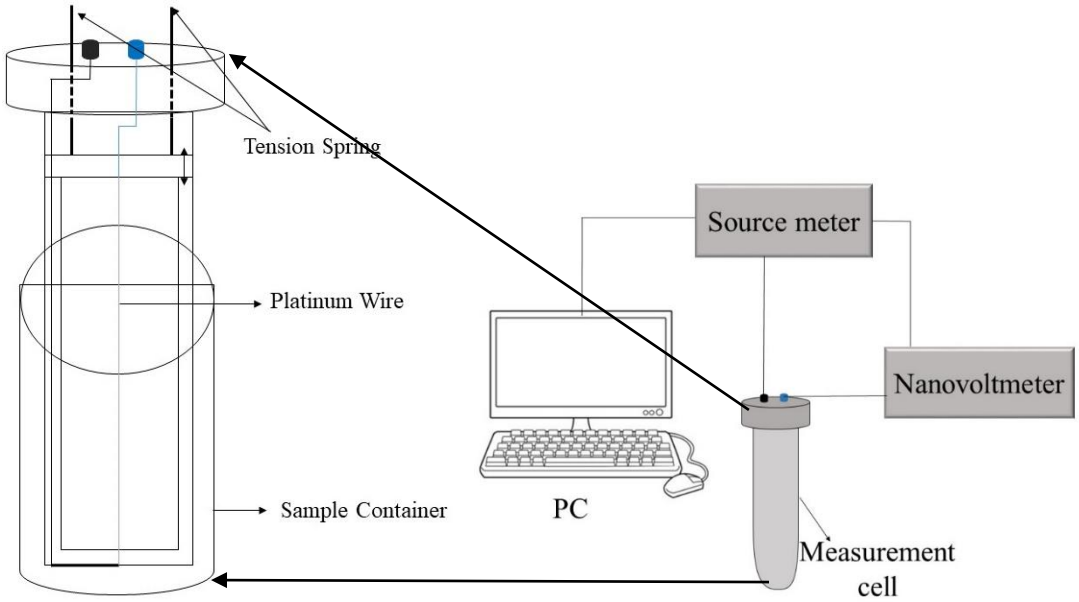

Figure 4.7. Typical Hotwire Setup

4.6.2 Temperature Oscillation Method

This method was first proposed by Roetzel et al. [159] and in this method, the temperature fluctuations of nanofluid are measured when a heat flux or temperature oscillation is applied. The temperature response indicates localized or averaged conductivity in the sample chamber direction height. The experimental setup consists of (1) specially fabricated test cell, (2) cooling water system, (3) thermostatic bath, (4) DC supply, (5) amplifier and filter, (6) data acquisition system and (7) PC with suitable software for analyzing and processing data as illustrated in figure 4.8. Thermal diffusivity can be measured accurately by considering the thermal oscillation amplitude sample (in this case nanofluid) material interface to the center of the fluid.

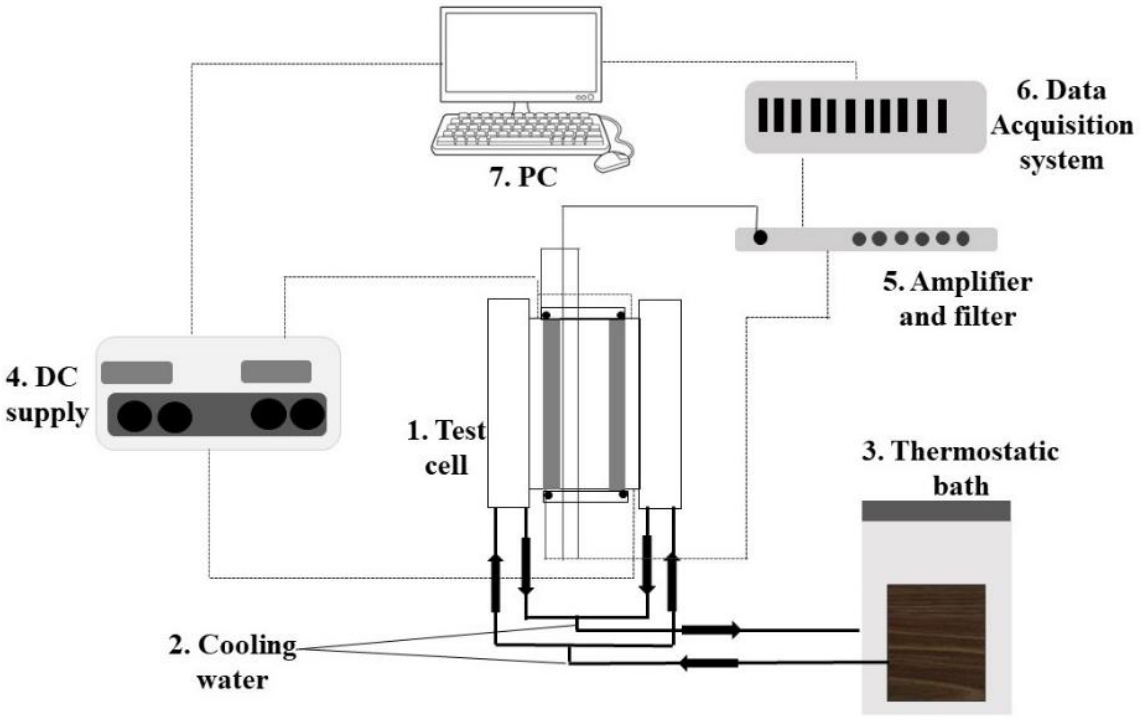

Figure 4.8. Experimental Setup of Temperature Oscillation Method

The problem with this method is that the thermal conductivity is not accurate. Das et al. used this technique to measure the thermal conductivity of water-based nanofluid comprising of Al_2O_3 and CuO nanoparticle[94].

4.6.3 Thermal Constants Analyzer Technique

In this process, the thermal conductivity of nanofluid is measured following the transient plane source (TPS) theory, where the TPS element acts both as a heat source and temperature sensor. The main principle is somewhat similar to the transient hot-wire method as thermal conductivity is calculated based on the Fourier law of heat conduction. However, the advantages are fast measurement, a wide range of thermal conductivity (0.2

to 200 W/m K) can be measured, minimal or no sample preparation needed, simplicity of the process, and flexibility of sample size. A schematic of this method is illustrated in figure 4.9.

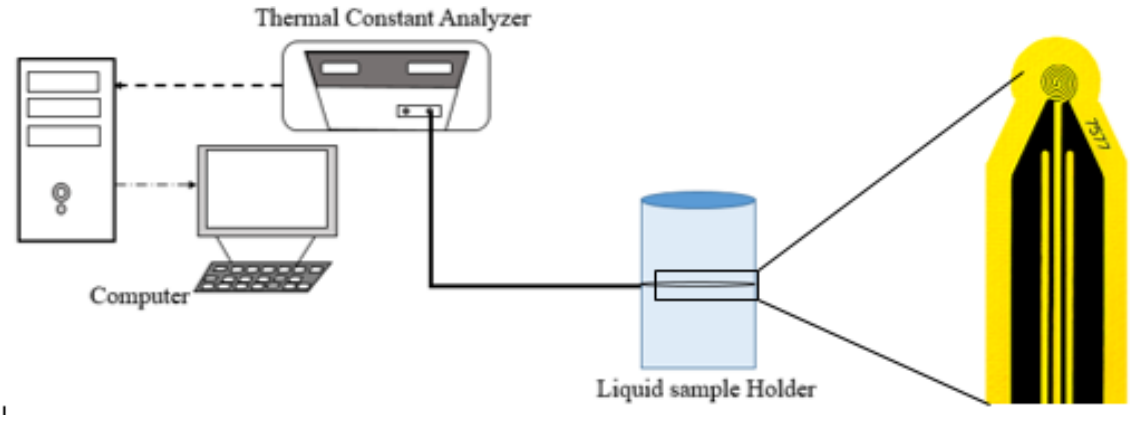

Figure 4.9. Schematic of Typical TPS Instrument

A typical TPS setup usually consists of a thermal constant analyzer that is connected to a computer (where a suitable operating software is used to run an experiment), a liquid cell holder, and an appropriate probe sensor. The probe sensor acts both as the heat source and sensor.

Time dependent temperature rise data is collected and used for determining the thermal properties of nanofluid. Fundamental transient heat conduction equation with a semi-infinite boundary condition is used for the calculation as stated below (equation 4.13)

$$k\nabla^2 T + \frac{Q}{\rho c_p} = \frac{\delta T}{\delta t} \qquad (4.13)$$

Here, k is the thermal conductivity of material, Q denotes heat flux, ρ is density, and C_p is specific heat capacity. Semi-infinite boundary condition is satisfied by computing the penetration depth, Δp (equation 4.14)

$$\Delta p = 2\sqrt{\alpha \, . \, t} \tag{4.14}$$

Here, α is thermal diffusivity and t is the measurement period. Solution for an average temperature increase of the sensor is a function of its geometry and power applied to the sensor which can be stated as follows (equation 4.15 and equation 4.16)

$$\Delta T\,(\tau) = \frac{P_0}{\pi^{\frac{3}{2}} \, . \, r \, . \, \alpha} D\,(\tau, k) \tag{4.15}$$

And

$$T = \frac{\sqrt{k\, t}}{r} \tag{4.16}$$

where, ΔT is average temperature increase of the sensor, P_0 is sensor heating power, r is sensor radius and D(τ) is dimensionless time function. After fitting the data taken experimentally to the straight line given by this equation, thermal conductivity value is calculated from the slope of the fitting line.

The liquid sample was placed inside the holder with the sensor making sure the sensor is fully immersed in a fluid. Assuming a temperature rise at a point(y, z) in the liquid cell holder at a certain time t because of the output power of the probe per unit area Q can be expressed as (equation 4.17)

$$\Delta T\,(y, z, t) = (8\,\pi^{3/2}\,\rho c)^{-1} \int_0^T d\tau\,[\alpha(t-t')]^{-3/2} \int_A dy'dz' \times Q\,(y', z', t') \exp \left\{-\left[\frac{(y-y')^2+(z-z')^2}{4\,\alpha\,(t-t')}\right]\right\} \quad (4.17)$$

here, ρ is density (kg/m^3), c is specific heat (J/kg K) and α is thermal diffusivity (m^2/s) of the sample. Further simplification of the equation can be done by taking $k(t-t') = \sigma^2 a^2$ (a is sensor radius) and can be written as (equation 4.18)

$$\Delta T\,(y, z, t) = (4\,\pi^{3/2}\,a\,k)^{-1} \int_0^T \frac{d\sigma}{\sigma^2} \int_A dy'dz' \times Q\,(y', z', t') \exp \left\{-\left[\frac{(y-y')^2+(z-z')^2}{4\,\sigma^2 a^2}\right]\right\} \quad (4.18)$$

Where, k is thermal conductivity[160]. This method gives a consistent result produced by commonly used transient hot-wire technique[161], [162]. This method has been followed by Jiang et al.[163] and Zhu et al.[164] to measure nanofluid thermal conductivity.

4.6.4 3ω Method

This method uses a radial heat flow from a single element acting both as heater and thermometer which is similar to the THW method. This method uses temperature oscillation rather than a time-dependent response which is used in THW. A sinusoidal current with ω frequency is passed through the metal wire and a heatwave with 2ω frequency is produced which is gathered by voltage component at 3ω frequency. 3ω device is fabricated by metal deposition and patterning and connected to metal heaters. Nanofluid is confined in a well around the heater and the whole system is placed inside a temperature-controlled cryostat[165]. This method is suitable to measure the temperature-

dependent thermal conductivity of nanofluid. Oh, and co-workers[166] used the 3ω method to measure the thermal conductivity of Al_2O_3 dispersed DI water and ethylene glycol at room temperature.

Apart from these methods, cylindrical cell method[167], nanoflash method[168], etc. have been applied for the thermal conductivity measurement of various nanofluids by different researchers.

4.7 Methodology

4.7.1 Preparation of Co Nanowire Based Nanofluid

A two-step approach is adopted to get a well-stabilized nanofluid and is shown in Figure 4.10. First, our synthesized Co nanowires were treated with Oleic acid ($C_{18}H_{34}O_2$) (OA) at 80 ^{0}C for 3-4 hr as it has been reported that, OA can be adsorbed onto the surface of Co nanoparticle[169] and can help with nanofluid stability. Methanol (OA: Methanol = 1:1) was also added for better mixing. To aid this treatment process additional 1 hr of ultrasonication at 60 ^{0}C along with probe sonication was performed. Using the magnetic decantation technique, these treated nanowires were then washed several times using methanol to remove excess OA. Nanowires then are kept under vacuum overnight for drying. After the drying process, 6 mL DI water was added. Finally, probe sonication was done for 1 minute to break agglomerates and homogenize the nanofluid. Diluted HCl and NaOH were used to change the pH of nanofluid. Two different volume concentrations of 0.01% and 0.02% were used at different pH values for the study.

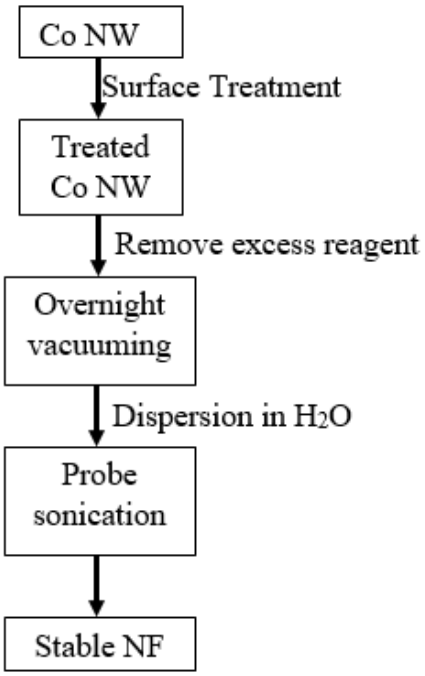

Figure 4.10. Schematic Representation of Co Nanofluid Preparation

Volume fraction can be calculated directly from the weight of added particle and base fluid. TGA analysis was done to measure the weights of nanoparticle and base fluid. The following formula was used (equation 4.19).

$$\text{Volume Fraction, } \%\varphi = \frac{\frac{W_{ap}}{\rho_{ap}}}{W_{ap}/\rho_{ap} + W_{bf}/\rho_{bf}} \text{ x } 100 \qquad (4.19)$$

where, W and ρ indicate the weight and density respectively; ap and bf indicate added particle and base fluid.

And W_{ap} = weight of added particle

ρ_{ap} = density of added particle (Co nanowire) = 8.9 g/cc

ρ_{bf} = density of base fluid (water) = 1g/cc

and W_{bf} = weight of base fluid

4.7.2 Thermal Conductivity Measurement

Thermal conductivity of nanofluid was measured in a liquid cell using Transient plane source (TPS) method. Transient Hot Disc TPS 2500s instrument was used with 7577 kapton probe. The radius of the TPS element is 2.001 mm (maximum uncertainty, k=2) to conduct the study as shown in figure 4.11.

Figure 4.11. TPS Setup for Fluid Thermal Conductivity Measurement

To keep the probe and liquid cell firm in position a special base was 3D printed. To avoid natural convection, a very low thermal power (30 mW) with short measuring time (10s) was used. It is to be mentioned that, the measurements should be performed at minimum external vibration as any type of vibration can affect the results. Thermal conductivity measurement was done at least 3 times for each condition (72 times). Between each test at least 15 minutes of time interval was maintained in order to cool TPS element.

4.8 Results and Discussions

4.8.1 Zeta Potential Measurement

Water based Co NW-NF stability is mainly dependent on electrokinetic properties where high surface charge can induce strong repulsive force among suspended NWs. That is why zeta potential measurement is an important phenomenon to study electrophoretic behavior thus, in turn, the dispersion stability[160] and has been used by various researchers. Figure 4.12 shows the variation of zeta potential values with respect to pH from 4.0 to 12.0 for surface-modified NF and as prepared nanofluid (before surface modification of nanowire) of 0.01 vol%. The pH was controlled adding diluted NaOH and HCl in nanofluid solution and measured by using a digital pH meter (Thermo Scientific Orion Star A111) for accurate values (relative accuracy of ±0.01).

Zeta potential was measured by dynamic light scattering method (DLS) using Malvern zeta sizer (ZEN 3600). For accurate results, samples were first diluted by adding

5 µL of nanofluid in 5 mL of aqueous solution with same pH value as the nanofluid. Then the sample was loaded in a folded capillary tube with care to avoid bubble formation. For the measurement options, Smoluchowski approximation of Henry's function (f(ka)= 1.5) was used with Backscatter detection (175^0 detection optics).

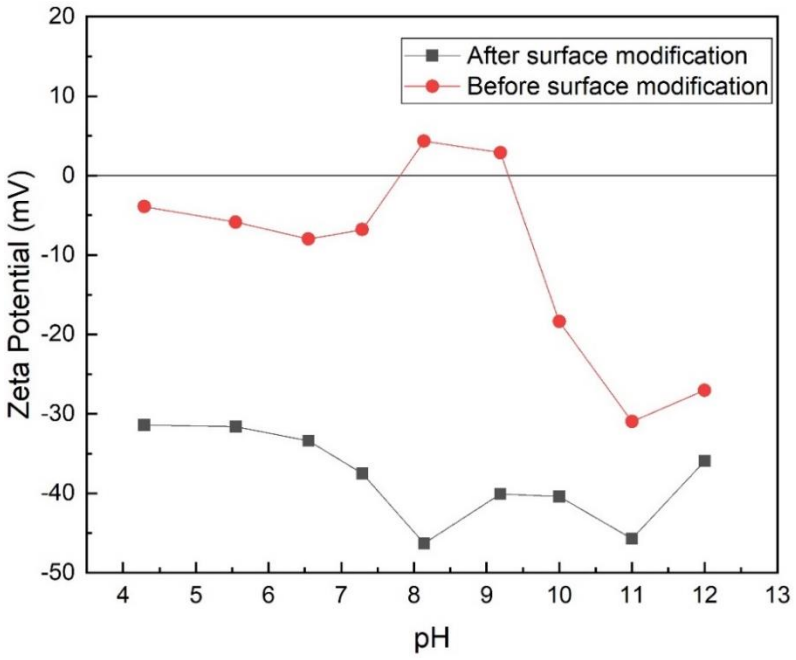

Figure 4.12. Effect of pH on Zeta Potential Value for Nanofluids of before and after Nanowire Surface Modification

We can see that, as prepared nanofluid has negative zeta value at all pH except in the range of 8-9 which can be the point of zero potential for cobalt based nanofluid. However, the absolute value of zeta potential <30 mV which indicates the nanofluids are not stable. For a stable nanofluid, the absolute zeta potential value must be >30mV[170]. After surface modification of the nanowires, the absolute value of zeta potential is higher than 30 mV. Maximum absolute zeta potential value was attained for pH value of 8.14

and 11(48 mV and 46 mV respectively). However, we can also see that point of zero surface charge (PZC) for cobalt nanofluid lies between 7.5-9 pH.

At PZC, there is no repulsive force among the suspended Co nanowires and they will coagulate together according to DLVO theory[135]. Besides, pH value further away from the PZC induces more charged sites providing more effective passage through phonons or heat can transfer more efficiently[171].

4.8.2 FTIR Analysis

Agilent 670 FTIR spectrometer was used for the analysis. Figure 4.13 shows the Fourier Transformation Infrared spectroscopy result of OA (Figure 4.13 (a)) and OA treated Co NW (Figure 4.13 (b)). For pure OA, two major bands were found at 2854 cm^{-1} and 2921 cm^{-1} corresponding to symmetric $–CH_2$ stretch and asymmetric $–CH_2$ stretch respectively[172], [173]. We can also see the characteristics OA peak at at 1708 cm^{-1}. Bands at 1464 cm^{-1} and 941 cm^{-1} represent O-H stretch in-plane and out of plane respectively[172], [174].

FIT-IR analysis of OA treated Co nanowire on the other hand, show peaks at 2913 cm^{-1} and 2854 cm^{-1} which indicates the presence of OA on the surface. Characteristic Oleic acid peak at 1708 cm^{-1} is almost absent in treated nanowire (curve b) whereas two new peaks at 1637 cm^{-1} and 1415 cm^{-1} were found which corresponds to the symmetric V_s(COO-) stretch and asymmetric V_{as} (COO-) stretch [175]. This result can explain that the bonding pattern of the carboxylic acids on the surface of the nanoparticles was bonded symmetrically and molecules bonded at an angle. The presence

of these new carboxylic acid bands indicates that the surface of the cobalt nanowires is modified chemically.

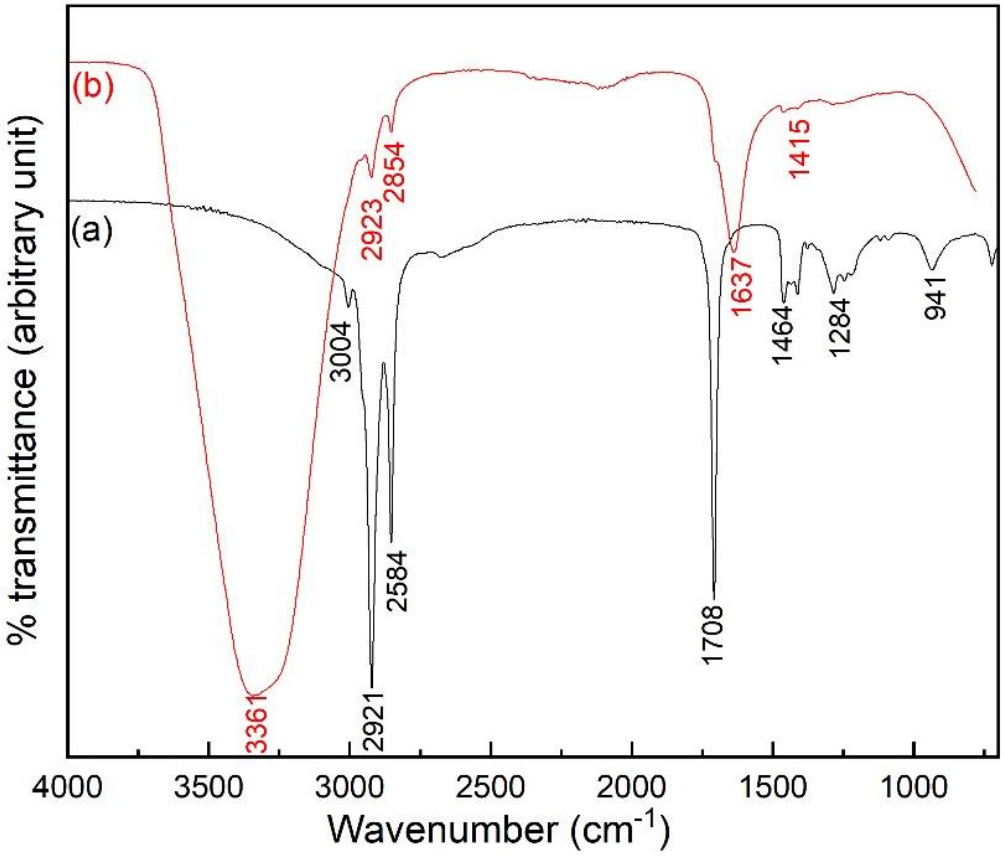

Figure 4.13. FT-IR Spectra of (a) Pure Oleic Acid, (b) OA Treated Co NW

A broad band of 3361 cm^{-1} is found, which is attributed to –OH stretching vibrations coming from water. These results can reveal that OA is chemically adsorbed on the surface of Co nanowire. Because of this chemical surface modification, the process is quite stable and can be used for further experiments.

4.8.3 Thermal Conductivity of Cobalt Nanofluid

Thermal conductivity of DI water was measured initially using TPS technique to validate our results. The thermal conductivity of DI water is 0.613 W/m.K (from the literature[176] at room temperature. From our experiments, we measured the thermal conductivity value of 0.614 W/m.k with an error of 0.03% only. The results are compiled in table 4.2.

Table 4.2. Comparative Study of Thermal Conductivity for DI Water

	Thermal Conductivity (W/m.K) Literature	Thermal conductivity (W/m.K)			% Error
		1	2	3	
DI Water	0.613	0.6155	0.614	0.6128	±0.03%

For reference, aqueous solution of different pH was used where the pH of DI water was changed using dilute HCl and NaOH. Figure 4.14 shows the thermal conductivity values for reference aqueous solution and Co nanowire based nanofluid at 0.01 and 0.02 vol%. We can see that, pH has a minimum effect on the thermal conductivity for aqueous solution as thermal conductivity value is 0.613±.003 W/m.K. However, for nanofluid with 0.01 vol% we can see a significant increase in thermal conductivity when compared to the reference solution at all pH values. For example, at a pH of 4.29 thermal conductivity is 0.665 W/m.K which is an 8.5% increase compared to the base fluid. In most of the cases, we can see thermal conductivity gradually increases as the pH value increases except for 6.55. On the other hand, more increase in thermal

conductivity was observed for 0.02 vol% nanofluid. At a pH of 4.29, the thermal conductivity is 0.699 W/m.K which is a 14% increase if compared to the reference solution. Similar to 0.01 vol%, thermal conductivity shows an increasing trend with increasing pH though not significant.

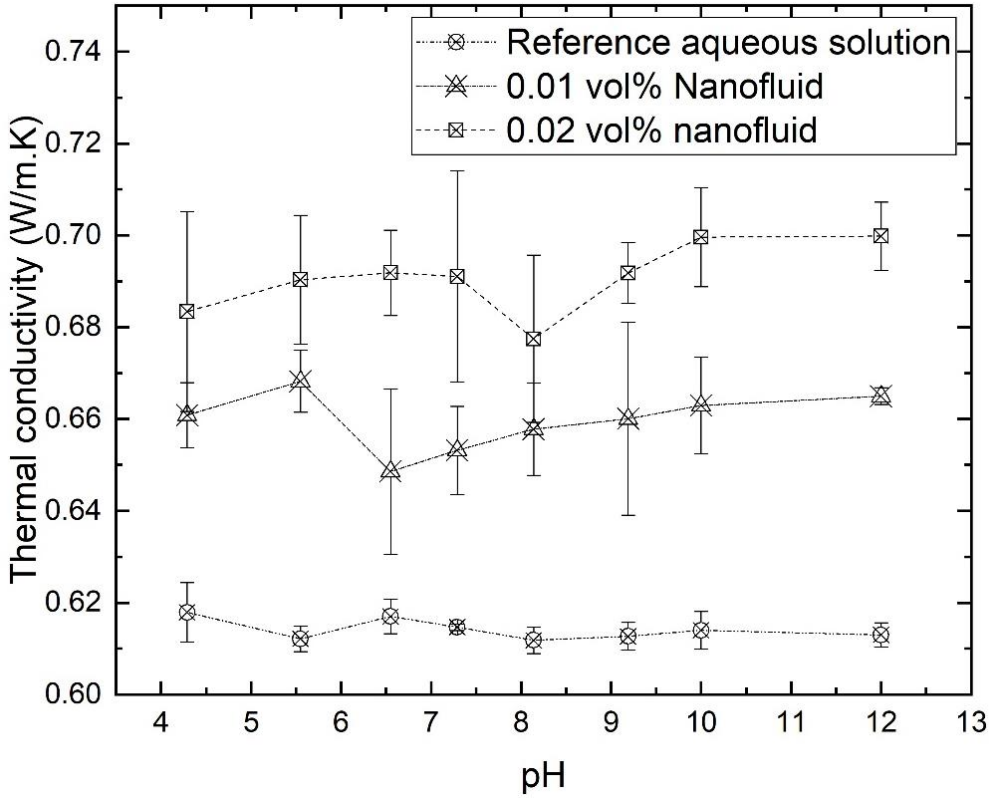

Figure 4.14. Thermal Conductivity of Aqueous Solution and Nanofluid with Different Volume Concentration

It is to be mentioned that, the thermal conductivity measurement was done at a constant temperature of 21 ^{0}C.

When the nanoparticles are dispersed in aqueous media, the particle-media interaction behavior depends on the particle surface properties. Deviation of pH value

from PZC increases the hydration forces among particles enhancing the particle mobility in the suspension. This microscopic motion causes micro convection which in turn enhances the heat transport process. Besides, change in pH can affect other mechanisms for thermal conductivity increase which needs to be studied. Although we can see there is a trend of increasing thermal conductivity with increasing pH, we do not see any significant increase in TC value. We can also see that thermal conductivity decreases at pH value of 6 to 7 for 0.01 vol% which can be accounted to PZC as discussed before. For 0.02 vol%, we can see a similar dip in thermal conductivity value at 8 pH.

4.8.4 Models for Thermal Conductivity of Nanofluid

Since the Maxwell model, scientists developed various models for NF thermal conductivity to corroborate theoretical studies with experimental results. It is to be noted that, all these models are derived from the Maxwell model for calculating the effective thermal conductivity of solid-liquid mixture. According to the Maxwell model[145], the effective thermal conductivity of a solid-liquid mixture (k_{eff}) having spherical solids can be described as follows (equation 4.20)

$$\frac{k_{eff}}{k_f} = 1 + \frac{3\left(\frac{k_p}{k_f}-1\right)\varphi}{\left(\frac{k_p}{k_f}+2\right)-\left(\frac{k_p}{k_f}-1\right)\varphi} \tag{4.20}$$

here, k_{eff} = effective thermal conductivity of suspension, k_f = liquid thermal conductivity, k_p = thermal conductivity of solid particles and φ = % volume fraction of

nanoparticles. Bruggeman [177] then proposed another model where he considered the interaction among randomly distributed solids for any concentrations which state (equation 4.21)

$$\varphi \left(\frac{k_p - k_{eff}}{k_p + 2\, k_{eff}} \right) + (1 - \varphi) \left(\frac{k_f - k_{eff}}{k_f + 2\, k_{eff}} \right) = 0 \tag{4.21}$$

At low particle concentrations, the Bruggeman model agrees well with the Maxwell model and experimental results. However, at high concentration, the Maxwell model fails to predict thermal conductivity while the Bruggeman model provides acceptable results. In both models, only spherical particles were considered. Hamilton and Crosser first considered particle shape and modified these models for non-spherical particles in 1962. Hamilton-Crosser model is expressed as follows (equation 4.22)

$$\frac{k_{eff}}{k_f} = \frac{k_p + (n-1)\, k_f - (n-1)\varphi\, (k_f - k_p)}{k_p + (n-1) k_f + \varphi (k_f - k_p)} \tag{4.22}$$

Here, n=shape factor (for sphere, n=3 and for cylindrical shape, n=6). All these models only consider particle volume fraction or shape as key variables and assume diffusive heat transport in both solid and liquid phases. Keblinski et al.[90] later considered additional possible factors to influence the NF effective thermal conductivity i.e. particle clustering, molecular layering, etc. Choi and co-workers[178] thus modified the Maxwell model to include molecular layering on particle liquid interface and introduced modified thermal conductivity k_{pe} in the place of particle thermal conductivity k_p and is based on effective medium theory. Their model is expressed as (equation 4.23)

$$k_{pe} = \frac{[\,2(1-\gamma)+(1+\beta)^3\,(1+2\gamma)\gamma]}{-(1-\gamma)+(1+\beta)^3\,(1+2\gamma)}\,k_p \qquad (4.23)$$

here, $\gamma = k_{layer}/\,k_p$ which is the ratio of nano-layer thermal conductivity to nanoparticle thermal conductivity and $\beta = h/r$ is the ratio of nanolayer thickness and original particle radius. Other researchers also contributed to propose various models for different factors and types of nanofluids[179], [180]. Wasp model for thermal conductivity was also used for the solid liquid mixture to predict thermal conductivity of TiO_2/ water nanofluid by Wang et al.[181]

$$\frac{k_{eff}}{k_f} = \frac{(k_p+2\,k_f-2\,\varphi\,(k_f-k_p)}{k_p+2\,k_f+\varphi\,(k_f-k_p)} \qquad (4.24)$$

We have compared our experimental findings with these models specifically with the Maxwell model where there is no shape factor involved and Hamilton-Crosser model where shape of nanowires is considered as shown in figure 4.15.

From the figure, we can see that our experimental findings correlate well with the Hamilton crosser model for variation of added particle concentration. At low volume concentration, only 1.7% of thermal conductivity is underpredicted by Hamilton crosser model whereas the value of under prediction is only 0.7% at the higher volume concentration.

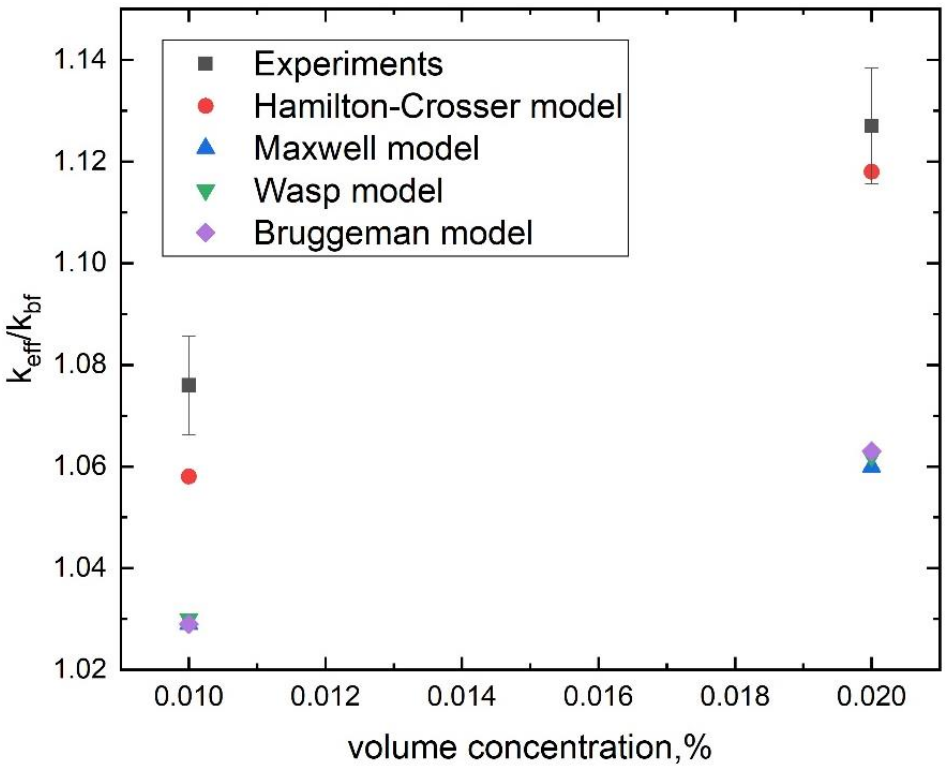

Figure 4.15. Comparison of Experimental Findings with Maxwell and Hamilton-Crosser Model

However, comparing with the Maxwell model, we can see that there is a huge deviation with our findings, and this model underpredicts the thermal conductivity ratio by 4% whereas, at higher concentrations, the underprediction is even higher at 6.3%. Other models like the Bruggeman and Wasp model give similar predictions to the Maxwell model and underpredict thermal conductivity values for our experimental findings. From this study, we can say that the Hamilton-Crosser model is more suitable for predicting the effective thermal conductivity of Co nanowire based nanofluid, and at higher concentration, it is possible to predict accurately. However, further study is needed for higher concentration to come into that conclusion.

4.8.5 Possible Mechanism of Thermal Conductivity Increase

Researchers argued that the abnormal increase in thermal conductivity of nanofluids can be accounted for the particle clusters as they give phonons path to transfer fast. To verify this hypothesis, we studied the cluster size of cobalt nanofluid using Dynamic Light Scattering (DLS) technique (Malvern Zeta sizer). We found that with increasing pH of the nanofluids the average particle size increases as shown in figure 4.16.

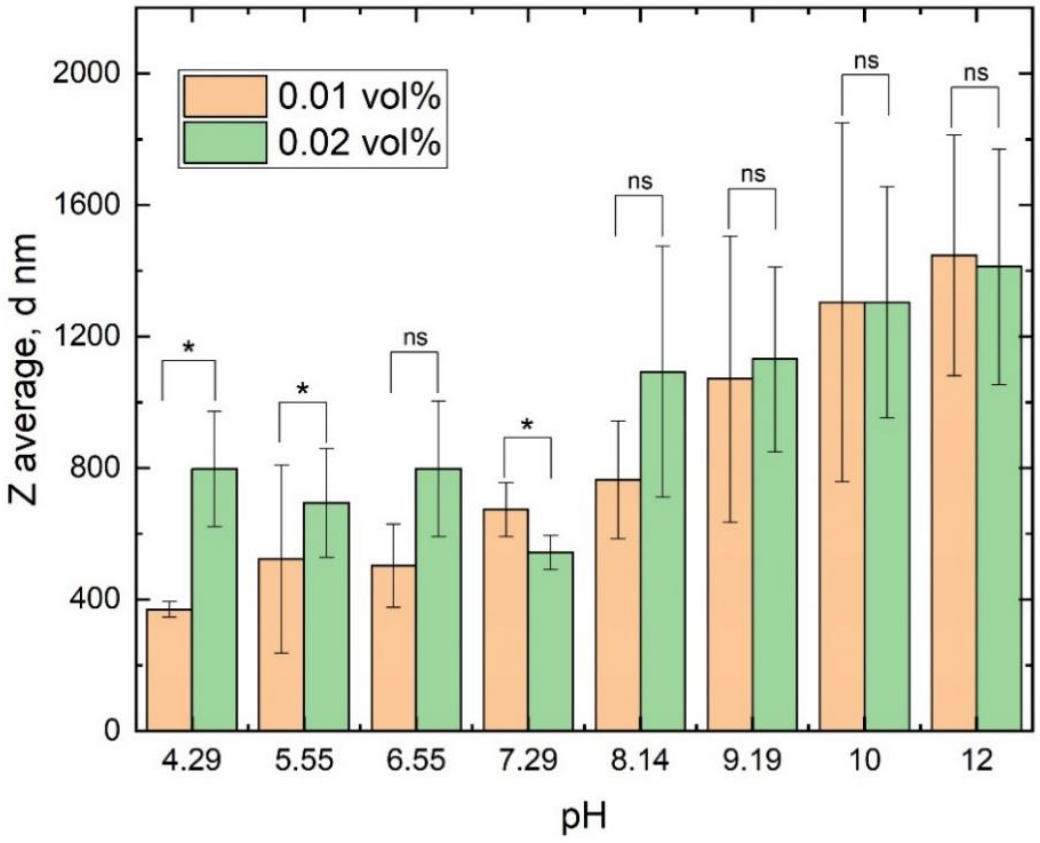

Figure 4.16. Average Cluster Size at Different pH Values. Significance level is also shown (* = significant ($p<0.05$), ns= not significant)

According to the argument presented before, higher cluster size should increase the thermal conductivity of nanofluid which we did not see in our case. We found that thermal conductivity is affected positively by particle volume fraction as with the increase of particle concentration by only 0.01vol%, the thermal conductivity of nanofluid increased by 3.2% to 4.3% for varying pH. Z average was taken from 9 data set for each pH. We can see that the cluster size increases with pH mostly. However, for 0.01 vol%, the cluster size is lower than 0.02 vol%. The logical explanation is that, for higher nanowire concentration, the possibility of particle clustering is more which increases the cluster size also. However, we can see a big deviation for our cluster size data. This can be accounted for the way DLS measures the size of the particle/cluster. DLS method considers particles as spheres and cluster size is calculated based on this assumption. However, our added nanoparticles are not spherical rather have 1-D shape which can affect the cluster size calculation using this technique.

Figure 4.17 shows the correlation between cluster size and the effective thermal conductivity of nanofluid. We do not see any specific correlation between cluster size and nanofluid thermal conductivity. We can see that irrespective of the cluster size, nanofluids with higher particle concentration yields a higher value for thermal conductivity. On the other hand, even for the same cluster size of ≈800 nm, nanofluids show different thermal conductivity values (0.66 W/m.K for 0.01 vol %, 0.685 W/m.K and 0.693 W/m.K for 0.02 vol %).

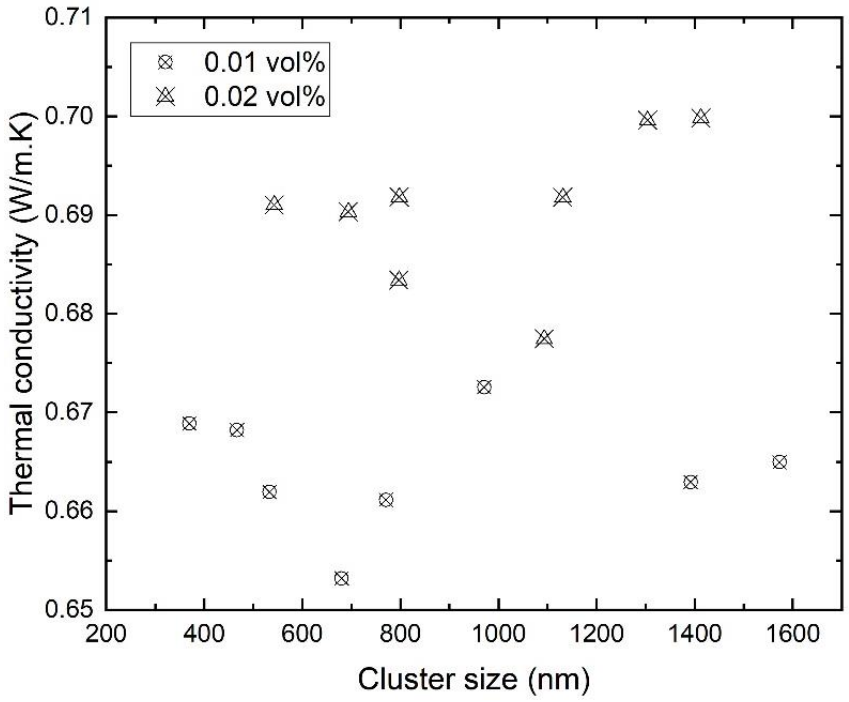

Figure 4.17. Thermal Conductivity of Nanofluids for Different Cluster Size

4.9 Conclusion

This chapter focused on the preparation of cobalt nanowire modified nanofluids and their thermal conductivity study. A definite route was developed to create stable aqueous nanofluid via surface modification of nanowires with oleic acid at high temperatures. Results show that oleic acid is physically adsorbed onto the surface of nanowires and give electrostatic stabilization by inducing surface charge. Zeta potential analysis shows that the surface modified nanowires give high absolute value of zeta potential at various pH values which indicates the stability of prepared nanofluid. Two different concentrations of 0.01 vol% and 0.02 vol% nanofluids were used for the thermal conductivity measurement. Thermal conductivity was measured using TPS technique. It

was found that pH does not affect the thermal conductivity of water. Results also show that nanowire based nanofluid has higher thermal conductivity compared to the base fluid. 0.01 vol% nanofluid increases the effective thermal conductivity up to 8.5% if compared to DI water. We also found that volume concentration can affect the effective thermal conductivity of nanofluid as the 0.02 vol% nanofluid increased the effective thermal conductivity up to 14% compared to the base fluid.

A correlation study using empirical formula for thermal conductivity and acquired experimental data was also performed. It was found that Hamilton-Crosser model can predict the thermal conductivity of Co nanowire modified nanofluid fairly irrespective of the volume concentration when compared to the Maxwell model. However, the prediction by the Maxwell model underpredicts thermal conductivity by 6% at higher volume concentration while for the Hamilton-Crosser model, it is only 0.7%. We can conclude from our findings that the Hamilton-Crosser model is suitable to predict thermal conductivity of Co nanowire based nanofluid especially if the concentration of added nanoparticle is higher.

We also studied the possible mechanism for the abnormal increase in thermal conductivity with a different cluster size of nanoparticle. We found that solution pH has a strong effect on particle cluster size though we did not find any significant effect of cluster size on the increase of thermal conductivity of nanofluid.

Increased thermal conductivity of nanofluid can offer to be a suitable option where highly efficient heat transfer media is needed. However, we need to further investigate the efficiency of cobalt nanowire based nanofluid for application purposes. In

the next chapter, we will study to understand the efficacy of Co-nanowire modified nanofluid as cooling media using a simple counter-flow microfluidic heat exchanger.

CHAPTER V

APPLICATION OF COBALT NANOWIRE MODIFIED NANOFLUID AS AN EFFECTIVE HEAT TRANSFER MEDIUM: A DEMONSTRATION

5.1 Introduction

As metal nanofluid shows improved thermal properties which can, in turn, increase the efficiency of thermal transport, they can be used in industries for cooling various thermal management purposes i.e. computer, car radiator, other electronics devices, and industrial machinery. Several researchers have investigated the heat transfer efficacy with various nanofluids used with a heat exchanger setup. Heat exchanger plays an important role in energy conservation and recovery. With the advancement of technology and the continuous need for highly efficient equipment, micro-scale devices commonly known as MEMS can be beneficial. However, reduced channel dimensions induce high pressure drop and the amount of transferred heat is mainly limited by the properties of heat transfer fluids. As the heat transfer rate depends on the surface area to volume ratio, smaller flow channels give a higher heat transfer coefficient. Additionally, with the increase in thermal conductivity of heat transfer fluids, it is possible to achieve higher efficiency. In this chapter, we will demonstrate the application of nanomodified fluid in a simple counter-flow heat exchanger and investigate their efficiency. Pantzali et al.[182] studied the effect of water based CuO nanofluid on the performance of miniature plate heat exchanger with a modulated surface. They found that heat capacity decreases

significantly with the increase in thermal conductivity. They also found that the enhancement of heat transfer is more at a lower flow rate. They also reported that volumetric flow rate is three times lower. Mapa and his co-workers studied the effect of nanofluid in a mini heat exchanger and found that the presence of nanoparticles can reduce the thickness of thermal boundary layer increasing the heat transfer rate[183]. Water based Al_2O_3 and TiO_2 were used in a shell and tube heat exchanger under turbulent flow condition by Farajollahi et al.[184]. Trisaksri et al.[143] studied on silicon microchannel heat sink using water based CuO and Al_2O_3 and found that there is no extra pressure drop due to the presence of nanoparticles. However, Chein et al.[185] found a small increase in pressure drop due to nanofluid while studying the performance of heat sink using water based Cu nanofluid. They also found that nanofluids can absorb more heat at low flow rate. A 10% increase in heat transfer was reported by Jang et al.[186] using water based diamond nanofluid. More works on the effect of nanofluids in heat exchangers can be found elsewhere[187].

5.2 Methodology

5.2.1 Experimental Setup

A microfluidic heat exchanger set up was developed using Luer μ-slide (acquired from Ibidi®) with a 0.4 mm channel height. Using a UV curable adhesive (Bondic®) a glass slide was attached to the channel side of the μ-slide using UV light for a few

seconds. Another μ-slide was attached on the bottom of the glass slide upside down to create the desired heat exchanger chip as shown in figure 5.1(a).

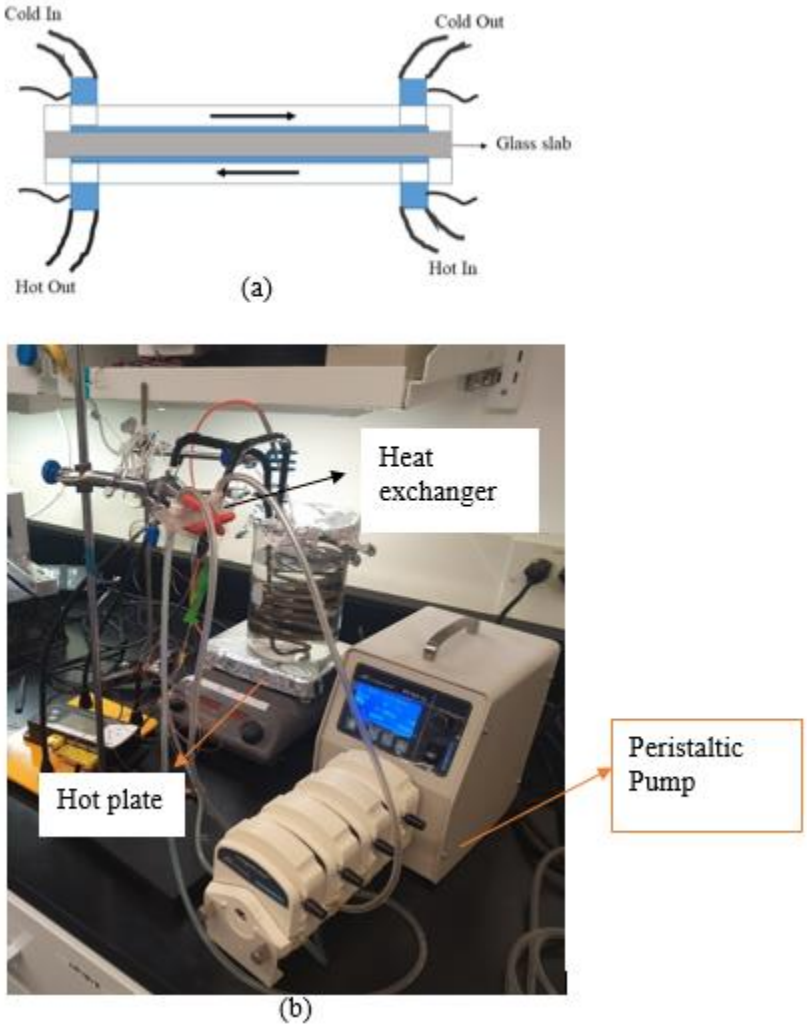

Figure 5.1. Heat Transfer Setup; (a) Fabricated Heat Exchanger, (b) Microfluidic Experimental Configuration

Thermocouples (measuring accuracy 0.1 ^{0}C) were inserted in each inlet and outlet of this chip and an Omega 2000 data logger was used to measure the temperature reading during the experiment. A peristaltic pump (Longer) was used to maintain the flow rate at

472.7 μL/min. A hot plate was used to supply heated water (as a heat source) through a copper pipe to the hot end of the chip. On the cold end side, DI water or modified nanofluid was fed in to create a counter flow type heat exchanger. Using proper software, temperature reading was taken for 30 minutes for further calculation.

5.2.2 Setting up the Numerical Problem

The numerical domain for the microfluidic heat exchanger is modeled in COMSOL Multiphysics 5.3 as shown in figure 5.2. The dimension of the chip apparatus is 50×25.5×6 mm (Length × Width × thickness) similar to the physical dimension of our microfluidic heat exchanger. The hot and cold carrying micro-channel dimensions are 50×5×0.4 mm (Length × Width × thickness). The top channel was assigned for hot fluid (working as a heat source) and the bottom channel was assigned for cooling fluids. Heat is transferred between fluids through glass slab separating them. Some key assumptions were made on the operating conditions for the heat exchanger such as

1. The heat exchanger operates under steady-state condition
2. Operating fluids remain as single phase along the channel and flow is laminar
3. External heat transfer effects are neglected
4. The outer walls of the heat exchanger are insulated (adiabatic condition)

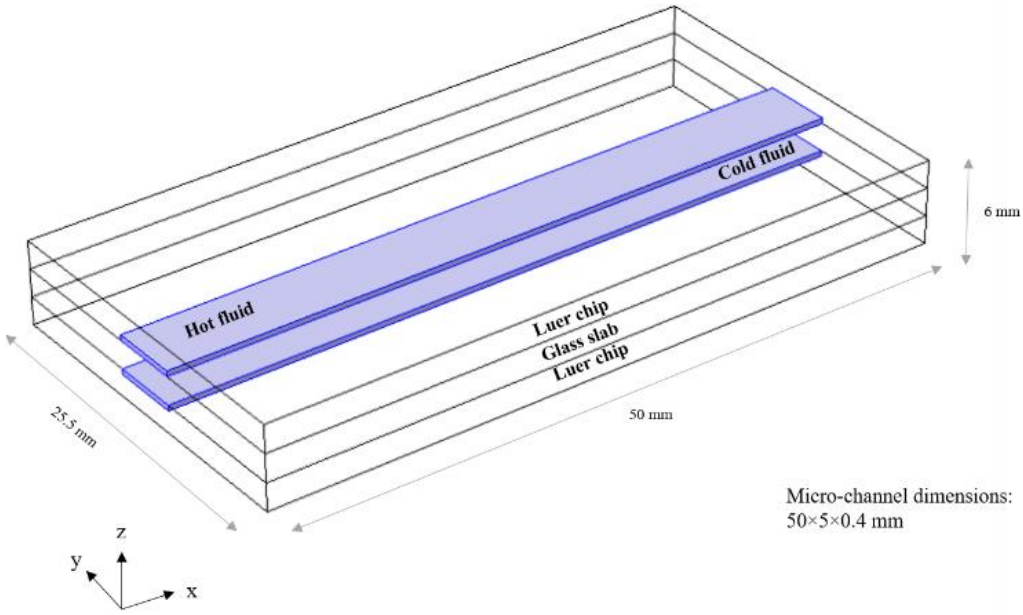

Figure 5.2. Schematic of Domain for Numerical Simulation of Micro Heat Exchanger

The governing equations for mass, momentum, and energy conservation of the fluids for laminar incompressible flow are as follows:

Mass conservation

$$\frac{\partial u}{\partial x}+\frac{\partial v}{\partial y}+\frac{\partial w}{\partial z}=0 \tag{5.1}$$

Momentum conservation

X-momentum:

$$\rho_f\left(u\frac{\partial u}{\partial x}+v\frac{\partial u}{\partial y}+w\frac{\partial u}{\partial z}\right)=-\frac{\partial p}{\partial x}+\mu_f\left(\frac{\partial^2 u}{\partial x^2}+\frac{\partial^2 u}{\partial y^2}+\frac{\partial^2 u}{\partial z^2}\right) \tag{5.2}$$

Y-momentum:

$$\rho_f \left(u\frac{\partial v}{\partial x} + v\frac{\partial v}{\partial y} + w\frac{\partial v}{\partial z}\right) = -\frac{\partial p}{\partial y} + \mu_f\left(\frac{\partial^2 v}{\partial x^2} + \frac{\partial^2 v}{\partial y^2} + \frac{\partial^2 v}{\partial z^2}\right) \quad (5.3)$$

Z-momentum:

$$\rho_f \left(u\frac{\partial w}{\partial x} + v\frac{\partial w}{\partial y} + w\frac{\partial w}{\partial z}\right) = -\frac{\partial p}{\partial z} + \mu_f\left(\frac{\partial^2 w}{\partial x^2} + \frac{\partial^2 w}{\partial y^2} + \frac{\partial^2 w}{\partial z^2}\right) \quad (5.4)$$

Where, u,v,w means velocity components in x,y, and z-direction respectively for fluid region, ρ_f and μ_f are the density and viscosity of the fluid region respectively, and p is the operating fluid pressure.

Energy conservation

For fluid region:

$$u\frac{\partial T_f}{\partial x} + v\frac{\partial T_f}{\partial y} + w\frac{\partial T_f}{\partial z} = \frac{k_f}{\rho_f c_{pf}}\left(\frac{\partial^2 T_f}{\partial x^2} + \frac{\partial^2 T_f}{\partial y^2} + \frac{\partial^2 T_f}{\partial z^2}\right) \quad (5.5)$$

Where, T_f and c_{pf} are temperature of the fluid and specific heat respectively

For solid region:

$$k_s\left(\frac{\partial^2 T_s}{\partial x^2} + \frac{\partial^2 T_s}{\partial y^2} + \frac{\partial^2 T_s}{\partial z^2}\right) = 0 \quad (5.6)$$

Where, T_s and k_s are temperature for solid region and thermal conductivity of solid

These governing equations were solved using following boundary conditions

1) For micro-channels:

   Hot fluid: - channel inlet at x=0,

   u= u_avg, v=w=0 and T_f= hot inlet temperature,

   Channel outlet at x=50 mm with pressure = atmospheric pressure

   Cold fluid: - channel inlet at x=50 mm,

   u= -u_avg, v=w=0 and T_f= cold inlet temperature,

   Channel outlet at x=0 with pressure = atmospheric pressure

2) At the solid-fluid interface:

   u=v=w=0 and$-k_s \frac{\partial T_s}{\partial n} = -k_f \frac{\partial T_f}{\partial n}$, where 'n' is the coordinate normal to the wall

3) At outer walls:

   Upper and lower walls: external natural convection for horizontal plates with ambient temperature and air as external fluid at atmospheric pressure.

   Sidewalls: external natural convection for vertical walls with ambient temperature and air as external fluid at atmospheric pressure.

The COMSOL multiphysics 5.3 software was used for generating the mesh and solving these governing equations. Figure 5.3 shows the mesh structure with 474527 elements generated using physics controlled finer mesh. Few cases were studied with coarse, normal, fine, and finer meshes as grid dependence analysis. The numerical simulation is performed for steady-state conditions depicting the experimental conditions with the above mentioned assumptions. For validation of the model, a simple case is studied with water as hot and cold fluid. The inlet temperature for hot and cold fluid is

307.16 K and 296.32 K respectively. The inlet velocities for both the channels are obtained by converting volumetric flow rate (472.7 µL/min) to the average velocity at the channel inlet face (4 mm/s). The rest of the boundary conditions were same as mentioned above.

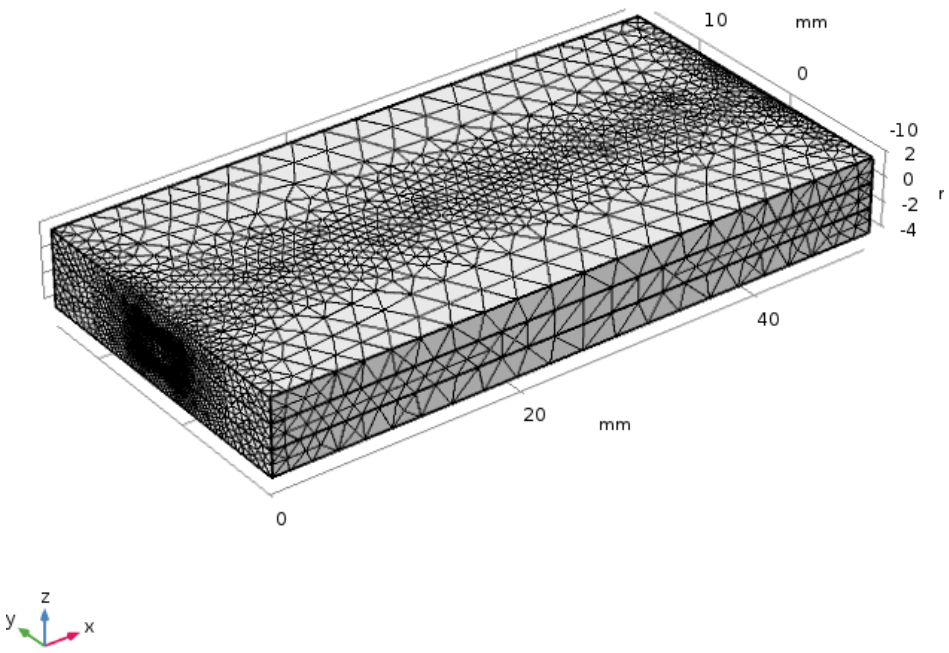

Figure 5.3. The Computational Domain with Mesh (Finer Physics Control Mesh in COMSOL)

Figure 5.4 shows the surface temperature distribution, temperature distribution in the section view (x-z plane) of the microchannel in the domain.

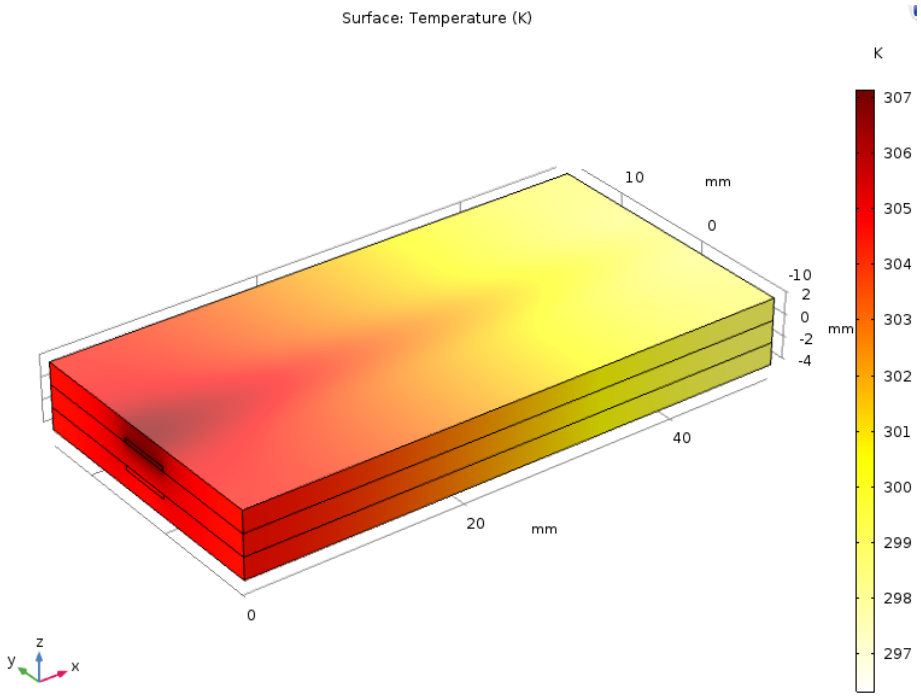

Figure 5.4. Surface Temperature Distribution for the Domain

5.3 Results and Discussions

From our experimental setup, we measured the temperature value of hot inlet and hot outlet and the temperature of the cold inlet and cold outlet at a fixed volumetric flow rate ($\dot{v}$). Overall heat transfer coefficient, is calculated using the following formula (equation 5.7)

$$Q = h\ A\ (\Delta T_m) \tag{5.7}$$

Where, ΔT_m = Logarithmic mean temperature difference (K)

h = Overall Heat transfer coefficient (W/m^2K)

Q = Heat transfer rate (W)

Logarithmic Mean Temperature Difference (LMTD) is calculated for the counter flow to determine the temperature difference between heat exchanger wall and heat transfer fluid and is a well-defined parameter for heat exchanger efficiency determination[188]. LMTD is calculated using the following formula (equation 5.8)

$$\text{LMTD}= \frac{\Delta t_i - \Delta t_o}{\ln(\frac{\Delta t_i}{\Delta t_o})} = \frac{\Delta_1 - \Delta_2}{\ln(\frac{\Delta_1}{\Delta_2})} \quad (5.8)$$

Here, Δt_i = temperature difference of inlet primary and outlet secondary fluid = Δ_1

and Δt_o = temperature difference of outlet primary and inlet secondary fluid = Δ_2

For a 100% efficient heat exchanger where all the heat lost by the hot medium is collected by cold medium, the LMTD value becomes infinity while zero LMTD value means there is no heat flow. Heat transfer rate Q is calculated using the formula (equation 5.9)

$$Q = \dot{m}\ c_p\ \Delta T \quad (5.9)$$

Here, ΔT = temperature difference between hot inlet and outlet or cold inlet and outlet

c_p = specific heat capacity of fluid (J/kgK)

Mass flow rate, $\dot{m}$ is calculated by the following formula (equation 5.10)

$$\dot{m} = \dot{v}\ \rho_f \quad (5.10)$$

Here ρ_f = density of fluid.

Specific heat capacity of nanofluid was calculated by equation (5.11)

$$C_{p(nanofluid)} = \frac{\varphi\, \rho_{np}\, c_{p\,np} + (1-\varphi)\rho_{bf}\, c_{p\,bf}}{\rho_{nf}} \quad (5.11)$$

Here, np, bf, and nf means nanoparticles, base fluid, and nanofluid, respectively. and φ is volume fraction.

Reynolds number (Re) was calculated to find out whether the flow is laminar or turbulent according to the following formula (equation 5.12)

$$Re = \frac{Q\, D_H}{\nu\, A} \quad (5.12)$$

Here, Q is volumetric flow rate, ν is kinematic viscosity (for water at 25^0C: 8.917×10^{-7} m^2/s), A is cross-sectional area of fluid channel and D_H is hydraulic diameter. As Ibidi luer flow channel has rectangular cross-section, the expression for D_H is (equation 5.13)

$$D_H = \frac{4\, A}{P} \quad (5.13)$$

Where, P is wetting parameter. For a flow to be laminar, the Re number should be less than 2,300 and for turbulent flow it should be greater than 2,900. Using these formulas we got the Re number to be 3.23 which falls in the laminar flow region.

Figure 5.5 shows a typical temperature profile for DI water used as cooling medium.

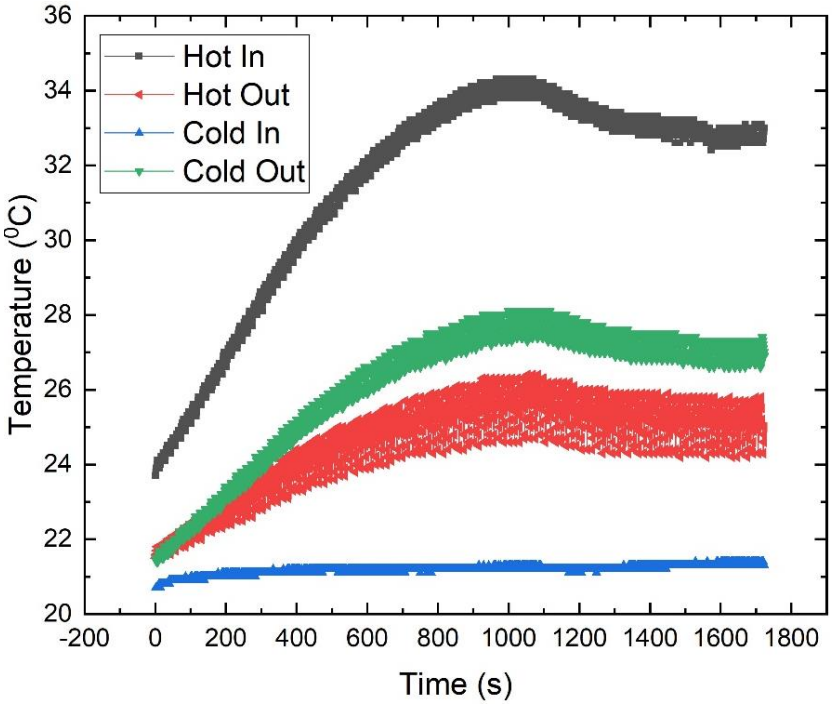

Figure 5.5. Typical Temperature Profile for DI Water

All the calculation was done after the system came to steady-state (temperature plateau) and at least for 3 times.

From the simulation results, it was found that the hot and cold outlet temperatures are 298.6 K and 304.85 K respectively. The experimental hot and cold outlet temperature values are 299.9 K and 300.5 respectively with relative errors 5% and 14.5%. These errors are considerable when compared to the errors reported in the literature[189]. The temperature profile in the flow channel is shown in figure 5.6.

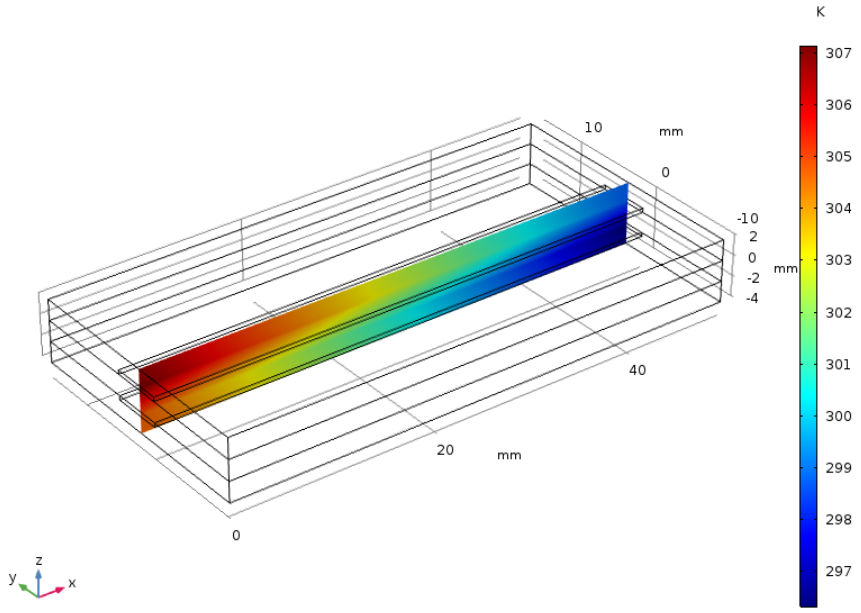

Figure 5.6. Temperature Distribution in the x-z Section (for Temperature Variation in the Micro-channels)

LMTD calculation for the experiments for DI water is shown in table 5.1. A similar calculation was done for nanofluids also and the results are shown in figure 5.7.

Table 5.1 LMTD Calculation for DI Water

Cooling Fluid	**Hot 1 (^{0}C)**	**Cold 2 (^{0}C)**	**Δ_1= Hot 1-Cold2**	**Hot 2 (^{0}C)**	**Cold 1 (^{0}C)**	**Δ_2= Hot 2-Cold 1**	**LMTD**
DI water	33.244	27.206	6.039	25.310	21.267	4.043	4.978

From figure 5.7 we can see that LMTD increases for nanofluids compared to the base fluid. Additionally, we found a higher LMTD value for higher concentration of nanofluid. Higher LMTD means more heat is extracted from the system as it is proportional to heat transfer rate. It also means that heat exchangers can perform at the same level even if the area of the heat exchanger is reduced.

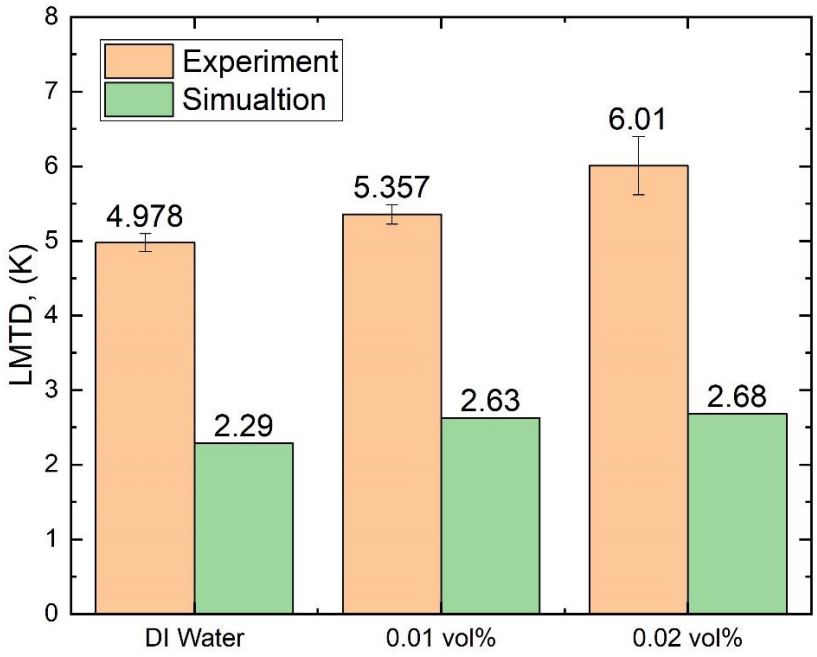

Figure 5.7. LMTD Values for Different Cooling Fluids for Both Experiments and Simulations

From the numerical analysis, the calculated LMTD shows lower values compared to experiments though a similar trend in the increase in LMTD value was observed. In the simulation, a continuous flow of fluid was considered and tubings for circulation are not considered, whereas in experiments the coolants were circulated in a closed-loop which might affect the temperature distribution, and hence LMTD.

However, only LMTD value comparison is not enough to define the heat exchanger performance as the coolants were changed. That is why comparison of overall heat transfer coefficients for all these coolants should be considered to get a better understanding of the efficiency of nanofluid used as a coolant. Figure 5.8 shows the increment of the effective heat transfer coefficient compared to base fluid for different particle volume fractions.

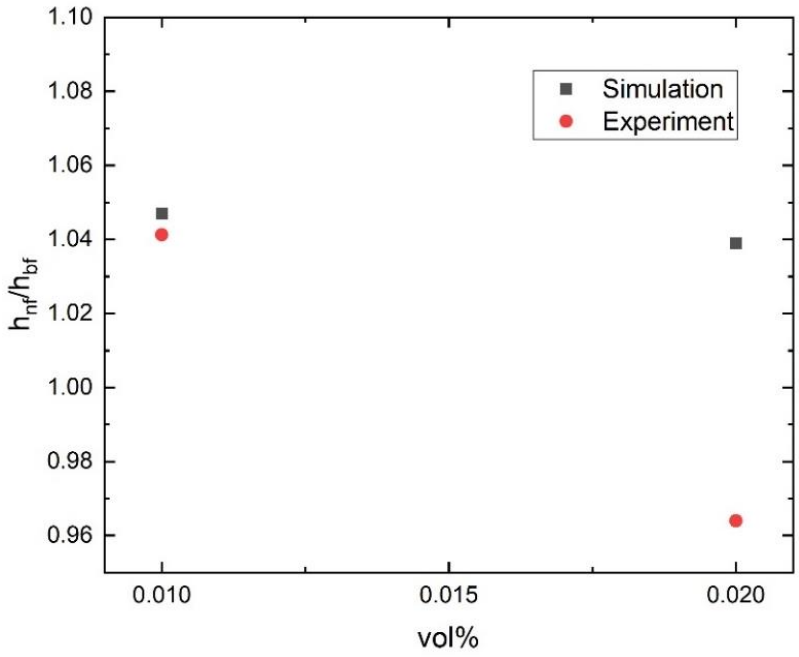

Figure 5.8. Increment in Effective Heat Transfer Coefficient at Different Particle Concentration

Results from both numerical analysis and experiments are shown in the figure. For 0.01vol% nanofluid, we can see a 4.1% increase in effective heat transfer coefficient when compared to the base fluid. From our numerical analysis calculation, we got slightly higher value as the increment is 4.9-5%. However, for 0.02 vol%, we see an overall decrease in heat transfer coefficient value from our experiments. Lack of information on particle-particle interaction at higher concentration, particle behavior at flow condition and under temperature gradient, etc. can potentially account for this deviation. From the numerical analysis, we also see the ratio of effective heat transfer coefficient decreased slightly for 0.02 vol% nanofluid though it shows a 4.1% increase if compared to the base fluid. So, from both simulation and experiments we can see the heat

transfer coefficient ratio decreases for 0.02 vol% nanofluid comparing with 0.01 vol% nanofluid.

5.4 Conclusion

Energy conservation thus in turn cost saving is one of the main challenges for industries to increase efficiency. Nanofluids, because of their superior heat transfer properties can be used successfully in heat exchangers to save energy. In this chapter, we have shown a demonstration of cobalt nanowire based nanofluid for heat exchanger application. We found that, if nanofluid is used as cooling media in place of pure water, the heat transfer properties increases. Higher LMTD value for nanofluids proves that the heat exchangers can perform with the same efficiency for smaller heat exchangers. Comparison of overall heat transfer coefficient with base fluid shows that nanofluids can increase the heat transfer coefficient by 4.1-5% for 0.01 vol% and 0.02 vol% respectively which in turn accounts for better heat exchanger performance. However, more carefully designed experiments can minimize the difference in experimental and simulation results.

CHAPTER VI

CONCLUSION AND FUTURE SCOPE

Present research has focused on the effect of current density and bath temperature on the morphological and structural properties of Co nanowire following template assisted electrodeposition method. Three different current densities of 3, 5, and 7 $mA.cm^{-2}$ and bath temperature RT (25 ^{0}C), 40 ^{0}C and 50 ^{0}C were used while other parameters were kept constant. Synthesized nanowires then were analyzed to study the influence of these processing parameters on nanowire morphology, length of nanowires, mass produced at each run, crystal orientation, crystal size, crystallographic study, and growth model identification. A facile route to prepare cobalt nanowire based nanofluid was also developed in aqueous media for two different volume fractions 0.01% and 0.02% and thermal conductivity of these new nanofluids was studied. Finally, the efficacy of the nanofluid was tested in a lab-scale microfluidic heat exchanger set up.

Co nanowires were successfully prepared via template-assisted electrodeposition method using AAO with consistency and repeatability. The nanowire diameter was found to be 230-280 nm based on the actual diameter of the nanopores whereas the length varies from 18-24 μm. We found that operating conditions can affect the nanowire physical properties as the surface morphology is changed with them. Surface roughness increases with the increase of current density and temperature. Nanowire length and mass

produced at each run are also affected as 40 ^{0}C bath temperature and 5-7 mA.cm^{-2} conditions give suitable results. The nanowires are as pure as 96.97% of Co with only trace oxygen was also found.

Co nanowires were showed polycrystalline nature with different preferential orientation of crystal planes at different processing conditions. XRD spectra detected the sharp peaks for (100), (002), (110), (101), and (112) planes. However, at high bath temperature (103) plane was also detected. Average crystal sizes are 22- 40 nm and with the change in processing conditions crystal size changes. Although there is no clear correlation between the crystal size and processing conditions, it was found that with increasing temperature, the average crystal size increases for these planes in general. HRTEM analysis and SAED pattern show that the nanowires show single-crystalline zones though there is a polycrystalline region at the bottom of the nanowires as those are the nucleation sites for nanowire growth. 2D crystal growth mechanism is proposed for the nanowire growth where both layer-by-layer growth and tilted plane growth are possible.

A successful route of cobalt nanowire based nanofluid preparation was developed by the surface treatment process via electrostatic stabilization process. The nanofluids show good stability over time. With the help of FTIR analysis, we can see that there is no major shift rather the oleic acid atoms are physically adsorbed on the surface of nanowire, which gives better stabilization in aqueous media. Thermal conductivity analysis shows that the nanofluid thermal conductivity is increased from 8 to 14% compared to the base fluid at 0.01 vol% and 0.02 vol% nanofluid respectively. The

correlation between theoretical models of thermal conductivity and experimental results reveals that the nanofluid thermal conductivity can be better predicted with the Hamilton-Crosser model rather than the Maxwell model. Microfluidic heat exchanger analysis shows that the nanofluids are more efficient in removing heat from systems compared to DI water. The thermal conductivity measurement was done at a set temperature of 21 ^{0}C which is not the ideal case in applications. Special cells with controllable temperature ramping can reveal the behavior of cobalt nanowire based nanofluid at high temperatures.

Logarithmic mean temperature difference increased for both 0.01 vol% and 0.02 vol% nanofluid compared to DI water which indicates better heat exchanger performance. An increase in overall heat transfer coefficient for 0.01 vol% nanofluid shows the efficiency of the heat exchanger is improved. However, for higher concentration, we cannot say that for sure from our present experimental findings, though from our numerical analysis of a simplified configuration we can see the heat transfer coefficient increased for 0.02 vol% nanofluid. Further investigation can be performed at different temperatures to determine the thermal properties of nanofluid as in practical case the operating temperature for cooling fluids is higher than room temperature. However, current experiments were done in an open environment at an ambient temperature of 21-22 ^{0}C, and heat loss due to radiation was not controlled. Besides, the UV curable polymer was not durable enough to run several experiments continuously. We found water leakage after few runs, especially from the hot side. More carefully designed experiments in a controlled environment can give verifiable results which can be a great future scope.

Besides physical and thermal properties of nanowires, mechanical properties can also be studied to understand the structural strength and integrity under tension which is an important feature for many applications i.e. electrical interconnect, MEMS devices, or flexible electronic devices. However, the experimental studies for nanowire mechanical properties is a challenging task as the experiments are needed to be done in controlled microscopic environment and are limited by the resolution of imaging techniques. Nanowire deformation behavior is characterized by atomistic level changes at nanoscale which is not possible to capture by experimental methods. Molecular dynamics (MD) simulations have enabled understanding of mechanical properties, deformation, and failure behavior in detail, as it would allow for visual observation and tracking of molecular configuration. We have studied the failure behavior of Co nanowire under uniaxial tension via MD simulations using Large-scale atomic/molecular massively parallel simulator (LAMMPS) which can lead to the future study of other pure metal nanowires as well as hybrid nanowires. The study is presented in appendix A [14].

REFERENCES

[1] C. R. Martin, “Membrane-Based Synthesis of Nanomaterials,” *Chem. Mater.*, vol. 8, pp. 1739–1746, 1996, doi: 10.1021/CM960166S.

[2] M. Samykano, R. Mohan, and S. Aravamudhan, “Morphology and Crystallographic Characterization of Nickel Nanowires—Influence of Magnetic Field and Current Density During Synthesis,” *J. Nanotechnol. Eng. Med.*, vol. 5, no. 2, Aug. 2014, doi: 10.1115/1.4028026.

[3] H. Pan *et al.*, “Growth of Single-Crystalline Ni and Co Nanowires via Electrochemical Deposition and Their Magnetic Properties,” *J. Phys. Chem. B*, vol. 109, pp. 3094–3098, 2005, doi: 10.1021/JP0451997.

[4] B. Gates, Y. Wu, Y. Yin, P. Yang, and Y. Xia, “Single-Crystalline Nanowires of Ag $_2$ Se Can Be Synthesized by Templating against Nanowires of Trigonal Se,” *J. Am. Chem. Soc.*, vol. 123, no. 46, pp. 11500–11501, Nov. 2001, doi: 10.1021/ja0166895.

[5] H. Pan *et al.*, “Growth of Single-Crystalline Ni and Co Nanowires via Electrochemical Deposition and Their Magnetic Properties,” *J. Phys. Chem. B*, vol. 109, no. 8, pp. 3094–3098, 2005, doi: 10.1021/JP0451997.

[6] K. Ahuja and A. Rawat, “Heat Transfer Fluid Market Size – Industry Share Forecast Report 2024,” 2017. Accessed: Feb. 25, 2020. [Online]. Available: https://www.gminsights.com/industry-analysis/heat-transfer-fluid-market?utm_source=GoogleAds&utm_medium=Adwords&utm_campaign=Chemicals-PPC&gclid=EAIaIQobChMIk-Xk5vDt5wIVDZyzCh3BoQFlEAAYAyAAEgKhAfD_BwE.

[7] G. Xia, H. Jiang, R. Liu, and Y. Zhai, “Effects of surfactant on the stability and thermal conductivity of Al 2O3/de-ionized water nanofluids,” *Int. J. Therm. Sci.*, vol. 84, pp. 118–124, Oct. 2014, doi: 10.1016/j.ijthermalsci.2014.05.004.

[8] A. Ghadimi and I. H. Metselaar, “The influence of surfactant and ultrasonic processing on improvement of stability, thermal conductivity and viscosity of titania nanofluid,” *Exp. Therm. Fluid Sci.*, vol. 51, pp. 1–9, Nov. 2013, doi: 10.1016/j.expthermflusci.2013.06.001.

[9] X. Li, Y. Chen, S. Mo, L. Jia, and X. Shao, “Effect of surface modification on the stability and thermal conductivity of water-based SiO2-coated graphene nanofluid,” *Thermochim. Acta*, vol. 595, pp. 6–10, Nov. 2014, doi: 10.1016/j.tca.2014.09.006.

[10] E. J. Lee, M. H. Chang, Y. S. Kim, and J. Y. Kim, “High-pressure polyol synthesis of ultrathin silver nanowires: Electrical and optical properties,” *APL Mater.*, vol. 1, no. 4, p. 042118, Oct. 2013, doi: 10.1063/1.4826154.

[11] A. I. Shiave, R. Mohan, and M. Samykano, “Effect of Current Density and Temperature on Template Assisted Cobalt Nanowire,” in *ASME 2019 International Mechanical Engineering Congress and Exposition*, Nov. 2019, doi: 10.1115/IMECE2019-11673.

[12] G. Schider *et al.*, “Optical properties of Ag and Au nanowire gratings,” *J. Appl. Phys.*, vol. 90, no. 8, pp. 3825–3830, Oct. 2001, doi: 10.1063/1.1404425.

[13] L. Sun, Y. Hao, C. L. Chien, P. C. Searson, and P. C. Searson, “Tuning the properties of magnetic nanowires,” *IBM J. Res. Dev.*, vol. 49, no. 1, pp. 79–102, 2005, doi: 10.1147/rd.491.0079.

[14] A. I. Shiave, R. P. S. Tomar, I. P. Espinosa, and R. Mohan, “Deformation Mechanisms and Dislocations in Nickel–Cobalt Core–Shell Nanowires Under Uniaxial Tensile Loading—A Molecular Dynamics Modeling Analysis,” *Adv. Sci. Eng. Med.*, vol. 11, no. 12, pp. 1187–1201, Dec. 2019, doi: 10.1166/asem.2019.2478.

[15] G. M. Moldoveanu, G. Huminic, A. A. Minea, and A. Huminic, “Experimental study on thermal conductivity of stabilized Al2O3 and SiO2 nanofluids and their hybrid,” *Int. J. Heat Mass Transf.*, vol. 127, pp. 450–457, Dec. 2018, doi: 10.1016/J.IJHEATMASSTRANSFER.2018.07.024.

[16] K. Sinha, B. Kavlicoglu, Y. Liu, F. Gordaninejad, and O. A. Graeve, “A comparative study of thermal behavior of iron and copper nanofluids,” *J. Appl. Phys.*, vol. 106, no. 6, 2009, doi: 10.1063/1.3225574.

[17] M. Hemmat Esfe, S. Saedodin, S. Wongwises, and D. Toghraie, “An experimental study on the effect of diameter on thermal conductivity and dynamic viscosity of Fe/water nanofluids,” *J. Therm. Anal. Calorim.*, vol. 119, no. 3, pp. 1817–1824, 2015, doi: 10.1007/s10973-014-4328-8.

[18] H. Adhikari, P. C. McIntyre, A. F. Marshall, and C. E. D. Chidsey, “Conditions for subeutectic growth of Ge nanowires by the vapor-liquid-solid mechanism,” *J. Appl. Phys.*, vol. 102, no. 9, p. 094311, Nov. 2007, doi: 10.1063/1.2803893.

[19] J. . Liu, S. . Cai, G. . Jin, S. . Thomas, and K. . Wang, “Growth of Si whiskers on Au/Si(1 1 1) substrate by gas source molecular beam epitaxy (MBE),” *J. Cryst. Growth*, vol. 200, no. 1–2, pp. 106–111, Apr. 1999, doi: 10.1016/S0022-0248(98)01408-0.

[20] M. Morassi *et al.*, “Morphology Tailoring and Growth Mechanism of Indium-Rich InGaN/GaN Axial Nanowire Heterostructures by Plasma-Assisted Molecular Beam Epitaxy,” *Cryst. Growth Des.*, vol. 18, no. 4, pp. 2545–2554, Apr. 2018, doi: 10.1021/acs.cgd.8b00150.

[21] H. Chandrasekaran, G. Sumanasekara, and M. K. Sunkara, “Rationalization of nanowire synthesis using low-melting point metals,” *J. Phys. Chem. B*, vol. 110, no. 37, pp. 18351–18357, 2006, Accessed: Sep. 19, 2018. [Online]. Available: https://pubs.acs.org/doi/abs/10.1021/jp0639750.

[22] H. Yu and W. E. Buhro, “Solution–Liquid–Solid Growth of Soluble GaAs Nanowires,” *Adv. Mater.*, vol. 15, no. 5, pp. 416–419, Mar. 2003, doi: 10.1002/adma.200390096.

[23] C.-Y. Wen, M. C. Reuter, J. Tersoff, E. A. Stach, and F. M. Ross, “Structure, Growth Kinetics, and Ledge Flow during Vapor−Solid−Solid Growth of Copper-Catalyzed Silicon Nanowires,” *Nano Lett.*, vol. 10, no. 2, pp. 514–519, 2009, doi: 10.1021/NL903362Y.

[24] C. Qian, F. Kim, L. Ma, F. Tsui, P. Yang, and J. Liu, “Solution-Phase Synthesis of Single-Crystalline Iron Phosphide Nanorods/Nanowires,” *J. Am. Chem. Scociety*, vol. 15, no. 2, pp. 933–939, 2003, doi: 10.1021/ja038401c.

[25] Byron Gates, A. Yadong Yin, and Y. Xia, “A Solution-Phase Approach to the Synthesis of Uniform Nanowires of Crystalline Selenium with Lateral Dimensions in the Range of 10−30 nm,” *J. Am. Chem. Scociety*, vol. 122, no. 50, pp. 12582–12583, 2000, doi: 10.1021/JA002608D.

[26] N. R. Jana, L. Gearhart, and C. J. Murphy, “Wet Chemical Synthesis of High Aspect Ratio Cylindrical Gold Nanorods,” *J. Phys. Chem. B*, vol. 105, no. 19, pp. 4065–4067, 2001, doi: 10.1021/JP0107964.

[27] D. Zhang, S. W. Eaton, Y. Yu, L. Dou, and P. Yang, “Solution-Phase Synthesis of Cesium Lead Halide Perovskite Nanowires,” *J. Am. Chem. Soc.*, vol. 137, no. 29, pp. 9230–9233, Jul. 2015, doi: 10.1021/jacs.5b05404.

[28] T. Bayrak *et al.*, “DNA-Mold Templated Assembly of Conductive Gold Nanowires,” *Nano Lett.*, vol. 18, no. 3, pp. 2116–2123, Mar. 2018, doi: 10.1021/acs.nanolett.8b00344.

[29] M. Knez *et al.*, “Biotemplate synthesis of 3-nm nickel and cobalt nanowires,” *Nano Lett.*, vol. 3, no. 8, pp. 1079–1082, 2003, doi: 10.1021/nl0342545.

[30] C. Schönenberger *et al.*, “Template Synthesis of Nanowires in Porous Polycarbonate Membranes: Electrochemistry and Morphology,” *J. Phys. Chem. B*, vol. 101, no. 28, pp. 5497–5505, 1997, doi: 10.1021/JP963938G.

[31] J. D. Klein, R. D. Herrick, D. Palmer, M. J. Sailor, C. J. Brumlik, and C. R. Martin, “Electrochemical fabrication of cadmium chalcogenide microdiode arrays,” *Chem. Mater.*, vol. 5, no. 7, pp. 902–904, Jul. 1993, doi: 10.1021/cm00031a002.

[32] L. Yang and W. W.-F. Leung, “Application of a Bilayer TiO_2 Nanofiber Photoanode for Optimization of Dye-Sensitized Solar Cells,” *Adv. Mater.*, vol. 23, no. 39, pp. 4559–4562, Oct. 2011, doi: 10.1002/adma.201102717.

[33] R. Sedghi, A. Shaabani, Z. Mohammadi, F. Y. Samadi, and E. Isaei, “Biocompatible electrospinning chitosan nanofibers: A novel delivery system with superior local cancer therapy,” *Carbohydr. Polym.*, vol. 159, pp. 1–10, Mar. 2017, doi: 10.1016/J.CARBPOL.2016.12.011.

[34] S. Almuhamed *et al.*, “Electrospinning composite nanofibers of polyacrylonitrile/synthetic Na-montmorillonite,” *J. Ind. Eng. Chem.*, vol. 35, pp. 146–152, Mar. 2016, doi: 10.1016/J.JIEC.2015.12.024.

[35] X. Li, “Metal assisted chemical etching for high aspect ratio nanostructures: A review of characteristics and applications in photovoltaics,” *Curr. Opin. Solid State Mater. Sci.*, vol. 16, no. 2, pp. 71–81, Apr. 2012, doi: 10.1016/J.COSSMS.2011.11.002.

[36] D. Rawtani, T. Sajan, A. Twinkle, and Y. K. Agrawal, “Emerging Strategies for Synthesis and manipulation of nanowires: A Review,” *Rev. Adv. Mater. Sci.*, vol. 40, pp. 177–187, 2015, Accessed: Sep. 20, 2018. [Online]. Available: http://www.ipme.nw.ru/e-journals/RAMS/no_24015/07_24015_rawtani.pdf.

[37] G. Cao and D. Liu, “Template-based synthesis of nanorod, nanowire, and nanotube arrays,” *Adv. Colloid Interface Sci.*, vol. 136, no. 1–2, pp. 45–64, 2008, doi: 10.1016/j.cis.2007.07.003.

[38] T. Ohgai *et al.*, “Template synthesis and magnetoresistance property of Ni and Co single nanowires electrodeposited into nanopores with a wide range of aspect ratios,” *J. Phys. D Appl. Phys. J. Phys. D Appl. Phys. J. Phys. D Appl. Phys*, vol. 36, no. 36, pp. 3109–3114, 2003, Accessed: May 15, 2018. [Online]. Available: http://iopscience.iop.org/article/10.1088/0022-3727/36/24/003/pdf.

[39] A. J. Bard, L. R. Faulkner, and others, “Fundamentals and applications,” *Electrochem. Methods*, vol. 2, no. 482, pp. 580–632, 2001.

[40] T. M. Whitney, P. C. Searson, J. S. Jiang, and C. L. Chien, “Fabrication and magnetic properties of arrays of metallic nanowires.,” *Science (80-.).*, vol. 261, no. 5126, pp. 1316–1319, Sep. 1993, doi: 10.1126/science.261.5126.1316.

[41] C. Schonenberger *et al.*, “Template Synthesis of Nanowires in Porous Polycarbonate Membranes: Electrochemistry and Morphology,” *J. Phys. Chem. B*, vol. 101, no. 28, pp. 5497–5505, 1997, Accessed: May 10, 2018. [Online]. Available: https://pubs.acs.org/doi/pdf/10.1021/jp963938g.

[42] H. Cao *et al.*, “Generation and growth mechanism of metal (Fe, Co, Ni) nanotube arrays,” *ChemPhysChem*, vol. 7, no. 7, pp. 1500–1504, 2006, doi: 10.1002/cphc.200500690.

[43] Z. Wang, Y.-K. Su, and H.-L. Li, “AFM study of gold nanowire array electrodeposited within anodic aluminum oxide template,” *Appl. Phys. A Mater. Sci. Process.*, vol. 74, no. 4, pp. 563–565, Apr. 2002, doi: 10.1007/s003390100909.

[44] T. Shimizu, T. Xie, J. Nishikawa, S. Shingubara, S. Senz, and U. Gösele, “Synthesis of Vertical High-Density Epitaxial Si(100) Nanowire Arrays on a Si(100) Substrate Using an Anodic Aluminum Oxide Template,” *Adv. Mater.*, vol. 19, no. 7, pp. 917–920, Apr. 2007, doi: 10.1002/adma.200700153.

[45] Zheng Miao, D. Xu, Jianhua Ouyang, G. Guo, X. Zhao, and Y. Tang, “Electrochemically Induced Sol−Gel Preparation of Single-Crystalline TiO2 Nanowires,” *Nano Lett.*, vol. 2, pp. 717–720, 2002, doi: 10.1021/NL025541W.

[46] D. J. Peña *et al.*, “Template Growth of Photoconductive Metal−CdSe−Metal Nanowires,” *J. Phys. Chem. B*, vol. 106, pp. 7458–7462, 2002, doi: 10.1021/JP0256591.

[47] V. Vega *et al.*, “Tuning the magnetic anisotropy of Co–Ni nanowires: comparison between single nanowires and nanowire arrays in hard-anodic aluminum oxide membranes,” *Nanotechnology*, vol. 23, no. 46, p. 465709, Nov. 2012, doi: 10.1088/0957-4484/23/46/465709.

[48] Z. Su and W. Zhou, “Formation mechanism of porous anodic aluminium and titanium oxides,” *Adv. Mater.*, vol. 20, no. 19, pp. 3663–3667, 2008, doi: 10.1002/adma.200800845.

[49] S. Kian Cheah *et al.*, “Self-Supported Three-Dimensional Nanoelectrodes for Microbattery Applications,” *Nano Lett.*, vol. 9, no. 9, pp. 3230–3233, 2009, doi: 10.1021/nl9014843.

[50] C. Schönenberger *et al.*, “Template Synthesis of Nanowires in Porous Polycarbonate Membranes: Electrochemistry and Morphology,” *J. Phys. Chem. B*, vol. 101, no. 28, pp. 5497–5505, Jul. 1997, doi: 10.1021/jp963938g.

[51] L. Zaraska, G. D. Sulka, and M. Jaskuła, “Porous anodic alumina membranes formed by anodization of AA1050 alloy as templates for fabrication of metallic nanowire arrays,” *Surf. Coatings Technol.*, vol. 205, no. 7, pp. 2432–2437, Dec. 2010, doi: 10.1016/J.SURFCOAT.2010.09.038.

[52] X. Wang, S. Ma, X. Wang, C. Ma, and Z. Yuan, “Facile conversion of Zn nanowires to Zn nanotubes by heating-induced volatilization in nanopores of anodic aluminum oxide template,” *Vacuum*, vol. 132, pp. 86–90, Oct. 2016, doi: 10.1016/J.VACUUM.2016.07.029.

[53] S. Shin, B. H. Kong, B. S. Kim, K. M. Kim, H. K. Cho, and H. H. Cho, “Over 95% of large-scale length uniformity in template-assisted electrodeposited nanowires by subzero-temperature electrodeposition,” *Nanoscale Res. Lett.*, vol. 6, no. 1, p. 467, 2011, doi: 10.1186/1556-276x-6-467.

[54] T. Katase, K. Murase, T. Hirato, and Y. Awakura, “Redox and transport behaviors of Cu(I) ions in TMHA-Tf2N ionic liquid solution,” *J. Appl. Electrochem.*, vol. 37, no. 3, pp. 339–344, Feb. 2007, doi: 10.1007/s10800-006-9262-4.

[55] J. E. Graves, M. E. A. Bowker, A. Summer, A. Greenwood, C. Ponce de León, and F. C. Walsh, “A new procedure for the template synthesis of metal nanowires,” *Electrochem. commun.*, vol. 87, pp. 58–62, Feb. 2018, doi: 10.1016/J.ELECOM.2017.11.022.

[56] X. Zhang, D. Li, L. Bourgeois, H. Wang, and P. A. Webley, “Direct Electrodeposition of Porous Gold Nanowire Arrays for Biosensing Applications,” *ChemPhysChem*, vol. 10, no. 2, pp. 436–441, Feb. 2009, doi: 10.1002/cphc.200800538.

[57] J. Fu, S. Cherevko, and C.-H. Chung, “Electroplating of metal nanotubes and nanowires in a high aspect-ratio nanotemplate,” *Electrochem. commun.*, vol. 10, no. 4, pp. 514–518, Apr. 2008, doi: 10.1016/J.ELECOM.2008.01.015.

[58] C. G. Jin *et al.*, “Fabrication of large-area single crystal bismuth nanowire arrays,” *J. Mater. Chem.*, vol. 13, no. 7, p. 1743, Jun. 2003, doi: 10.1039/b302303f.

[59] V. Vega *et al.*, “Tuning the magnetic anisotropy of Co-Ni nanowires: comparison between single nanowires and nanowire arrays in hard-anodic aluminum oxide membranes,” *Nanotechnology*, vol. 23, p. 465709, 2012, doi: 10.1088/0957-4484/23/46/465709.

[60] S. Atalay, H. Kaya, F. E. Atalay, and E. Aydogmus, “Magnetoimpedance effects in a CoNiFe nanowire array,” *J. Alloys Compd.*, vol. 561, pp. 71–75, 2013, doi: 10.1016/j.jallcom.2013.01.173.

[61] N. Liakakos *et al.*, “Solution Epitaxial Growth of Cobalt Nanowires on Crystalline Substrates for Data Storage Densities beyond 1 Tbit/in ^{2},” *Nano Lett.*, vol. 14, no. 6, pp. 3481–3486, Jun. 2014, doi: 10.1021/nl501018z.

[62] S. F. Akhtarianfar, A. Ramazani, M. Almasi-Kashi, and A. H. Montazer, “The effect of barrier layer conditions on the electrodeposition efficiency and magnetic properties of Fe nanowire arrays,” *Appl. Phys. A*, vol. 124, no. 5, p. 379, May 2018, doi: 10.1007/s00339-018-1805-0.

[63] A. J. Yin, J. Li, W. Jian, A. J. Bennett, and J. M. Xu, “Fabrication of highly ordered metallic nanowire arrays by electrodeposition,” *Appl. Phys. Lett.*, vol. 79, no. 7, pp. 1039–1041, Aug. 2001, doi: 10.1063/1.1389765.

[64] D. Wang *et al.*, “Electrodeposition of Metallic Nanowire Thin Films Using Mesoporous Silica Templates,” *Adv. Mater.*, vol. 15, no. 2, pp. 130–133, Jan. 2003, doi: 10.1002/adma.200390025.

[65] K. Kim, M. Kim, and S. M. Cho, “Pulsed electrodeposition of palladium nanowire arrays using AAO template,” *Mater. Chem. Phys.*, vol. 96, no. 2–3, pp. 278–282, Apr. 2006, doi: 10.1016/J.MATCHEMPHYS.2005.07.013.

[66] Y. Konishi, M. Motoyama, H. Matsushima, Y. Fukunaka, R. Ishii, and Y. Ito, “Electrodeposition of Cu nanowire arrays with a template,” *J. Electroanal. Chem.*, vol. 559, pp. 149–153, Nov. 2003, doi: 10.1016/S0022-0728(03)00157-8.

[67] J.-G. Wang, M.-L. Tian, N. Kumar, and T. E. Mallouk, “Controllable Template Synthesis of Superconducting Zn Nanowires with Different Microstructures by Electrochemical Deposition,” *Nano Lett.*, vol. 5, no. 7, pp. 1247–1253, 2005, doi: 10.1021/nl050918u.

[68] T. Gao *et al.*, “Template synthesis of single-crystal Cu nanowire arrays by electrodeposition,” *Appl. Phys. A*, vol. 73, pp. 251–254, 2001, doi: 10.1007/s003390100910.

[69] P. G. Schiavi, P. Altimari, A. Rubino, and F. Pagnanelli, “Electrodeposition of cobalt nanowires into alumina templates generated by one-step anodization,” *Electrochim. Acta*, vol. 259, pp. 711–722, Jan. 2018, doi: 10.1016/J.ELECTACTA.2017.11.035.

[70] J. Choi, G. Sauer, K. Nielsch, R. B. Wehrspohn, and U. Gösele, “Hexagonally Arranged Monodisperse Silver Nanowires with Adjustable Diameter and High Aspect Ratio,” *Chem. Mater.*, vol. 15, pp. 776–779, 2003, doi: 10.1021/cm0208758.

[71] D. Borissov, S. Isik-Uppenkamp, and M. Rohwerder, “Fabrication of Iron Nanowire Arrays by Electrodeposition into Porous Alumina,” *J. Phys. Chem. C*, vol. 113, pp. 3133–3138, 2009, doi: 10.1021/jp809202h.

[72] L. M. Graham, S. Cho, S. K. Kim, M. Noked, and S. B. Lee, “Role of boric acid in nickel nanotube electrodeposition: a surface-directed growth mechanism,” *Chem. Commun.*, vol. 50, no. 5, pp. 527–529, Dec. 2014, doi: 10.1039/C3CC47183G.

[73] J. S. Santos, R. Matos, F. Trivinho-Strixino, and E. C. Pereira, “Effect of temperature on Co electrodeposition in the presence of boric acid,” *Electrochim. Acta*, vol. 53, no. 2, pp. 644–649, Dec. 2007, doi: 10.1016/j.electacta.2007.07.025.

[74] H. Schlörb *et al.*, "Magnetic nanowires by electrodeposition within templates," *Phys. status solidi*, vol. 247, no. 10, pp. 2364–2379, Aug. 2010, doi: 10.1002/pssb.201046189.

[75] J. Keyani, "Electrodeposition and device incorporation of bismuth antimony nanowire arrays," University of California, Berkeley, 2007.

[76] L. Trahey, C. R. Becker, and A. M. Stacy, "Electrodeposited Bismuth Telluride Nanowire Arrays with Uniform Growth Fronts," *Nano Lett.*, vol. 7, no. 8, pp. 2535–2539, Aug. 2007, doi: 10.1021/nl070711w.

[77] A.W.Hull, "A new method of chemical analysis," *J. Am. Chem. Soc.*, vol. 41, no. 8, pp. 1168–1175, 1919, Accessed: Apr. 24, 2018. [Online]. Available: https://pubs.acs.org/doi/pdf/10.1021/ja02229a003.

[78] B. C. Deceased and S. R. Stock, *Elements of X-ray Diffraction*, 3rd ed. Addision-Wesley, 1956.

[79] L. S. Birks and H. Friedman, "Particle Size Determination from X-Ray Line Broadening," *J. Appl. Phys.*, vol. 17, no. 8, pp. 687–692, Aug. 1946, doi: 10.1063/1.1707771.

[80] J. Li, T. Malis, and S. Dionne, "Recent advances in FIB-TEM specimen preparation techniques," *Mater. Charact.*, vol. 57, no. 1, pp. 64–70, Jul. 2006, doi: 10.1016/j.matchar.2005.12.007.

[81] R. J. Patterson, D. Mayer, L. Weaver, and M. W. Phaneuf, "'H-Bar Lift-Out' and 'Plan-View Lift-Out': Robust, Re-thinnable FIB-TEM Preparation for Ex-Situ Cross-Sectional and Plan-View FIB Specimen Preparation," *Microsc. Microanal.*, vol. 8, no. S02, pp. 566–567, Aug. 2002, doi: 10.1017/s1431927602105502.

[82] H.-Y. Sun, "Template-Based Electrodeposition Growth Mechanism of Metal Nanotubes," *J. Electrochem. Soc.*, vol. 160, no. 2, pp. D41–D45, 2012, doi: 10.1149/2.049302jes.

[83] S. Shin, B. S. Kim, K. M. Kim, B. H. Kong, H. K. Cho, and H. H. Cho, "Tuning the morphology of copper nanowires by controlling the growth processes in electrodeposition," *J. Mater. Chem.*, vol. 21, pp. 17967–17971, 2011, doi: 10.1039/c1jm14403k.

[84] J. Xu, X. Huang, G. Xie, Y. Fang, and D. Liu, "Fabrication and magnetic property of monocrystalline cobalt nanowire array by direct current electrodeposition," *Mater. Lett.*, vol. 59, no. 8–9, pp. 981–984, Apr. 2005, doi: 10.1016/j.matlet.2004.11.042.

[85] A. Taylor and R. W. Floyd, "Precision measurements of lattice parameters of non-cubic crystals," *Acta Crystallogr.*, vol. 3, no. 4, pp. 285–289, Jul. 1950, doi: 10.1107/s0365110x50000732.

[86] X. H. Huang, G. H. Li, G. Z. Sun, X. C. Dou, L. Li, and L. X. Zheng, “Initial growth of single-crystalline nanowires: From 3D nucleation to 2D growth,” *Nanoscale Res. Lett.*, vol. 5, no. 6, pp. 1057–1062, 2010, doi: 10.1007/s11671-010-9602-5.

[87] X. Dou, G. Li, and H. Lei, “Kinetic versus thermodynamic control over growth process of electrodeposited Bi/BiSb superlattice nanowires,” *Nano Lett.*, vol. 8, no. 5, pp. 1286–1290, 2008, doi: 10.1021/nl073039b.

[88] R. L. Schwoebel and E. J. Shipsey, “Step Motion on Crystal Surfaces,” *J. Appl. Phys.*, vol. 37, no. 10, pp. 3682–3686, Sep. 1966, doi: 10.1063/1.1707904.

[89] G. Ehrlich and F. G. Hudda, “Atomic View of Surface Self-Diffusion: Tungsten on Tungsten,” *J. Chem. Phys.*, vol. 44, no. 3, pp. 1039–1049, Feb. 1966, doi: 10.1063/1.1726787.

[90] P. Keblinski, S. Phillpot, S. U. S. Choi, and J. A. Eastman, “Mechanisms of heat flow in suspensions of nano-sized particles (nanofluids),” *Int. J. Heat Mass Transf.*, vol. 45, no. 4, pp. 855–863, 2002, Accessed: Nov. 25, 2019. [Online]. Available: https://www.sciencedirect.com/science/article/pii/S0017931001001752.

[91] G. A. Pilkington and W. H. Briscoe, “Nanofluids mediating surface forces,” *Adv. Colloid Interface Sci.*, vol. 179–182, pp. 68–84, Nov. 2012, doi: 10.1016/J.CIS.2012.06.007.

[92] B. Wei, C. Zou, and X. Li, “Experimental investigation on stability and thermal conductivity of diathermic oil based TiO2 nanofluids,” *Int. J. Heat Mass Transf.*, vol. 104, pp. 537–543, Jan. 2017, doi: 10.1016/J.IJHEATMASSTRANSFER.2016.08.078.

[93] M. Hemmat Esfe and S. Saedodin, “Turbulent forced convection heat transfer and thermophysical properties of Mgo–water nanofluid with consideration of different nanoparticles diameter, an empirical study,” *J. Therm. Anal. Calorim.*, vol. 119, no. 2, pp. 1205–1213, Feb. 2015, doi: 10.1007/s10973-014-4197-1.

[94] S. K. Das, N. Putra, P. Thiesen, and W. Roetzel, “Temperature Dependence of Thermal Conductivity Enhancement for Nanofluids,” *J. Heat Transfer*, vol. 125, no. 4, pp. 567–574, Jul. 2003, doi: 10.1115/1.1571080.

[95] M. Hemmat Esfe, M. Firouzi, and M. Afrand, “Experimental and theoretical investigation of thermal conductivity of ethylene glycol containing functionalized single walled carbon nanotubes,” *Phys. E Low-dimensional Syst. Nanostructures*, vol. 95, no. January, pp. 71–77, Jan. 2018, doi: 10.1016/J.PHYSE.2017.08.017.

[96] T.-P. Teng and C.-C. Yu, “Heat dissipation performance of MWCNTs nano-coolant for vehicle,” *Exp. Therm. Fluid Sci.*, vol. 49, pp. 22–30, Sep. 2013, doi: 10.1016/J.EXPTHERMFLUSCI.2013.03.007.

[97] A. M. Hussein, R. A. Bakar, and K. Kadirgama, “Study of forced convection nanofluid heat transfer in the automotive cooling system,” *Case Stud. Therm. Eng.*, vol. 2, pp. 50–61, Mar. 2014, doi: 10.1016/J.CSITE.2013.12.001.

[98] L. S. Sundar and K. V. Sharma, “Thermal Conductivity enhancement of nanoparticles in distilled water,” *Int. J. Nanoparticles*, vol. 1, no. 1, pp. 66–77, 2008, Accessed: Oct. 01, 2019. [Online]. Available: https://www.researchgate.net/profile/K_Sharma2/publication/249923115_Thermal_conductivity_enhancement_of_nanoparticles_in_distilled_water/links/58a599144585150402d06c0a/Thermal-conductivity-enhancement-of-nanoparticles-in-distilled-water.pdf.

[99] A. J. Sundararaj, L. G. Asirvatham, B. C. Pillai, and S. Panicker, “Thermophysical properties of refined kerosene—alumina nanofluid,” in *Recent Advances in Materials, Mechanics and Management: Proceedings of the 3rd International Conference on Materials, Mechanics and Management (IMMM 2017), July 13-15, 2017, Trivandrum, Kerala, India*, 2019, p. 263.

[100] H. T. Zhu, C. Y. Zhang, Tang Ya M., and Wang Ji X., “Novel Synthesis and Thermal Conductivity of CuO Nanofluid,” *J. Phys. Chem. C*, vol. 111, pp. 1646–1650, 2007, Accessed: Oct. 01, 2019. [Online]. Available: https://pubs.acs.org/doi/pdf/10.1021/jp065926t.

[101] A. Karimi, M. Goharkhah, M. Ashjaee, and M. B. Shafii, “Thermal Conductivity of Fe2O3 and Fe3O4 Magnetic Nanofluids Under the Influence of Magnetic Field,” *Int. J. Thermophys.*, vol. 36, no. 10–11, pp. 2720–2739, 2015, doi: 10.1007/s10765-015-1977-1.

[102] P. D. Shima, J. Philip, and B. Raj, “Dependence on Thermal Conductivity and Viscosity,” *J. Phys. Chem. C*, vol. 114, no. 44, pp. 18825–18833, 2010.

[103] D.-H. Yoo, K. S. Hong, and H.-S. Yang, “Study of thermal conductivity of nanofluids for the application of heat transfer fluids,” *Thermochim. Acta*, vol. 455, no. 1–2, pp. 66–69, Apr. 2007, doi: 10.1016/J.TCA.2006.12.006.

[104] L. S. Sundar, M. K. Singh, and A. C. M. Sousa, “Thermal conductivity of ethylene glycol and water mixture based Fe3O4 nanofluid,” *Int. Commun. Heat Mass Transf.*, vol. 49, pp. 17–24, Dec. 2013, doi: 10.1016/J.ICHEATMASSTRANSFER.2013.08.026.

[105] M. Hemmat Esfe, W.-M. Yan, M. Akbari, A. Karimipour, and M. Hassani, “Experimental study on thermal conductivity of DWCNT-ZnO/water-EG nanofluids,” *Int. Commun. Heat Mass Transf.*, vol. 68, pp. 248–251, Nov. 2015, doi: 10.1016/J.ICHEATMASSTRANSFER.2015.09.001.

[106] D. Toghraie, V. A. Chaharsoghi, and M. Afrand, “Measurement of thermal conductivity of ZnO–TiO2/EG hybrid nanofluid,” *J. Therm. Anal. Calorim.*, vol. 125, no. 1, pp. 527–535, Jul. 2016, doi: 10.1007/s10973-016-5436-4.

[107] A. Hussanan, M. Z. Salleh, and I. Khan, “Microstructure and inertial characteristics of a magnetite ferrofluid over a stretching/shrinking sheet using effective thermal conductivity model,” *J. Mol. Liq.*, vol. 255, pp. 64–75, Apr. 2018, doi: 10.1016/J.MOLLIQ.2018.01.138.

[108] V. Ganesan, C. Louis, and S. P. Damodaran, “Novel Nanofluids Based on Magnetite Nanoclusters and Investigation on Their Cluster Size-Dependent Thermal Conductivity,” *J. Phys. Chem. C*, vol. 122, no. 12, pp. 6918–6929, Mar. 2018, doi: 10.1021/acs.jpcc.7b12043.

[109] H. E. Patel, A. T. Sundararajan, A. E. Sarit, and K. Das, “An experimental investigation into the thermal conductivity enhancement in oxide and metallic nanofluids,” *J. Nanoparticle Res.*, vol. 12, pp. 1015–1031, 2010, doi: 10.1007/s11051-009-9658-2.

[110] R. Chen, M.-C. Lu, V. Srinivasan, Z. Wang, H. H. Cho, and A. Majumdar, “Nanowires for Enhanced Boiling Heat Transfer,” *Nano Lett.*, vol. 9, no. 2, pp. 548–553, 2008, doi: 10.1021/nl8026857.

[111] M. H. Ahmadi, A. Mirlohi, M. Alhuyi Nazari, and R. Ghasempour, “A review of thermal conductivity of various nanofluids,” *J. Mol. Liq.*, vol. 265, pp. 181–188, Sep. 2018, doi: 10.1016/j.molliq.2018.05.124.

[112] S. Sanukrishna and M. Prakash, “Experimental studies on thermal and rheological behaviour of TiO2-PAG nanolubricant for refrigeration system,” *Int. J. Refrig.*, vol. 86, pp. 356–372, 2018, Accessed: Feb. 12, 2020. [Online]. Available: https://www.sciencedirect.com/science/article/pii/S0140700717304577.

[113] R. Singh, A. Sharma, and A. Dixit, “Experimental investigation of thermal conductivity and specific heat of nanoparticles mixed cutting fluids,” in *Matrialstoday: Proceedings*, 2017, pp. 8587–8596, Accessed: Feb. 12, 2020. [Online]. Available: https://www.sciencedirect.com/science/article/pii/S2214785317315031.

[114] R. Kathiravan, R. Kumar, A. Gupta, and R. Chandra, “Preparation and pool boiling characteristics of copper nanofluids over a flat plate heater,” *Int. J. Heat Mass Transf.*, vol. 53, no. 9–10, pp. 1673–1681, Apr. 2010, doi: 10.1016/j.ijheatmasstransfer.2010.01.022.

[115] H. D. Koca, S. Doganay, and A. Turgut, “Thermal characteristics and performance of Ag-water nanofluid: Application to natural circulation loops,” *Energy Convers. Manag.*, vol. 135, pp. 9–20, Mar. 2017, doi: 10.1016/j.enconman.2016.12.058.

[116] Z. Aparna, M. Michael, S. K. Pabi, and S. Ghosh, “Thermal conductivity of aqueous Al 2 O 3 /Ag hybrid nanofluid at different temperatures and volume concentrations: An experimental investigation and development of new correlation function,” *Powder Technol.*, vol. 343, pp. 714–722, Feb. 2019, doi: 10.1016/j.powtec.2018.11.096.

[117] R. Gómez-Villarejo *et al.*, “Ag-based nanofluidic system to enhance heat transfer fluids for concentrating solar power: Nano-level insights,” *Appl. Energy*, vol. 194, pp. 19–29, May 2017, doi: 10.1016/j.apenergy.2017.03.003.

[118] R. Agarwal, K. Verma, N. K. Agrawal, and R. Singh, “Comparison of Experimental Measurements of Thermal Conductivity of Fe2O3 Nanofluids Against Standard Theoretical Models and Artificial Neural Network Approach,” *J. Mater. Eng. Perform.*, vol. 28, no. 8, pp. 4602–4609, Aug. 2019, doi: 10.1007/s11665-019-04202-z.

[119] X. Zhang, H. Gu, and M. Fujii, “Effective thermal conductivity and thermal diffusivity of nanofluids containing spherical and cylindrical nanoparticles,” *Exp. Therm. Fluid Sci.*, vol. 31, no. 6, pp. 593–599, May 2007, doi: 10.1016/j.expthermflusci.2006.06.009.

[120] L. S. Sundar, G. O. Irurueta, E. Venkata Ramana, M. K. Singh, and A. C. M. Sousa, “Thermal conductivity and viscosity of hybrid nanfluids prepared with magnetic nanodiamond-cobalt oxide (ND-Co3O4) nanocomposite,” *Case Stud. Therm. Eng.*, vol. 7, pp. 66–77, Mar. 2016, doi: 10.1016/j.csite.2016.03.001.

[121] A. Mariano, M. J. Pastoriza-Gallego, L. Lugo, L. Mussari, and M. M. Piñeiro, “Co3O4 ethylene glycol-based nanofluids: Thermal conductivity, viscosity and high pressure density,” *Int. J. Heat Mass Transf.*, vol. 85, pp. 54–60, Jun. 2015, doi: 10.1016/j.ijheatmasstransfer.2015.01.061.

[122] L. S. Sundar, M. K. Singh, E. V. Ramana, B. Singh, J. Grácio, and A. C. M. Sousa, “Enhanced Thermal Conductivity and Viscosity of Nanodiamond-Nickel Nanocomposite Nanofluids,” *Sci. Rep.*, vol. 4, no. 1, pp. 1–14, Apr. 2014, doi: 10.1038/srep04039.

[123] A. Karimi, M. A. A. Sadatlu, B. Saberi, H. Shariatmadar, and M. Ashjaee, “Experimental investigation on thermal conductivity of water based nickel ferrite nanofluids,” *Adv. Powder Technol.*, vol. 26, no. 6, pp. 1529–1536, Nov. 2015, doi: 10.1016/j.apt.2015.08.015.

[124] H. Akoh, Y. Tsukasaki, S. Yatsuya, A. T.-J. of C. Growth, and undefined 1978, “Magnetic properties of ferromagnetic ultrafine particles prepared by vacuum evaporation on running oil substrate,” *Elsevier*, Accessed: Feb. 24, 2020. [Online]. Available: https://www.sciencedirect.com/science/article/pii/0022024878904827.

[125] J. Eastman, U. Choi, L. Thompson, and S. Lee, “Enhanced Thermal Conductivity through the Development of Nanofluids,” in *MRS Proceedings*, 1996, pp. 3–11, Accessed: Feb. 24, 2020. [Online]. Available: https://sci-hub.tw/https://www.cambridge.org/core/journals/mrs-online-proceedings-library-archive/article/enhanced-thermal-conductivity-through-the-development-of-nanofluids/0C0FED1470292813BB63D7EC4006E183.

[126] I. Ho, S. Yang, T.-K. Hong, H.-S. Yang, and C. J. Choi, “Study of the Enhanced Thermal Conductivity of Fe Nanofluids,” *J. Appl. Phys.*, vol. 97, no. 6, 2005, doi: 10.1063/1.1861145.

[127] S. M. S. Murshed, K. C. Leong, and C. Yang, “Enhanced thermal conductivity of TiO2 - Water based nanofluids,” *Int. J. Therm. Sci.*, vol. 44, no. 4, pp. 367–373, Apr. 2005, doi: 10.1016/j.ijthermalsci.2004.12.005.

[128] Y. Xuan and Q. Li, “Heat transfer enhancement of nanofluids,” *Int. J. Heat Fluid Flow*, vol. 21, no. 1, pp. 58–64, Feb. 2000, doi: 10.1016/S0142-727X(99)00067-3.

[129] M. Ghanbarpour, E. Bitaraf Haghigi, and R. Khodabandeh, “Thermal properties and rheological behavior of water based Al2O3 nanofluid as a heat transfer fluid,” *Exp. Therm. Fluid Sci.*, vol. 53, pp. 227–235, Feb. 2014, doi: 10.1016/j.expthermflusci.2013.12.013.

[130] T. P. Teng and C. C. Yu, “Heat dissipation performance of MWCNTs nano-coolant for vehicle,” *Exp. Therm. Fluid Sci.*, vol. 49, pp. 22–30, Sep. 2013, doi: 10.1016/j.expthermflusci.2013.03.007.

[131] M. R. Raveshi, A. Keshavarz, M. S. Mojarrad, and S. Amiri, “Experimental investigation of pool boiling heat transfer enhancement of alumina-water-ethylene glycol nanofluids,” *Exp. Therm. Fluid Sci.*, vol. 44, pp. 805–814, Jan. 2013, doi: 10.1016/j.expthermflusci.2012.09.025.

[132] S. Zeinali Heris, T. H. Nassan, S. H. Noie, H. Sardarabadi, and M. Sardarabadi, “Laminar convective heat transfer of Al2O3/water nanofluid through square cross-sectional duct,” *Int. J. Heat Fluid Flow*, vol. 44, pp. 375–382, Dec. 2013, doi: 10.1016/j.ijheatfluidflow.2013.07.006.

[133] Y. Vermahmoudi, S. M. Peyghambarzadeh, S. H. Hashemabadi, and M. Naraki, “Experimental investigation on heat transfer performance of Fe 2 O 3/water nanofluid in an air-finned heat exchanger,” *Eur. J. Mech. B/Fluids*, vol. 44, pp. 32–41, Mar. 2014, doi: 10.1016/j.euromechflu.2013.10.002.

[134] M. Naraki, S. M. Peyghambarzadeh, S. H. Hashemabadi, and Y. Vermahmoudi, “Parametric study of overall heat transfer coefficient of CuO/water nanofluids in a car radiator,” *Int. J. Therm. Sci.*, vol. 66, pp. 82–90, Apr. 2013, doi: 10.1016/j.ijthermalsci.2012.11.013.

[135] W. Russel, D. Saville, and W. Schowalter, *Colloidal dispersions*. 1991.

[136] F. Yu *et al.*, "Dispersion stability of thermal nanofluids," *Prog. Nat. Sci. Mater. Int.*, vol. 27, no. 5, pp. 531–542, Oct. 2017, doi: 10.1016/J.PNSC.2017.08.010.

[137] C. Brinker and G. Scherer, *Sol-gel science: the physics and chemistry of sol-gel processing*. Academic Press, Inc., 2013.

[138] W. Evans, R. Prasher, J. Fish, P. Meakin, P. Phelan, and P. Keblinski, "Effect of aggregation and interfacial thermal resistance on thermal conductivity of nanocomposites and colloidal nanofluids," *Int. J. Heat Mass Transf.*, vol. 51, no. 5–6, pp. 1431–1438, Mar. 2008, doi: 10.1016/J.IJHEATMASSTRANSFER.2007.10.017.

[139] E. V. Timofeeva *et al.*, "Thermal conductivity and particle agglomeration in alumina nanofluids: Experiment and theory," *Phys. Rev. E*, vol. 76, no. 6, p. 061203, Dec. 2007, doi: 10.1103/PhysRevE.76.061203.

[140] K. S. Hong, T.-K. Hong, and H.-S. Yang, "Thermal conductivity of Fe nanofluids depending on the cluster size of nanoparticles," *Appl. Phys. Lett.*, vol. 88, no. 3, p. 031901, Jan. 2006, doi: 10.1063/1.2166199.

[141] Y. Hwang *et al.*, "Stability and thermal conductivity characteristics of nanofluids," *Thermochim. Acta*, vol. 455, no. 1–2, pp. 70–74, Apr. 2007, doi: 10.1016/J.TCA.2006.11.036.

[142] A. Ghadimi, R. Saidur, and H. S. C. Metselaar, "A review of nanofluid stability properties and characterization in stationary conditions," *Int. J. Heat Mass Transf.*, vol. 54, no. 17–18, pp. 4051–4068, Aug. 2011, doi: 10.1016/J.IJHEATMASSTRANSFER.2011.04.014.

[143] V. Trisaksri and S. Wongwises, "Critical review of heat transfer characteristics of nanofluids," Renewable and Sustainable Energy Reviews, vol. 11, no. 3. Pergamon, pp. 512–523, Apr. 01, 2007, doi: 10.1016/j.rser.2005.01.010.

[144] M. Chandrasekar and S. Suresh, "A Review on the Mechanisms of Heat Transport in Nanofluids," *Heat Transf. Eng.*, vol. 30, no. 14, pp. 1136–1150, Dec. 2009, doi: 10.1080/01457630902972744.

[145] J. C. Maxwell, *A treatise on electricity and magnetism*. Oxford: Clarendon press, 1873.

[146] S. Lee, S. U.-S. Choi, S. Li, and J. A. Eastman, "Measuring Thermal Conductivity of Fluids Containing Oxide Nanoparticles," *J. hea*, vol. 121, no. 2, pp. 280–289, 1999, Accessed: Dec. 04, 2019. [Online]. Available: http://heattransfer.asmedigitalcollection.asme.org/.

[147] J. R. Henderson and F. van Swol, “On the interface between a fluid and a planar wall theory and simulations of a hard sphere fluid at a hard wall,” *Mol. Phys.*, vol. 51, no. 4, pp. 991–1010, 1984, doi: 10.1080/00268978400100651.

[148] C. J. Yu, A. G. Richter, A. Datta, M. K. Durbin, and P. Dutta, “Molecular layering in a liquid on a solid substrate: An X-ray reflectivity study,” *Phys. B Condens. Matter*, vol. 283, no. 1–3, pp. 27–31, 2000, doi: 10.1016/S0921-4526(99)01885-2.

[149] D. Song, D. Jing, W. Ma, and X. Zhang, “High thermal conductivity of nanoparticles not necessarily contributing more to nanofluids,” *Appl. Phys. Lett.*, vol. 113, no. 22, Nov. 2018, doi: 10.1063/1.5055058.

[150] J. Selinger *et al.*, “Thermal Conductivity and Particle Agglomeration in Alumina Nanofluids: Experiment and Theory,” *Phys. Rev. E*, no. 6, p. 76, 2007, doi: 10.1103/PhysRevE.76.061203.

[151] D. Song, Y. Yang, D. J.-I. J. of H. and M. Transfer, and U. 2017, “Insight into the contribution of rotating Brownian motion of nonspherical particle to the thermal conductivity enhancement of nanofluid,” *Int. J. Heat Mass Transf.*, vol. 112, pp. 61–71, 2017, Accessed: Dec. 02, 2019. [Online]. Available: https://www.sciencedirect.com/science/article/pii/S0017931017308013.

[152] A. Majumdar and P. Reddy, “Role of electron-phonon coupling in thermal conductance of metal-nonmetal interfaces,” *Appl. Phys. Lett.*, vol. 84, no. 23, pp. 4768–4770, Jun. 2004, doi: 10.1063/1.1758301.

[153] F. Iacobazzi, M. Milanese, G. Colangelo, M. Lomascolo, and A. de Risi, “An explanation of the Al2O3 nanofluid thermal conductivity based on the phonon theory of liquid,” *Energy*, vol. 116, pp. 786–794, Dec. 2016, doi: 10.1016/j.energy.2016.10.027.

[154] D. X. Song, Y. F. Zhang, W. G. Ma, and X. Zhang, “Role of electron-phonon coupling in thermal conductivity of metallic nanofluids,” *J. Phys. D. Appl. Phys.*, vol. 52, no. 48, Sep. 2019, doi: 10.1088/1361-6463/ab3aac.

[155] T. Qiu, C. T.-I. J. of H. and M. Transfer, and U. 1992, “Short-pulse laser heating on metals,” *Int. J. Heat Mass Transf.*, vol. 35, no. 3, pp. 719–726, 1992, Accessed: Dec. 02, 2019. [Online]. Available: https://www.sciencedirect.com/science/article/pii/001793109290131B.

[156] J. A. Eastman, S. U. S. Choi, S. Li, W. Yu, and L. J. Thompson, “Anomalously increased effective thermal conductivities of ethylene glycol-based nanofluids containing copper nanoparticles,” *Appl. Phys. Lett.*, vol. 78, no. 6, pp. 718–720, Feb. 2001, doi: 10.1063/1.1341218.

[157] S. Alvarado, E. Marín, A. G. Juárez, A. Calderón, and R. Ivanov, “A hot-wire method based thermal conductivity measurement apparatus for teaching purposes,” *Eur. J. Phys.*, vol. 33, no. 4, pp. 897–906, 2012, doi: 10.1088/0143-0807/33/4/897.

[158] M. Abareshi, S. Sajjadi, and S. Zebarjad, “Fabrication, characterization, and measurement of viscosity of α-Fe2O3-glycerol nanofluids,” *J. Mol. Liq.*, vol. 163, no. 1, pp. 27–32, 2011, Accessed: Oct. 24, 2018. [Online]. Available: https://www.sciencedirect.com/science/article/pii/S0167732211002406.

[159] W. Roetzel and S. Prinzen, “Measurement of thermal diffusivity using temperature oscillations,” *Therm. Conduct.*, vol. 21, pp. 201–206, 1990, Accessed: Oct. 24, 2018. [Online]. Available: https://books.google.com/books?hl=en&lr=&id=ujRFHBWYmoUC&oi=fnd&pg=PA201&dq=Roetzel+W,+Prinzen+S,+Xuan+Y.+Measurement+of+thermal+diffusivity+usingtemperature+oscillations+thermal+conductivity.+In:+Cremers+CJ,+Fine+HA,+editors.Therm.+Conduct.+Int.+C.

[160] D. Zhu, X. Li, N. Wang, X. Wang, J. Gao, and H. Li, “Dispersion behavior and thermal conductivity characteristics of Al2O3-H2O nanofluids,” *Curr. Appl. Phys.*, vol. 9, no. 1, pp. 131–139, Jan. 2009, doi: 10.1016/j.cap.2007.12.008.

[161] J. Buongiorno *et al.*, “A benchmark study on the thermal conductivity of nanofluids,” *J. Appl. Phys.*, vol. 106, no. 9, p. 094312, Nov. 2009, doi: 10.1063/1.3245330.

[162] G. Paul, M. Chopkar, I. Manna, and P. K. Das, “Techniques for measuring the thermal conductivity of nanofluids: A review,” *Renew. Sustain. Energy Rev.*, vol. 14, no. 7, pp. 1913–1924, Sep. 2010, doi: 10.1016/J.RSER.2010.03.017.

[163] W. Jiang, G. Ding, and H. Peng, “Measurement and model on thermal conductivities of carbon nanotube nanorefrigerants,” *Int. J. Therm. Sci.*, vol. 48, no. 6, pp. 1108–1115, Jun. 2009, doi: 10.1016/j.ijthermalsci.2008.11.012.

[164] D. Zhu *et al.*, “Dispersion behavior and thermal conductivity characteristics of Al2O3–H2O nanofluids,” *Curr. Appl. Phys.*, vol. 9, no. 1, pp. 131–139, 2009, Accessed: Oct. 25, 2018. [Online]. Available: https://www.sciencedirect.com/science/article/pii/S1567173907002805.

[165] H. Wang and M. Sen, “Analysis of the 3-omega method for thermal conductivity measurement,” *Int. J. Heat Mass Transf.*, vol. 52, no. 7–8, pp. 2102–2109, 2009.

[166] D. Oh, A. Jain, J. Eaton, … K. G.-I. J. of, and U. 2008, “Thermal conductivity measurement and sedimentation detection of aluminum oxide nanofluids by using the 3ω method,” *Int. J. Heat Fluid Flow*, vol. 29, pp. 1456–1461, 2008, Accessed: Oct. 25, 2018. [Online]. Available: https://www.sciencedirect.com/science/article/pii/S0142727X08000738.

[167] H. Kurt, M. K.-A. Energy, and U. 2009, “Prediction of thermal conductivity of ethylene glycol–water solutions by using artificial neural networks,” *Appl. Energy*, vol. 86, pp. 2244–2248, 2009, Accessed: Oct. 25, 2018. [Online]. Available: https://www.sciencedirect.com/science/article/pii/S0306261908003334.

[168] B. Buonomo, O. Manca, L. Marinelli, and S. Nardini, “Effect of temperature and sonication time on nanofluid thermal conductivity measurements by nano-flash method,” *Appl. Therm. Eng.*, vol. 91, pp. 181–190, Dec. 2015, doi: 10.1016/J.APPLTHERMALENG.2015.07.077.

[169] N. Wu, L. Fu, M. Su, M. Aslam, K. C. Wong, and V. P. Dravid, “Interaction of Fatty Acid Monolayers with Cobalt Nanoparticles,” *Nano Lett.*, vol. 4, no. 2, pp. 383–386, 2004, doi: 10.1021/nl035139x.

[170] C. Pang, J. Y. Jung, J. W. Lee, and Y. T. Kang, “Thermal conductivity measurement of methanol-based nanofluids with Al 2O 3 and SiO 2 nanoparticles,” *Int. J. Heat Mass Transf.*, vol. 55, no. 21–22, pp. 5597–5602, Oct. 2012, doi: 10.1016/j.ijheatmasstransfer.2012.05.048.

[171] D. Zhu, X. Li, N. Wang, X. Wang, J. Gao, and H. Li, “Dispersion behavior and thermal conductivity characteristics of Al2O3-H2O nanofluids,” *Curr. Appl. Phys.*, vol. 9, no. 1, pp. 131–139, Jan. 2009, doi: 10.1016/j.cap.2007.12.008.

[172] K. Bootdee, M. Nithitanakul, and B. P. Grady, “Synthesis and encapsulation of magnetite nanoparticles in PLGA: effect of amount of PLGA on characteristics of encapsulated nanoparticles,” *Polym. Bull.*, vol. 69, no. 7, pp. 795–806, Oct. 2012, doi: 10.1007/s00289-012-0773-3.

[173] L. Zhang, R. He, and H.-C. Gu, “Oleic acid coating on the monodisperse magnetite nanoparticles,” *Appl. Surf. Sci.*, vol. 253, no. 5, pp. 2611–2617, Dec. 2006, doi: 10.1016/J.APSUSC.2006.05.023.

[174] J. Ibarra *et al.*, “Synthesis and characterization of magnetite/PLGA/chitosan nanoparticles,” *Mater. Res. Express*, vol. 2, no. 9, p. 095010, Sep. 2015, doi: 10.1088/2053-1591/2/9/095010.

[175] L. Zhang, R. He, and H. C. Gu, “Oleic acid coating on the monodisperse magnetite nanoparticles,” *Appl. Surf. Sci.*, vol. 253, no. 5, pp. 2611–2617, Dec. 2006, doi: 10.1016/j.apsusc.2006.05.023.

[176] Y. J. Hwang *et al.*, “Investigation on characteristics of thermal conductivity enhancement of nanofluids,” *Curr. Appl. Phys.*, vol. 6, no. 6 SPEC. ISS., pp. 1068–1071, Oct. 2006, doi: 10.1016/j.cap.2005.07.021.

[177] D. A. G. Bruggeman, “Dielectric constant and conductivity of mixtures of isotropic materials,” *Ann. Phys.(Leipzig)*, vol. 24, pp. 636–679, 1935.

[178] W. Yu and S. U. S. Choi, “The role of interfacial layers in the enhanced thermal conductivity of nanofluids: A renovated Maxwell model,” *J. Nanoparticle Res.*, vol. 5, pp. 167–171, 2003.

[179] D. H. Kumar, H. E. Patel, V. R. R. Kumar, T. Sundararajan, T. Pradeep, and S. K. Das, “Model for Heat Conduction in Nanofluids,” *Phys. Rev. Lett.*, vol. 93, no. 14, 2004, doi: 10.1103/PhysRevLett.93.144301.

[180] B. Wang, L. Zhou, X. P.-I. J. of H. and Mass, and U. 2003, “A fractal model for predicting the effective thermal conductivity of liquid with suspension of nanoparticles,” *Internatinal J. Heat Mass Transf.*, vol. 46, no. 14, pp. 2665–2672, 2003, Accessed: Feb. 01, 2020. [Online]. Available: https://www.sciencedirect.com/science/article/pii/S0017931003000164.

[181] B. X. Wang, H. Li, and X. F. Peng, “Research on the heat-conduction enhancement for liquid with nano-particle suspension,” *J. Therm. Sci.*, vol. 11, no. 3, pp. 214–219, 2002, doi: 10.1007/s11630-002-0057-6.

[182] M. N. Pantzali, A. G. Kanaris, K. D. Antoniadis, A. A. Mouza, and S. V. Paras, “Effect of nanofluids on the performance of a miniature plate heat exchanger with modulated surface,” *Int. J. Heat Fluid Flow*, vol. 30, no. 4, pp. 691–699, Aug. 2009, doi: 10.1016/j.ijheatfluidflow.2009.02.005.

[183] L. B. Mapa and S. Mazhar, “Heat transfer in mini heat exchanger using nanofluids,” in *American Society for Engineering Education*, 2005, pp. 1–2.

[184] B. Farajollahi, S. G. Etemad, and M. Hojjat, “Heat transfer of nanofluids in a shell and tube heat exchanger,” *Int. J. Heat Mass Transf.*, vol. 53, no. 1–3, pp. 12–17, Jan. 2010, doi: 10.1016/j.ijheatmasstransfer.2009.10.019.

[185] R. Chein and G. Huang, “Analysis of microchannel heat sink performance using nanofluids,” *Appl. Therm. Eng.*, vol. 25, no. 17–18, pp. 3104–3114, Dec. 2005, doi: 10.1016/j.applthermaleng.2005.03.008.

[186] S. P. Jang and S. U. S. Choi, “Cooling performance of a microchannel heat sink with nanofluids,” *Appl. Therm. Eng.*, vol. 26, no. 17–18, pp. 2457–2463, Dec. 2006, doi: 10.1016/j.applthermaleng.2006.02.036.

[187] H. A. Mohammed, G. Bhaskaran, N. H. Shuaib, and R. Saidur, “Heat transfer and fluid flow characteristics in microchannels heat exchanger using nanofluids: A review,” *Renewable and Sustainable Energy Reviews*, vol. 15, no. 3. Elsevier Ltd, pp. 1502–1512, Apr. 01, 2011, doi: 10.1016/j.rser.2010.11.031.

[188] A. Hosseinian, A. H. Meghdadi Isfahani, and E. Shirani, “Experimental investigation of surface vibration effects on increasing the stability and heat transfer coeffcient of MWCNTs-water nanofluid in a flexible double pipe heat exchanger,” *Exp. Therm. Fluid Sci.*, vol. 90, pp. 275–285, Jan. 2018, doi: 10.1016/j.expthermflusci.2017.09.018.

[189] M. Akhtari, M. Haghshenasfard, and M. R. Talaie, “Numerical and Experimental Investigation of Heat Transfer of[roman] alpha[/roman]-Al sub (2) O sub (3)/Water Nanofluid in Double Pipe and Shell and Tube Heat Exchangers,” *Numer. Heat Transf. Part A Appl.*, vol. 63, no. 12, pp. 941–958, 2013.

APPENDIX A

DEFORMATION MECHANISMS OF COBALT NANOWIRE: A MOLECULAR DYNAMICS MODELING ANALYSIS

Geometry of Cobalt nanowire for uniaxial tension test

Modeled nanowires have <100> axial direction with initial dimension of 210 x 52.5 x 52.5 (units in A^0) which corresponds to 84λ x 15 λ x 15 λ where λ is lattice constant of cobalt. Square cross section was selected to model integer number of unit cells and Shrink wrapped boundary conditions were employed in all direction. EAM potential was used for MD modeling analysis. Energy minimization was performed using conjugate gradient algorithm with fixed nanowire length followed by thermal equilibration via NVT (constant-temperature, constant-volume) at 298 K for 90 ps. Tensile loading (uniform strain rate of 4×10^7 s^{-1}) at the nanowire axis direction was emulated by assigning velocities for a group of atoms defined at both the ends of nanowires (0.5 A^0) called holding zone as shown in figure A-1.

Figure A-1. Initial Configuration of Cobalt Nanowire

Common neighbor analysis (CNA) was also Figure A-1. Initial nanowire configuration: cyan colored atoms show holding zone

performed to check the changes in crystal structure during deformation process.

Key Findings

After deformation of Co nanowire, we can see that the nanowires get elongated over time due to elastic deformation and are finally deformed primarily by twinning as shown in the circled region in figure A-2(c).

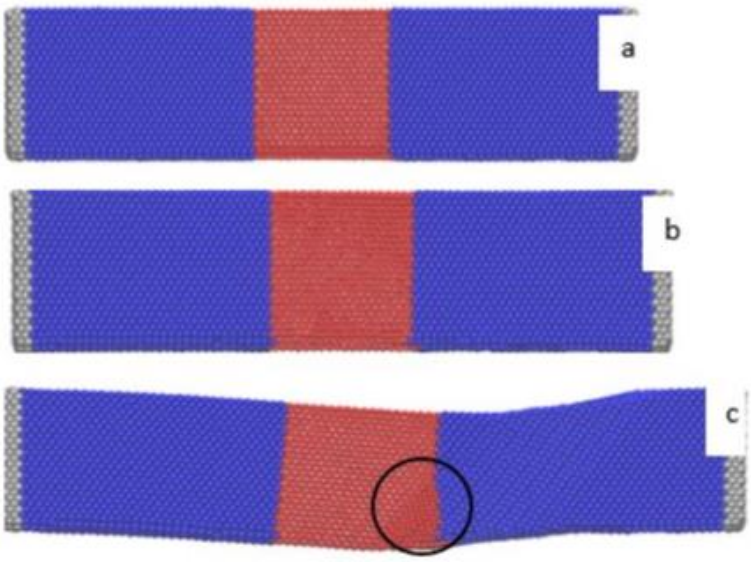

Figure A-2. Deformation Behavior of Co Nanowire; (a) Initial Configuration, (b) Configuration just before Yielding and (c) after Yielding

Stress-strain curve for cobalt nanowire is shown in figure A-3(a) where we can see linear stress strain behavior until the stress of 5.32 GPa with corresponding strain value of 5%. A stress relaxation behavior is noticed with initial stress drop after first

yield, which is followed by increase in stress with further increasing strain. The stress strain behavior can be divided into several stages. First stage, i→ii shows typical linear elastic deformation for metallic nanowires where (ii) is the yield point.

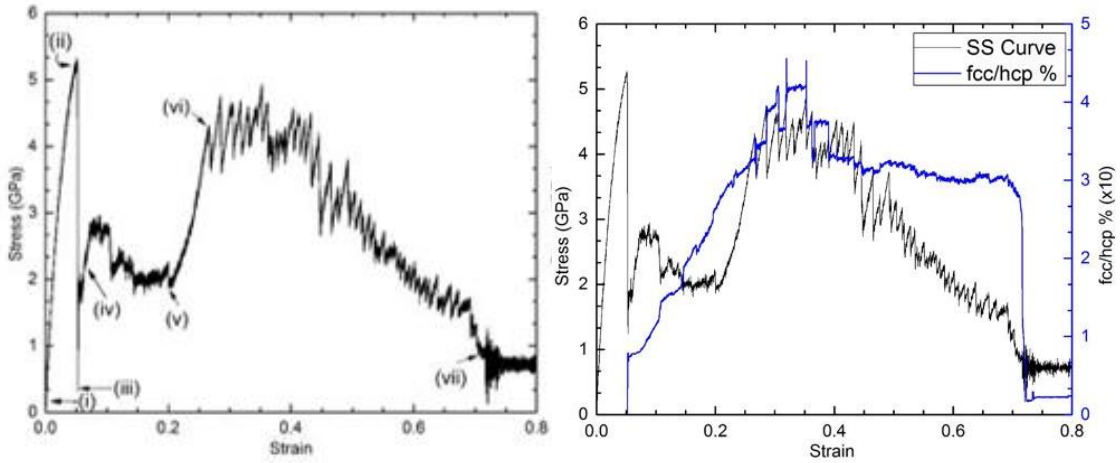

(a) (b)

Figure A-3. (a) Stress-strain curve of Co nanowire; (b) CNA analysis showing the fcc/hcp ratio during tensile deformation

Computed Young's modulus from the elastic region is 143 GPa. Stage ii →iii experiences sudden drop of stress from 5.32 GPa to about 0.25 GPa (very unstable and increases immediately) within an additional 0.28% strain. Further analysis of the results showed that during the increase in strain, *hcp* cobalt atoms show a transition to *fcc* structure (figure A-3 (b)). Stage iii→iv gives rise to the nucleation of *fcc* phase, thus increasing the stress value from 0.25 GPa to 2.8 GPa. With increase in strain, more and more atoms transform from *hcp* to *fcc* structure and continue to do so until about 20% strain. Another region v→vi can be identified where a second elastic like behavior is observed with stress increasing linearly to 4.24 GPa at 27% strain, and has been

mentioned as pseudo-elastic zone. Region vi→vii shows progressive failure with localized stress relaxation prior to final breaking at 72% strain.